# MICROMACHINED DIFFRACTION BASED OPTICAL MICROPHONES AND INTENSITY PROBES WITH ELECTROSTATIC FORCE FEEDBACK

A Dissertation
Presented to
The Academic Faculty

by

Baris Bicen

In Partial Fulfillment
of the Requirements for the Degree
Doctor of Philosophy in the
School of Mechanical Engineering

Georgia Institute of Technology
August 2010

# MICROMACHINED DIFFRACTION BASED OPTICAL MICROPHONES AND INTENSITY PROBES WITH ELECTROSTATIC FORCE FEEDBACK

Approved by:


Dr. F. Levent Degertekin, Advisor
School of Mechanical Engineering
*Georgia Institute of Technology*

Dr. Jerry H. Ginsberg
School of Mechanical Engineering
*Georgia Institute of Technology*

Dr. Kenneth Cunefare
School of Mechanical Engineering
*Georgia Institute of Technology*

Dr. Oliver Brand
School of Electrical and Computer Engineering
*Georgia Institute of Technology*

Dr. Ronald Miles
School of Mechanical Engineering
*Binghamton University*


Date Approved: 04/30/2010

Dedicated to my family…

# ACKNOWLEDGEMENTS

This thesis is made possible with contributions from many people. I would first like to thank to my thesis advisor, Professor F. Levent Degertekin, for giving me this opportunity and being a great mentor throughout the whole research experience. His knowledge, guidance and motivation helped me to contribute my knowledge and keep me on the right track to finish this thesis work. I would also like to thank Professors Jerry H. Ginsberg, Kenneth Cunefare, Oliver Brand and Ronald Miles for serving on my thesis committee and for their constructive feedback.

I am thankful for the help and support of all members of Micromachined Sensors and Transducers (MiST) Laboratory. Special thanks go to Dr. Neal Hall being a second mentor in my thesis and teaching me all the technical background of this thesis work and also being a great friend. I also owe many thanks to Caesar Garcia, Dr. Wook Lee, Dr. M. Shakeel Qureshi and Sunny Jolly who are previous members of MiST group. I have equally enjoyed working with all. I also would like to thank Guclu Onaran and Utku B. Pazar for helping out with theoretical issues and being helpful friends all the time. In addition to all, I enjoyed sharing lots of valuable thoughts and also sharing the office and friendship with Hamdi Torun, Zehra Parlak and Ofer Finkler.

I also owe special thanks to the National Institute of Health and Catalyst Foundation for their support to this research, and the Vibrations Research Laboratory at Binghamton University, New York. Specifically, many thanks are owed to Professor Ron Miles, Dr. Quang Su, and Dr. Weili Cui for supplying the biomimetic directional microphone devices and sharing their valuable ideas. I would also like to thank Professor Cunefare's Integrated Acoustics Laboratory for generously letting me use the equipment and acoustic testing facilities at Georgia Tech.

# TABLE OF CONTENTS

# LIST OF TABLES

# LIST OF FIGURES

# SUMMARY

Measuring acoustic pressure gradients is critical in many applications such as directional microphones for hearing aids and sound intensity probes. This measurement is especially challenging with decreasing microphone size, which reduces the sensitivity due to small spacing between the pressure ports. Novel, micromachined biomimetic microphone diaphragms are shown to provide high sensitivity to pressure gradients on one side of the diaphragm with low thermal mechanical noise. These structures have a dominant mode shape with see-saw like motion in the audio band, responding to pressure gradients as well as spurious higher order modes sensitive to pressure. In this dissertation, integration of a diffraction based optical detection method with these novel diaphragm structures to implement a low noise optical pressure gradient microphone is described and experimental characterization results are presented, showing 36 dBA noise level with 1mm port spacing, nearly an order of magnitude better than the current gradient microphones. The optical detection scheme also provides electrostatic actuation capability from both sides of the diaphragm separately which can be used for active force feedback. A 4-port electromechanical equivalent circuit model of this microphone with optical readout is developed to predict the overall response of the device to different acoustic and electrostatic excitations. The model includes the damping due to complex motion of air around the microphone diaphragm, and it calculates the detected optical signal on each side of the diaphragm as a combination of two separate dominant vibration modes. This equivalent circuit model is verified by experiments and used to predict the microphone response with different force feedback schemes. Single sided force feedback is used for active damping to improve the linearity and the frequency response of the microphone. Furthermore, it is shown that using two sided force feedback one can significantly suppress or enhance the desired

vibration modes of the diaphragm. This approach provides an electronic means to tailor the directional response of the microphones, with significant implications in device performance for various applications. As an example, the use of this device as a particle velocity sensor for sound intensity and sound power measurements is investigated. Without force feedback, the gradient microphone provides accurate particle velocity measurement for frequencies below 2 kHz, after which the pressure response of the second order mode becomes significant. With two-sided force feedback, the calculations show that this upper frequency limit may be increased to 10 kHz. This improves the pressure residual intensity index by more than 15 dB in the 50 Hz-10 kHz range, matching the Class I requirements of IEC 1043 standards for intensity probes without any need for multiple spacers.

# CHAPTER 1

# INTRODUCTION

This chapter gives a brief introduction to properties of acoustic signals in the audio frequency range and their measurements. Conventional capacitive microphones and sound intensity probes are summarized, indicating a need for new technologies in this field. One of the alternatives to capacitive sensing is optical sensing. A short background of a particular optical detection method is given and the motivation behind this dissertation is described.

## Sound Measurements

Sound is a form of energy produced by the movement and vibration of molecules in a medium. Different properties of sound are measured in order to understand its characteristics. Sound pressure is the most common measured quantity, and it gives information on the amount of sound that is heard when measured in the audio band. Sound pressure can easily be measured using acoustic transducers like microphones. However since pressure is a scalar quantity, it does not give any information about the direction of the sound. If the sound power emitted by a directional sound source or the location of sound sources is to be found, then the direction of the sound radiated also needs to be measured. This information usually comes from particle velocity measurement. Combining the particle velocity and pressure information, the intensity of the sound can be determined. In the following sections of this chapter, conventional

microphone technology for measuring the sound pressure field and conventional sound intensity probe technology used for determining the sound intensity or sound power are described.

**Capacitive Microphone Technology**

Microphones, devices that convert sound signals into electrical signals, are widely used in many different applications like cellular phones, electronic devices, hearing aids and acoustic measurement devices. The performance needs for these applications are also different. For example, the most important factor for microphones used in cellular phones is total system and integration cost; whereas for high performance scientific measurement microphones, sensitivity and bandwidth are the most important criteria. The common microphone design uses a thin membrane that vibrates with the incoming sound pressure wave. The vibration of the membrane can be translated into electrical signal by different methods.

In capacitive microphones, a pair of electrically conductive electrodes forms a capacitor as seen in Figure 1. The top electrode, which is the membrane in this case, and rigid back electrode (back plate) are separated by a gap. The top electrode vibrates by the incoming sound wave. This vibration causes a change in the capacitance and this change is detected either as a voltage change under constant charge or charge variation at constant voltage conditions. Despite its popularity and simplicity, capacitive detection has fundamental problems that limit its performance.

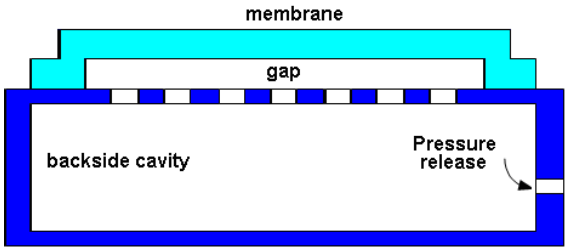


Figure 1: Conventional capacitive microphone

When the microphone is operated under constant charge the conversion factor between the membrane displacement and the output voltage can be called the electrical sensitivity, $S_e$, and is measured in Volts/meter. Similarly, the mechanical sensitivity, $S_m$, is the ability to convert the applied pressure into membrane displacement. Mechanical sensitivity is measured in meter/Pascal. The total sensitivity of the device to sound pressure can then be expressed as $S_e$ x $S_m$, with units of Volts/Pascal. To obtain higher electrical sensitivity in a capacitive microphone, the gap distance between two electrodes should be small, and high DC bias voltages should be applied to electrodes. However, the DC bias voltage is directly related with the gap height because of the electrostatic collapse phenomena. As the gap height gets smaller, the maximum DC voltage that can be applied to the device before collapse also decreases [1]. This condition causes a design conflict. The other important limitation is that the detection scheme becomes nonlinear near the collapse voltage where the maximum electrical sensitivity can be achieved [1, 2].

In order to relax some of the tradeoffs that are caused by the electrical sensitivity, the membrane of the microphone should be compliant and large. This will generate a larger displacement for a given pressure, increasing the mechanical sensitivity of the microphone. Making a compliant and large membrane is not trivial, especially using microfabrication processes because of the membrane stress which may not be controlled

easily [3]. Special fabrication processes are used to overcome this stress issue [4-6]. Furthermore, the back plate of the microphone should be perforated to prevent the stiffening effect of the squeezed air between two electrodes [7]. Since the total effective area directly affects the capacitance and hence the electrical signal output, perforating the back plate reduces the electrical sensitivity [1]. With these design limitations, measurement quality capacitive microphones achieve noise levels of 15-20 dBA with 12.7 mm diameter membranes and DC bias of about $200V_{DC}$ [8]. Although these are impressive figures, they are still prohibitive for many applications where small size and high performance are required.

Advances in microelectromechanical systems (MEMS) technology has made it possible to fabricate small-sized capacitive micromachined microphones which are commercially viable for applications like cell phones [1, 9, 10]. However, achieving noise levels acceptable for measurement instruments and hearing aids has not been possible due to the factors described above, in addition to detrimental effects of parasitic capacitance at that small scale.

**Directional Microphones**

Directional microphones have sensitivity that depends on the direction of the incident sound wave. They are typically used to suppress unwanted sounds from directions other than that of the sound source of interest. Miniature directional microphone systems are often used in hearing aids to improve speech intelligibility in noisy environments [11-14]. In addition, during outdoor recordings and in environments

when there is excessive background noise, directional microphones are preferred over conventional pressure microphones.

For a microphone's response to depend on the direction of an incoming acoustic sound wave, the difference in acoustic pressure at minimum of two different points must be measured. The common method used in directional microphones is to measure the sound pressure with the help of two sound ports across a single diaphragm as seen in Figure 2 [15]. When the sound comes in 90° angle, the acoustic pressure on each side of the diaphragm is the same, resulting in zero pressure difference and zero output. However, when the sound comes from the sides (0° or 180° angles shown in Figure 2), it arrives at one port little sooner than it arrives at the other port, causing a pressure difference on the diaphragm.

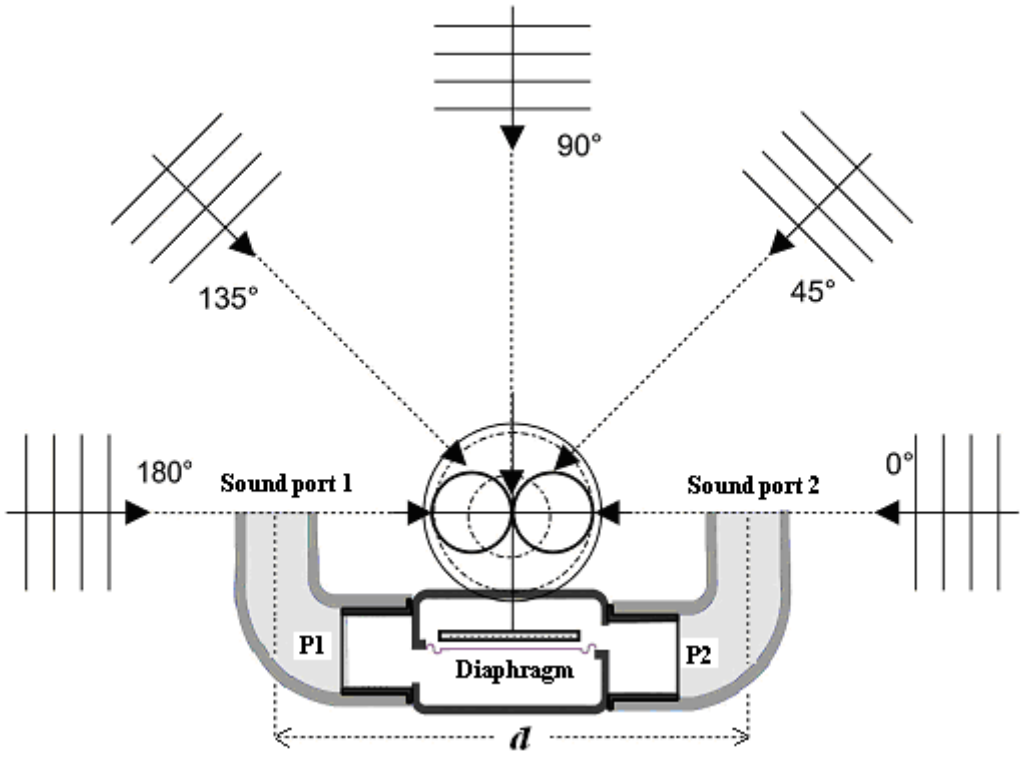


Figure 2: Conventional directional mic. with two ports separated by a distance, *d* [15]

Since the directional microphone subtracts the pressure on each side of the diaphragm, the sensitivity of these microphones is highly dependent on the separation distance, d, between the sound ports. This separation distance needs to be significant as compared to the wavelength of the sound to get accurate results. When the distance between ports gets smaller in order to decrease the size of the microphone, the pressure difference, $P_2$-$P_1$, between these two ports becomes too small to be detected accurately. Figure 3 shows the degradation in the sensitivity of the directional microphones with changing port distance. This figure shows the reduction in sensitivity of a directional microphone especially at low frequencies. The reduction is greater when the separation distance between two ports gets smaller. As a result of this, it is challenging to have a directional microphone with small size and high sensitivity.

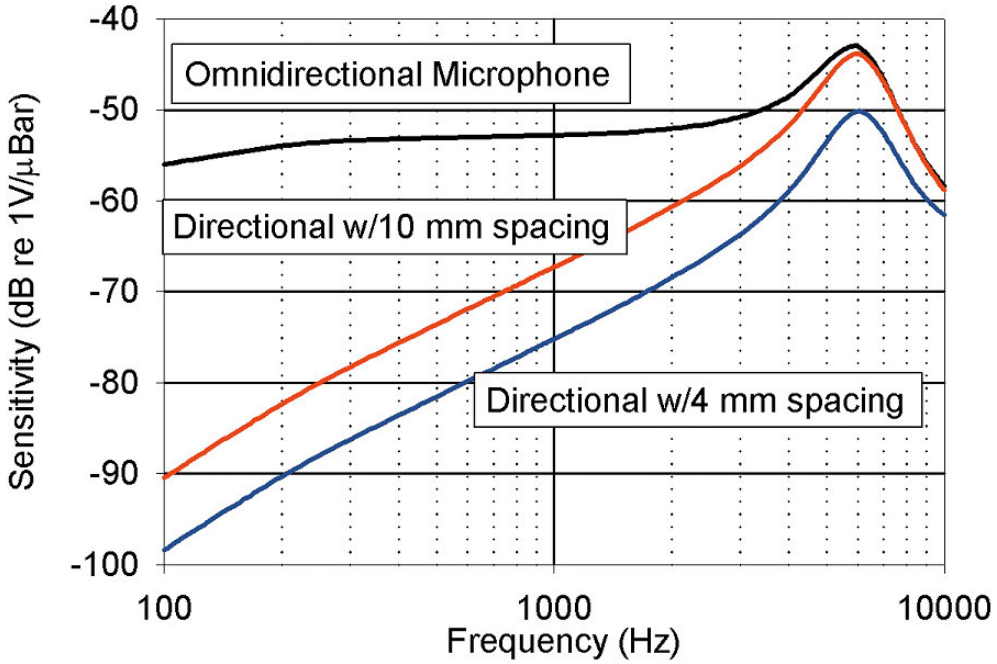


Figure 3: Sensitivity of directional microphones with different port spacing compared with the omnidirectional microphone [15]

Recently, a biomimetic differential microphone structure that is sensitive to the pressure difference on one side of a single diaphragm has been developed as an alternative method of constructing a directional microphone [16-18]. In this thesis, this structure is used in conjunction with a highly sensitive optical detection method to implement low noise, miniature pressure gradient microphones. This structure and the integrated optical detection method are described in detail in Chapters 2.

**Optical Microphones**

The limitations of capacitive detection especially in micromachined microphones indicate a need for alternative sensing techniques. Optical detection, which sets the standard for displacement measurement through interferometry, has been an alternative detection method with similar or improved microphone performance for several applications [19-22]. Although a variety of optical techniques have been investigated, most of them have not been successful in microscale implementations, due to integration difficulties [22, 23]. With the advancing communications industry, integrated optical components which offer the possibility of constructing inexpensive small scale optical measuring systems became more available [24]. The optical detection scheme that is more feasible to integrate is the interferometric detection method shown in Figure 4. In this method, the incoming beam of light is split into two beams which are then passed along different paths. When these two beams are combined, the interference takes place because of the path length difference. This interference can be any combination of the constructive and destructive interferences depending on the displacement of the moving

object. The detection of this interference with a light intensity sensor makes it possible to obtain highly sensitive displacement measurements.

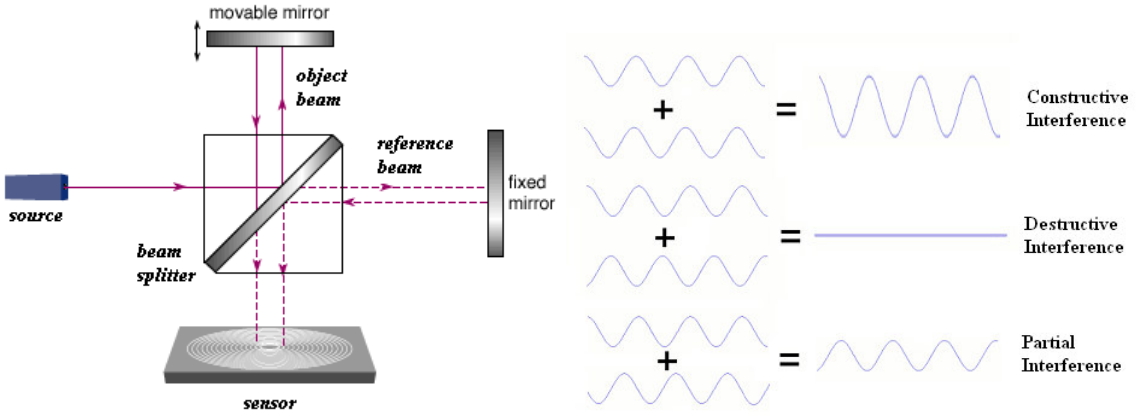


Figure 4: Basic working principle of Michelson Interferometer (left) and different types of interference curves (right)

By using inter-digital diffraction gratings, the optical detection can be designed to be highly sensitive. This method has been used in displacement detection of atomic force microscopy and in accelerometers [25-27]. Initial work with diffraction based optical displacement detection shows 20 fm/rt(Hz) displacement detection resolution with 61 μW laser power detected on the photodiodes. Combining this method with micromachined diaphragms enables microphones to reach a 24 dBA A-weighted sound pressure level detection limit [28, 29]. The details of the diffraction based optical detection method will be described in Chapter 2.

## Sound Intensity Measurements

Sound intensity in a specified direction is the rate at which sound energy is transmitted through a unit area perpendicular to that direction. From basic acoustics, the sound intensity at any point in the sound field can found from the pressure and the particle velocity vector. The instantaneous sound intensity at any point is determined by;

$$I(t) = p(t)u(t) \tag{1}$$

where $p(t)$ is the instantaneous pressure and $u(t)$ is the instantaneous particle velocity. The average sound intensity is obtained by averaging the above equation over time $T$ .

$$I = \frac{1}{T}\int_{-T/2}^{T/2} p(t)u(t)dt \tag{2}$$

The relationship between the instantaneous intensity *I(x, t)* and the time plots of pressure and particle velocity can be seen from Figure 5. The top plot in Figure 5 describes the case when the phase difference between the pressure and the particle velocity is zero. In this case the reactive intensity which is the imaginary part of the complex intensity is zero. If the phase difference between the pressure and the particle velocity is $\pi/2$, which is the case shown in the bottom plot of Figure 5, then the sound field is known as reactive where the real part (active part) of the complex intensity is zero [30].

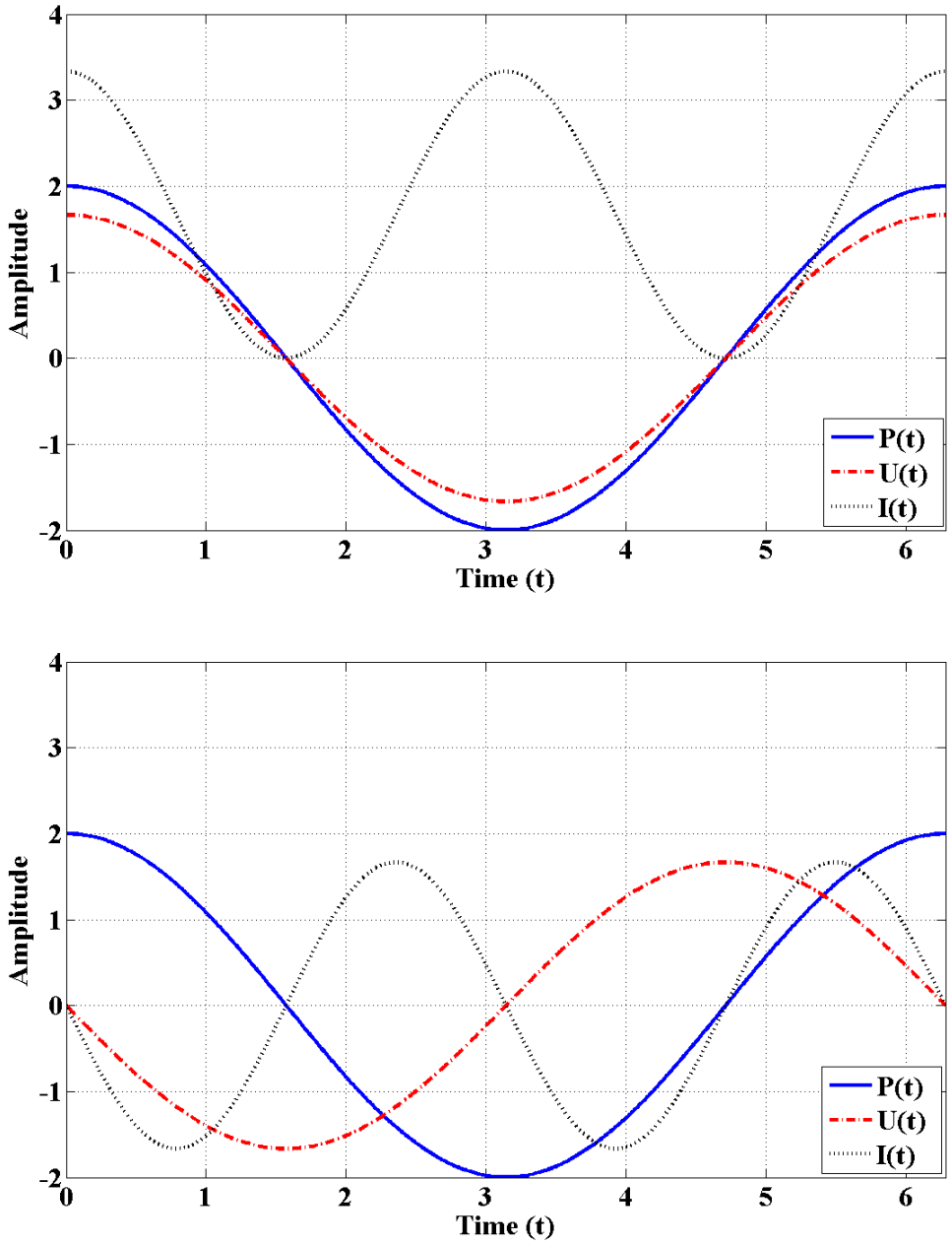


Figure 5: Time plots of pressure, *P(t)*, (solid line), particle velocity, *U(t)*, (dotted-dashed line) and the instantaneous intensity, *I (t),* (dotted line), when the phase difference between the pressure and the particle velocity is zero (top) or $\pi/2$ (bottom)

**Conventional Sound Intensity Probe Technology**

Sound intensity is useful in sound power measurements, transmission loss and transmission path measurements, identification of different sources and sound fields. In order to measure the sound intensity, sound pressure and the particle velocity at that point need to be known. Sound pressure is relatively easy to measure by using a simple sound pressure microphone. The challenge in measuring the sound intensity comes from the accurate derivation or measurement of the particle velocity. Starting from the 1930s, measuring sound intensity has been a research topic. The history of sound intensity measurements started with the patent by Harry Olson in 1932 [31]. In the 1940s, the combination of ribbon velocity microphones and crystal pressure microphones was first used in order to measure sound intensity fields [32]. In 1943, the two pressure microphone method was used to measure acoustic impedances of materials, which lead to the two microphone intensity measurements [33]. In 1956, Schultz found the principle of using two pressure microphones to obtain particle velocity by integrating the difference of microphone outputs [34]. After advances in the digital signal processing technology in 1970s, commercial sound intensity probes became available in the market.

Two different methods, namely the PP-method and the PU-method, are used to measure the sound intensity. The PP-method, which stands for Pressure-Pressure, is the most common. This method uses a PP-probe that is composed of two pressure microphones separated from each other by a distance $\Delta r$. In these probes, particle velocity in the direction of the axis of the probe can be calculated using the Euler's equation of motion which is given as;

$$u = -\frac{1}{\rho}\int \frac{\partial p}{\partial r} dt \qquad \textbf{(3)}$$

By using the finite difference approximation, this particle velocity equation can be approximated as;

$$u = -\frac{1}{\rho}\int \frac{p_1 - p_2}{\Delta r} dt \tag{4}$$

In the PP-method, the pressure is calculated from the average of two pressure values measured with two microphones. With pressure and particle velocity at hand, the sound intensity can be calculated as;

$$I = -\frac{p_1 + p_2}{2\rho}\int \frac{p_1 - p_2}{\Delta r} dt \tag{5}$$

where $p_1$ and $p_2$ are the pressure output of two microphones, ρ is the density of air and Δr is the separation distance between two microphones.

The most important challenge in the PP-method comes from the finite difference approximation and the phase mismatch between two pressure microphones. The smaller the distance between the two pressure microphones, the better the finite difference approximation. However, with reduced distance the pressure difference – mostly due to phase- that needs to be measured gets smaller, which is more challenging at low frequencies due to large wavelengths. Therefore the distance between microphones sets the useful frequency range in which intensity measurements can be done accurately. In order to get accurate results in different frequency ranges, different separation distances should be used, which may be impractical. Typical spacer dimensions that are used in commercial sound intensity probes and the useful frequency range of these spacers are shown in Figure 6. The lower frequency limit of the PP-probes with specified spacer dimension in this figure is related to the total phase mismatch of the microphone pair and the processing unit. Microphones that are used with the PP-method should be perfectly

phase matched, especially in the low frequency range. Phase mismatch is important because the phase difference between two microphones is interpreted as particle velocity causing errors in the velocity measurement. It can be seen from the figure that when the total phase mismatch increases, the lower frequency limit of the sound intensity probe also increases.

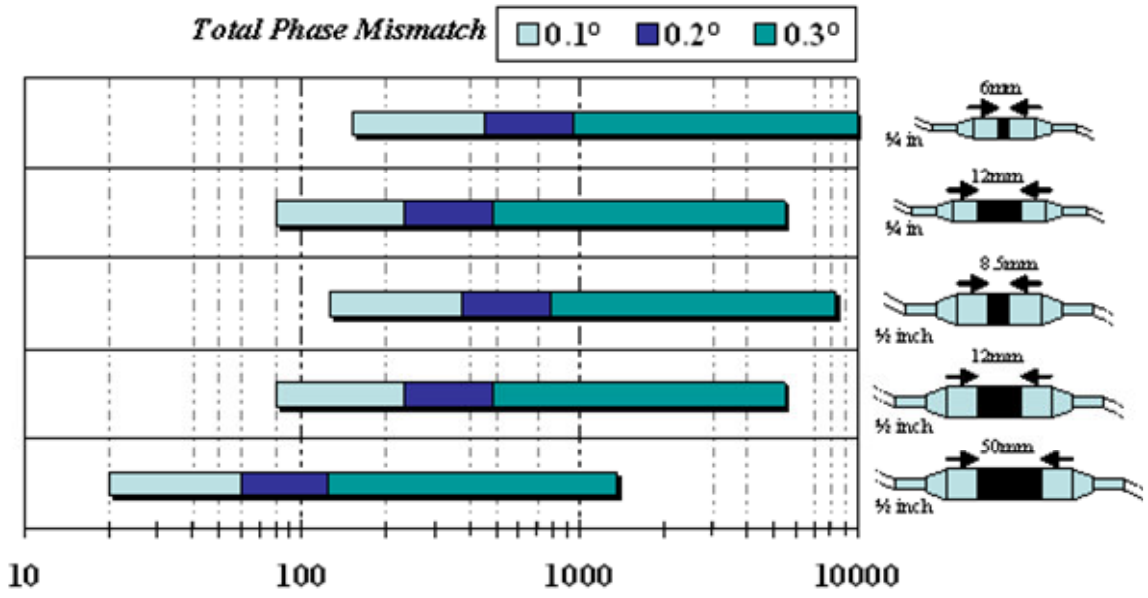


Figure 6: Measurement frequency ranges of a commercial PP-sound intensity probe with changing spacer and microphone dimensions [35]

The other important challenge with the PP-method is the size. Because of the required spacer dimension, the size of PP-intensity probes is large. This makes sound intensity measurements of small objects in limited spaces difficult. In addition, 3D sound intensity probes consist of 6 microphones, which make the size of 3D-probes impractical. A commercially available Larson Davis PP-probe and GRAS 3D PP-probe are shown in Figure 7 to show dimensions of the current technology. In addition to these problems,

the sound field in which the measurement is done is also important when a PP-probe is used. One of the most important indicators for the sound field is the pressure-intensity index which is the difference between pressure and the intensity level. Reflections, diffuse sound fields or additional noise sources in a sound field make the pressure level to be high while the intensity is low, resulting in high pressure-intensity index. PP-probes face difficulties in these sound fields that have a high pressure-intensity index [36].

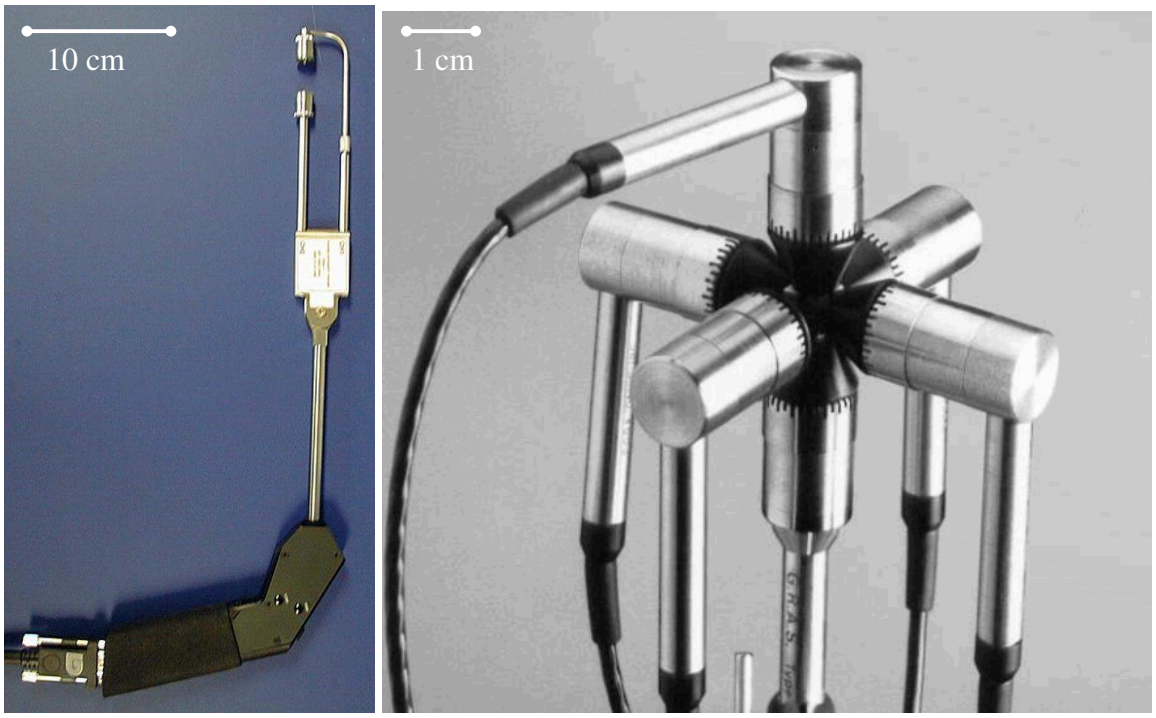


a) b)

Figure 7: a) Larson Davis PP-sound intensity probe with two ½ inch microphone, b) GRAS 3-dimensional PP-sound intensity probe with six ½ inch microphones [37, 38]

The second method in measuring the sound intensity is the PU-method which stands for Pressure-Velocity method. A PU-probe uses a pressure microphone to measure the pressure at the point of interest and a sensor that measures the corresponding particle

velocity at the same point. Some of the challenges with the PP-probes are solved using PU-probes [36, 39]. Since there is no spacer, the size of the PU-probe can be small depending on the size of the velocity sensor. As expected, the limitations of the PU-probe come from the particle velocity sensor. Figure 8 shows the picture of a commercial particle velocity sensor (known as Microflown), and a PU-intensity probe consists of this velocity sensor and a pressure sensor [40]. A Microflown particle velocity sensor consists of two wires which are made of temperature dependent material. When a voltage is applied across these wires, they heat up. Depending on the flow direction and amplitude which determines the particle velocity, the temperature difference between these two wires changes. This temperature difference causes a change in the resistance of the wires, which is measured and converted to particle velocity. Since the temperature change of the wires depends on the direction of the particle velocity, this particle velocity sensor is sensitive only in one direction perpendicular to the wires [41]. This velocity sensor has a frequency response with a roll off at 1 kHz. The 6dB per octave decrease in the sensitivity between 1 and 10 kHz comes from the diffusion effect related with the distance between the two wires (about 40μm). Above 10 kHz, the sensitivity experiences an additional 6dB per octave decrease because of the thermal heat capacity of the wires [42].

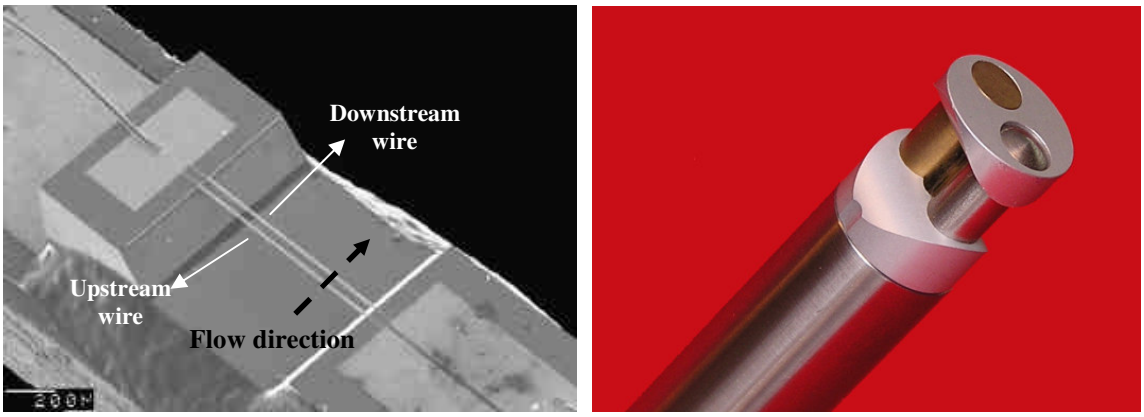


a) b)

Figure 8: a) Microflown particle velocity sensor, b) Microflown ½ inch PU-sound intensity probe [42]

In addition to size advantages, directly measuring the particle velocity instead of using finite difference approximation avoids errors that come from the approximation of the velocity. The phase difference between the pressure and velocity transducer is not as critical as the phase mismatch of the two pressure microphones. Although it solves some problems of the PP-probe, the PU-probes usually suffer from low bandwidth because of the flow based velocity sensing [42]. Velocity transducers have problems caused by environmental effects like wind and temperature [43]. Since both PP and PU-probes have advantages and disadvantages, neither of these methods is totally effective across the whole frequency range from 50Hz to 10000Hz.

## Motivation

As described earlier in this chapter, the current technology with traditional microphones and intensity probes has problems in terms of sensitivity, noise, bandwidth

and size. The limitations of the capacitive detection in current microphones are the main motivation to use the optical displacement detection method with different microphone structures. One of those microphone structures is the biomimetic differential microphone. In these microphones the advantage of highly sensitive optical displacement detection method has already been shown [18].

The main goal of this thesis is to show that it is feasible to fill some of the gaps in current technology using optical microphones and intensity probes based on these microphones. For this purpose, the force feedback ability of the optical detection method is combined with the novel design of differential microphone structures. In terms of microphones, the target is to get optical microphones with small size, low noise, high bandwidth and high dynamic range. Force feedback method allows altering the microphone dynamics in a desirable manner to make the optical microphones more favorable than traditional microphones, which have challenges and tradeoffs described earlier. In terms of intensity probes, the target is to get probes with small size and high bandwidth, overcoming the limitations of current sound intensity probes. Force feedback with different schemes can also be used to make these gradient microphones to respond only to pressure gradients by drastically reducing the effect of unwanted modes of the diaphragm.

In the next section of this dissertation, the optical interferometric displacement detection method is summarized [44, 45]. It is shown that the optical detection method can be integrated with the biomimetic directional microphone diaphragms in a small scale package. Because of the problems with the small scale integration of the optical displacement detection method, an optical model is developed and details of this optical

model are explained. Chapter 3 describes the feasibility of these microphones in measuring particle velocity measurement. Comparisons with a commercial particle velocity sensor and a sound intensity probe are presented. Chapter 4 gives a detailed description of an equivalent circuit model of these directional microphones which provides insight into the effect of individual modes on the overall microphone response, the asymmetric characteristics of the optical detection scheme and the use of electrostatic actuation for force feedback implementation. Chapter 5 describes the force feedback method and its capabilities based on the equivalent circuit model. It is shown that optimization of these optical gradient microphones in order to get better sound intensity probes with high bandwidth, and small size is possible using the force feedback method. The last chapter summarizes the importance of this research work and gives some recommendations as future guidelines.

# CHAPTER 2

# MICROPHONES WITH DIFFRACTION BASED OPTICAL DETECTION METHOD

As described in the previous chapter, there are some disadvantages of capacitive sensing in micromachined microphones. One of the alternative methods for capacitive sensing is a diffraction-based optical displacement detection method to implement low noise micromachined microphones [46, 47]. In this study, an optical detection method is used as a sensing mechanism that converts the diaphragm motion into an electrical signal without suffering from the adverse effects of viscous damping between the capacitive electrodes and parasitic capacitance. This chapter first summarizes the working principle of this diffraction based optical displacement detection method. The novel biomimetic diaphragm structure, its vibration modes and a simple mechanical model describing the dynamics of its first two dominant modes are discussed. The integration of optical detection with the biomimetic diaphragms and packaging issues are described next. Finally, characterization results of these microphones are summarized and a detailed optical model, developed to enhance the performance of the optical detection method, is described.

## Diffraction Based Optical Displacement Detection Method

The basic schematic that shows the operating principle of the diffraction based optical displacement detection scheme is shown in Figure 9. In this method, there is a

diffraction grating and sensor membrane (backplate) pair forming bottom and top electrodes. In Figure 9, the diffraction gratings are shown as fixed and the sensor membrane is moving with external excitations. However for different implementations, moving diffraction gratings with a fixed backplate can also be used. This grating-backplate structure is illuminated with a light source such as a laser. The grating structure reflects some of the incident light. The other portion of the light directly reflects from the backplate and interferes with the light reflected from the grating. The diffracted orders formed with this interference are captured by using separate photodiodes placed next to the laser so that the intensity change in diffracted orders can be monitored. The intensities of the resulting diffracted orders are modulated by the change in the gap thickness between the grating and the backplate. This method, which was analyzed in detail previously [46], works as a Michelson interferometer.

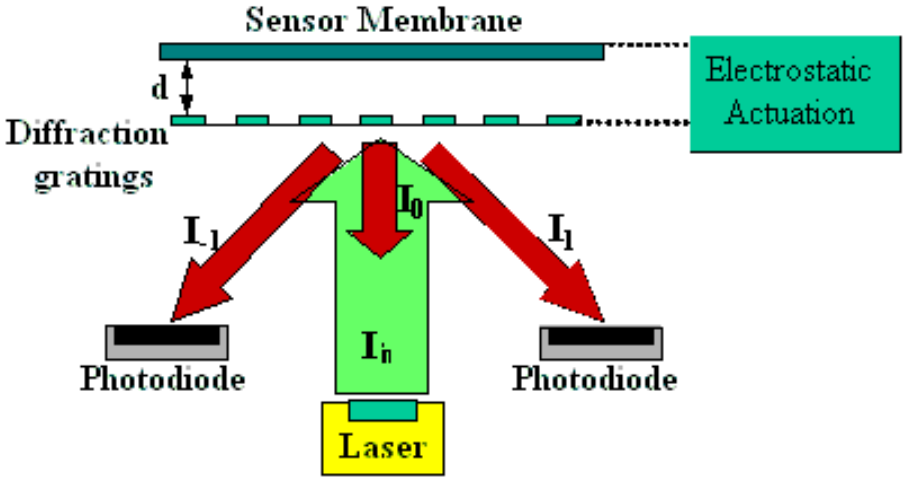


Figure 9: Basic schematic of the diffraction based optical displacement detection method.

Using scalar diffraction theory, the beam intensity of the zero and first diffraction orders can be calculated. The analysis gives intensities as;

$$I_0 = I_{in} \cos^2\left(\frac{2\pi d}{\lambda_0}\right) \quad (6)$$

$$I_1 = \frac{4I_{in}}{\pi^2} \sin^2\left(\frac{2\pi d}{\lambda_0}\right) \quad (7)$$

where $I_{in}$ is the incident laser intensity, $d$ is the gap thickness between electrodes and $\lambda_0$ is the optical wavelength. These 1st and 0th order intensities vs. the gap thickness are plotted in Figure 10 for 650nm optical wavelength.

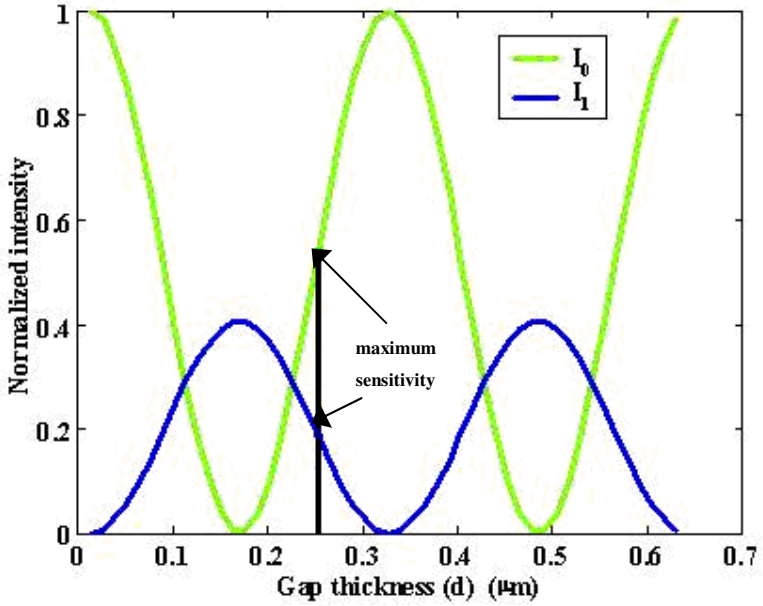


Figure 10: First and zero order normalized light intensities as a function of gap thickness for light source with optical wavelength of 650nm.

It is clear from Figure 10 that when the gap thickness is a multiple of $\lambda_0/2$, the zero order intensity is a maximum and the diffraction grating acts as a perfect mirror. When the gap thickness is an odd multiple of $\lambda_0/4$, the first order intensity becomes a maximum. To get the highest sensitivity from these diffracted orders, $d$ should be an odd

multiple of $\lambda_0/8$ where the slope of the intensity curve is a maximum. At this maximum sensitivity point, which is the inflection point, this curve is linear. Any factor that causes a shift of the operating point from the maximum sensitivity point results in nonlinearity.

The optical detection scheme provides a highly sensitive method of obtaining an electronic output from microphone diaphragms without adding too much electronic noise. For example, with 20μW laser power on a photodetector having 0.5 A/W responsivity and using 200 Kohm feedback resistance for transimpedance amplifier, the displacement sensitivity of the optical detection is 15mV/nm. With this configuration, the shot noise voltage limit can be found as -129dBV/rt(Hz), which sets the displacement resolution as 24fm/rt(Hz). In this optical detection method, sensitivity does not depend on device capacitance or device size. Because the same sensitivity can be achieved with large grating-reflector distances, the noise due to the squeeze film viscous damping of the air in the gap has minimal influence on the response. Also, different and novel backplate designs can be implemented, since the capacitance of the device is not critical [48]. Usually the dominant noise source in the optical detection is the laser intensity noise, which can be reduced by using the differential detection (first and zero order). With the differential detection, ideally shot noise limits can be achieved [49, 50]. Optoelectronics integration can be made easier by fabricating photodetectors with the integrated amplifiers on the same wafer with the microphone structure [51].

## Biomimetic Directional Microphone Structures

The biomimetic directional microphones used in this research are inspired by the ears of the fly *Ormia ochracea* which has a remarkable ability for directional hearing and

locating sound sources [16, 18, 52, 53]. As shown in Figure 11, the microphone diaphragm is essentially a rigid, but light-weight teeter-totter structure that rotates around a central pivot. Figure 11a shows the top view of the diaphragm, which is fabricated out of polycrystalline silicon and has lateral dimensions of 1mm by 2mm and thickness of about 1.3µm. This structure is placed over a backside cavity with narrow openings around its periphery, and the diaphragm has slits in the middle close to the pivot to allow air flow in and out of the backside cavity. The backside cavity and the stiffeners on the diaphragm can be seen from the picture in Figure 11b. The diaphragm is connected to a rigid substrate with pivots on each side of the diaphragm's center points. The diaphragm rotates when there is a pressure gradient over its front surface along its long axis leading to a directional response.

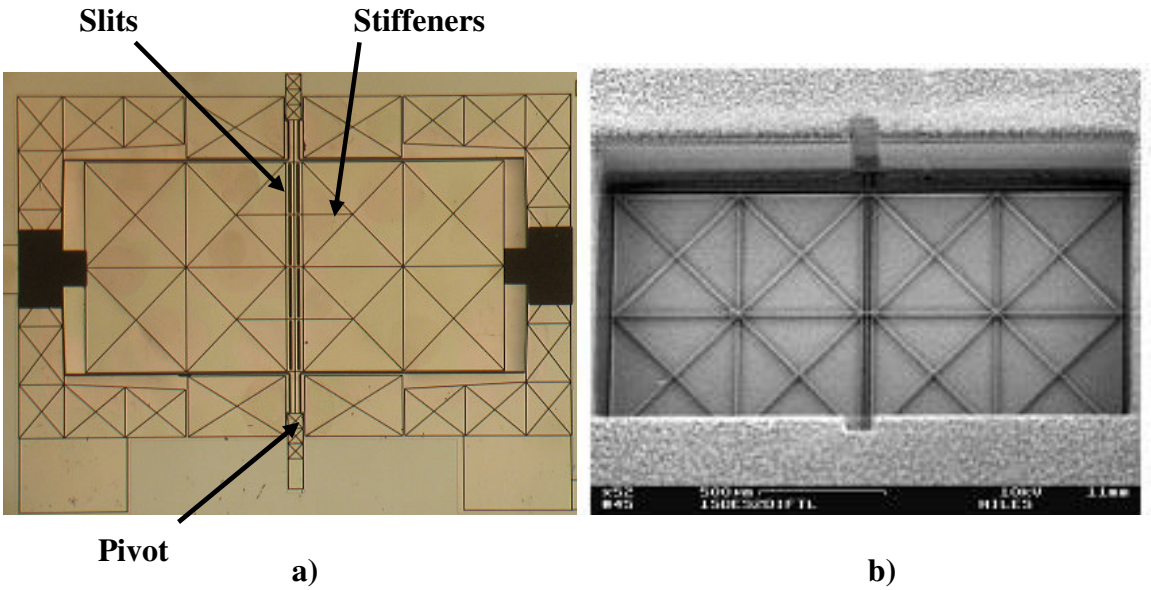


Figure 11: a) Top view of the directional diaphragm b) scanning electron microscope (SEM) picture taken from the backside to show the backside cavity and diaphragm stiffeners

As expected, this structure has several vibration modes in the frequency range of interest, between 20Hz to 20 kHz, as well as higher order modes at higher frequencies. These vibration modes are predicted by using a finite element modal analysis. In this analysis, ANSYS software with a Block Lanczos routine is used to extract the first 7 mode shapes and corresponding mode frequencies as illustrated in Figure 12.

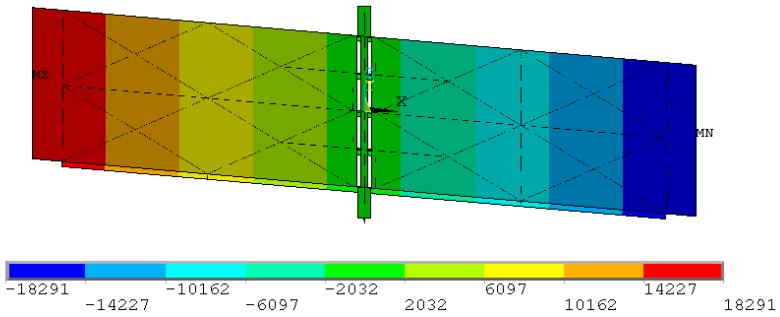


a) $f_1$= 800 Hz

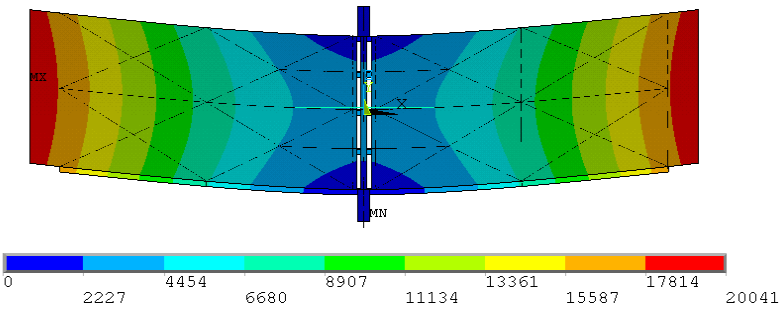


b) $f_2$ =14 kHz

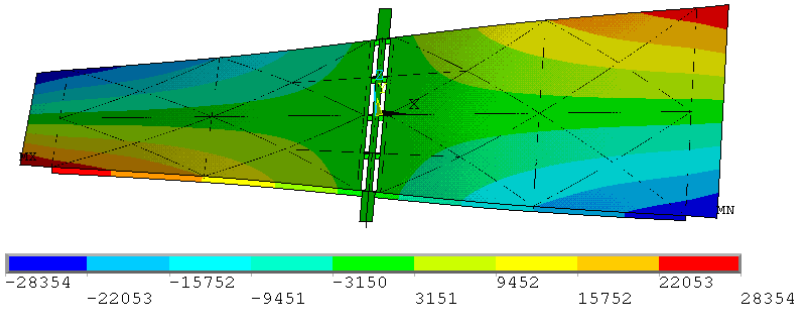


c) $f_3$ = 28 kHz

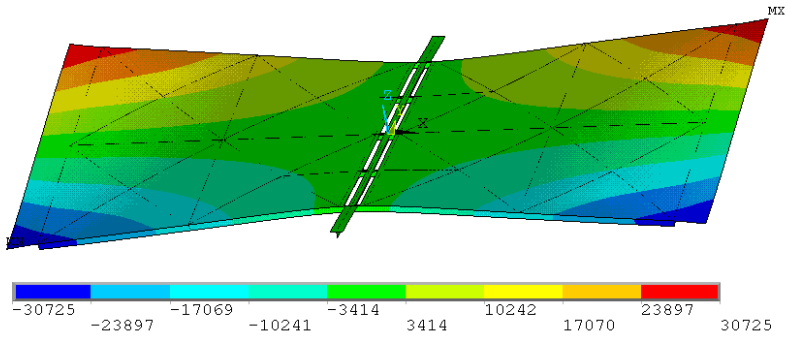


d) $f_4$ = 34 kHz

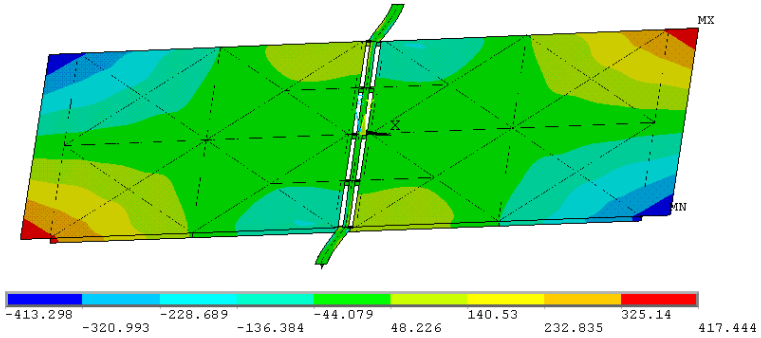


e) $f_5$ = 45 kHz

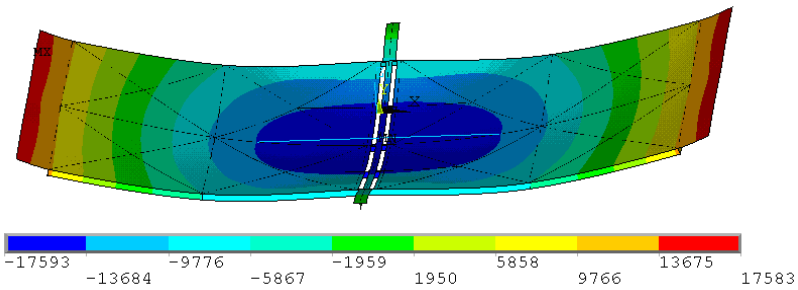


f) $f_6$ = 48 kHz

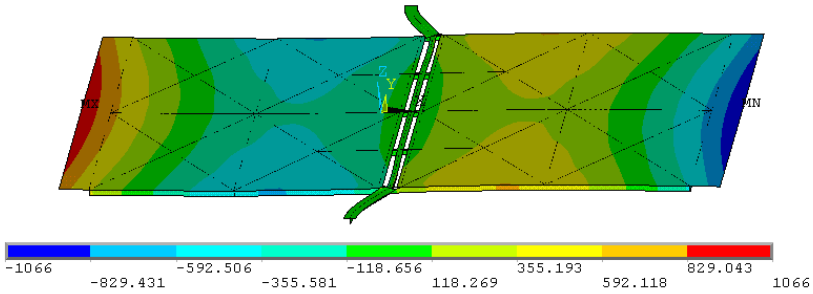


g) $f_7$ = 57 kHz

Figure 12: FEM simulation of the first 7 mode shapes and corresponding mode frequencies of the biomimetic gradient microphone diaphragm

In the audible frequency range (20Hz-20000Hz), the biomimetic diaphragm has two vibrational mode shapes as seen in Figure 12a and 12b. The first mode has a rocking motion in which two sides of the diaphragm rotate about the central pivot in opposite directions responding to the pressure gradient due to difference in pressure on each side of the diaphragm. The resonance frequency of this mode is around 800 Hz. The second mode shown in Figure 12b is the in-phase mode, in which the diaphragm tries to move up and down responding to the average pressure over the diaphragm. However, since the pivots, which hold the diaphragm from the center, are rigid, the in-phase mode looks like a flapping mode. The resonance frequency of this undesired mode is around 14 kHz. These two modes dominate the behavior of the microphone diaphragm in the audio band. The effect of higher order mode shapes is discussed in detail in Chapter 4 which introduces a detailed model of the gradient microphone.

The slits and the stiffeners on the diaphragm are designed to enhance the directional response of the microphone. The model of the diaphragm with a zoomed in view is shown in Figure 13. To suppress the $2^{nd}$ mode sensitivity, the slits are used for allowing air movement between the front side and back side cavity. This air movement causes the second mode to be less sensitive by decreasing the average pressure difference between the front and backside of the diaphragm, which drives the second mode. The other feature that is used to suppress the second mode movement is the stiffeners, which adds extra rigidity to the diaphragm's in phase motion. Figure 13 shows the stiffeners on the backside of the diaphragm.

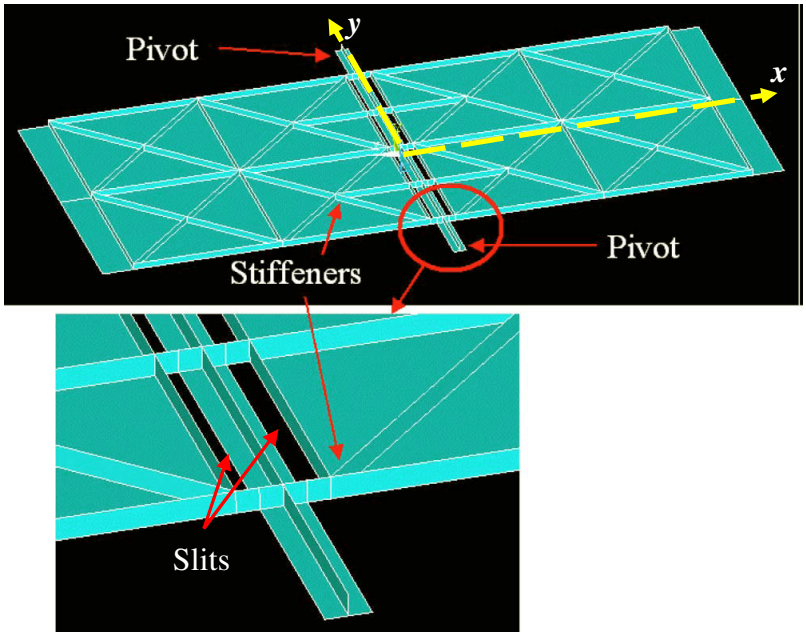


Figure 13: Design model of the biomimetic microphone diaphragm and the zoomed in view around the pivot to show the stiffeners and slits [18]

A simple two degree of freedom model has been used to predict the response of the microphone. The detailed derivation of the transfer functions for the two mode shapes are described elsewhere [18]. Assuming an incident sound wave coming from the x-direction shown in Figure 13, the transfer function of the first mode is given by;

$$H_{pt} = \frac{\frac{i\omega I_A}{cI_{yy}}}{(\omega_r^{\,2} - \omega^2) + 2i\omega_r \xi_r \omega} \tag{8}$$

where $H_{pt}$ is the transfer function between the applied pressure and the rotational angle of the diaphragm in rad/Pa, $I_{yy}$ is the mass moment of inertia, $I_A$ is the area moment of inertia of the rectangular diaphragm with width $b$ and length $L$ about the axis of rotation ($I_A = bL^3/12$), $\omega_r$ is the resonance frequency of the first mode and $\xi_r$ is the damping ratio of the first mode. By using the same analogy, the transfer function of the second mode can be written as;

$$H_{px} = \frac{bL/m_{eq}}{(\omega_t^2 - \omega^2) + 2i\omega_t\xi_t\omega} \quad \textbf{(9)}$$

where $H_{px}$ is the transfer function between the applied pressure and the displacement of the diaphragm in the second mode in *m/Pa*, $m_{eq}$ is the equivalent mass of the diaphragm, $\omega_t$ and $\xi_t$ are the resonance frequency and the damping ratio of the second mode respectively. Using the two transfer functions from Equations 8 and 9, the response at the one end of the diaphragm can be written as;

$$H_p = \frac{L}{2}H_{pt} + H_{px} \quad \textbf{(10)}$$

where $H_p$ is the response at the end of the diaphragm in *m/Pa.* The magnitude and the phase of the predicted responses are plotted in Figure 14. This predicted plot shows that the overall response of the microphone is dominated by the first mode motion around its resonance frequency, around 800Hz. The sensitivity of this mode decreases as the frequency goes down. The second mode which is sensitive to pressure over the diaphragm becomes significant in the overall response at frequencies below 200 Hz and above 4 kHz. This response prediction shows that the frequency range in which these biomimetic directional microphones respond to pressure gradient and have directional output is limited. This limitation, which is mainly a result of the second mode, is investigated more when the characterization of these microphones is discussed.

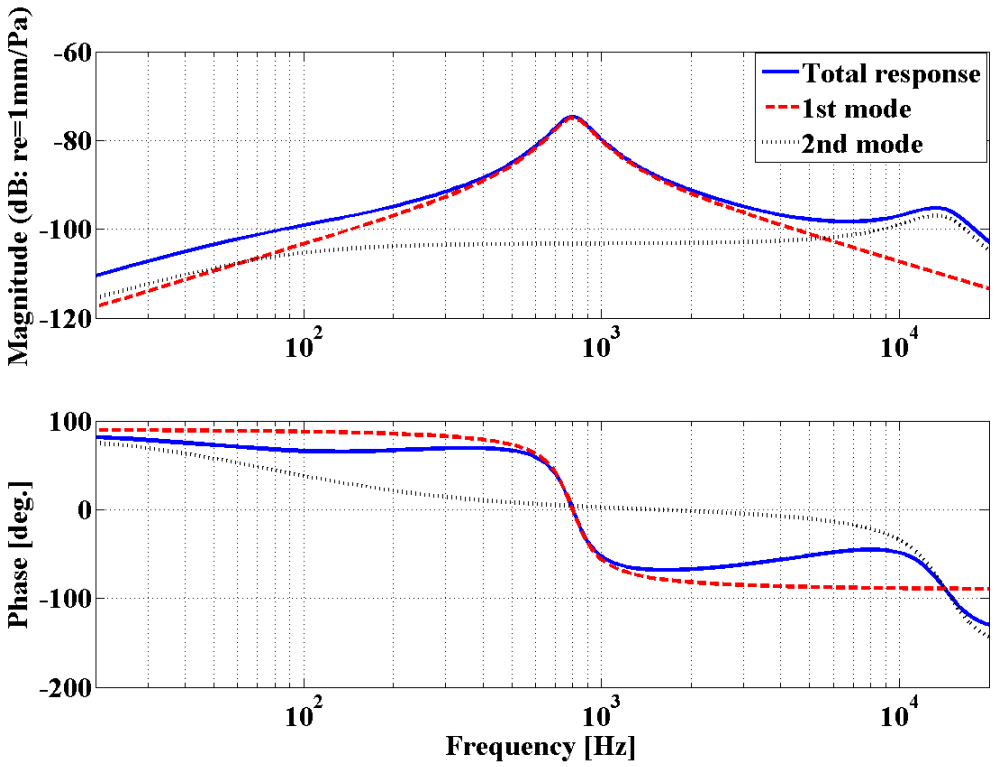


Figure 14: Magnitude and phase response of the biomimetic gradient microphone to the incoming sound wave from the most sensitive direction of the diaphragm (x-direction)

## Integration of Optical Detection with Biomimetic Directional Microphone Structures

The diffraction based optical detection method has been implemented in acoustic sensors using large scale by using external light sources and large scale light detection devices [29]. However, an important challenge of the optical detection method is miniaturization for integration with micromachined sensors. For this purpose, a vertical cavity surface emitting laser (VCSEL) with dimensions of 270μm by 270μm is used as a light source because of size requirements for the integration. These lasers are manufactured by *Lasermate* and have 1.22 mW nominal output power and 850 nm

operation wavelength [54]. Commercially available photodiode dies with dimensions of 250µm by 250µm are used to capture diffracted orders. The photodiodes are selected according to their sensitivities at the operating wavelength of the VCSEL.

The schematic of the optical displacement detection method integrated with the novel biomimetic differential microphone diaphragm is shown in Figure 15. The microfabrication and design details of these differential microphone structures are described earlier [16, 53]. The particular polysilicon diaphragms used in this study have lateral dimensions of 1mm x 2mm and their thickness is in 1-2µm range. As shown in Figure 15, the diaphragm is supported by the center with hinges which serve as torsional springs. The moving gratings at each end of the diaphragm have 4µm periodicity. Fixed gold reflector structures attached to the substrate are used for both as a reference reflector and as the rigid electrode of an electrostatic actuator (the diaphragm is the "moving" electrode). The backside of the diaphragm is open, enabling the laser light to illuminate gratings.

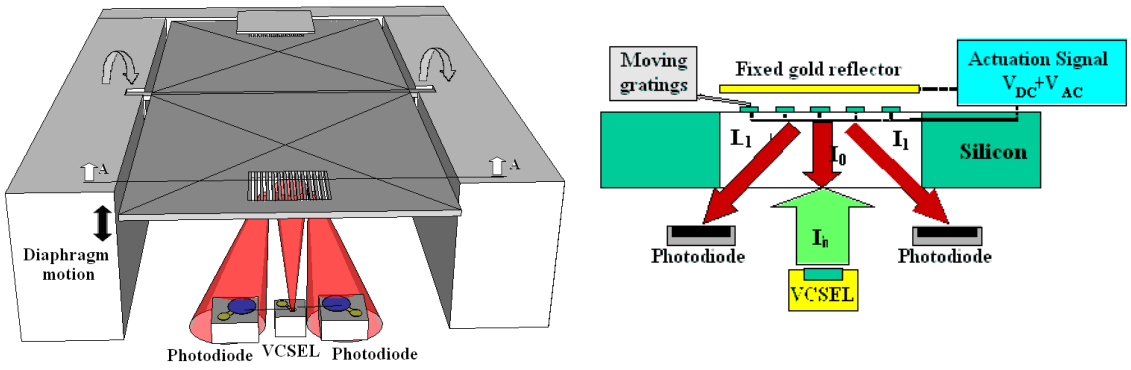


Figure 15: 3D model of the differential microphone diaphragm with integrated optical detection (left, not drawn to scale) and schematic view of cross section-AA (right)

This integration scheme enables the use of these micromachined microphones for measurement microphone and hearing aid applications. Figure 16 shows the packaging steps involved. The picture on the left of Figure 16 shows the parts that are used. In this package, a transistor outline header (TO-header) is used as a base structure to hold the optoelectronics components, custom made printed circuit board (PCB) and the SLA spacer used for holding the microphone structure. A routing PCB is placed on the TO-header, which is 12.7 mm (1/2 inch) in diameter to access signal outputs.

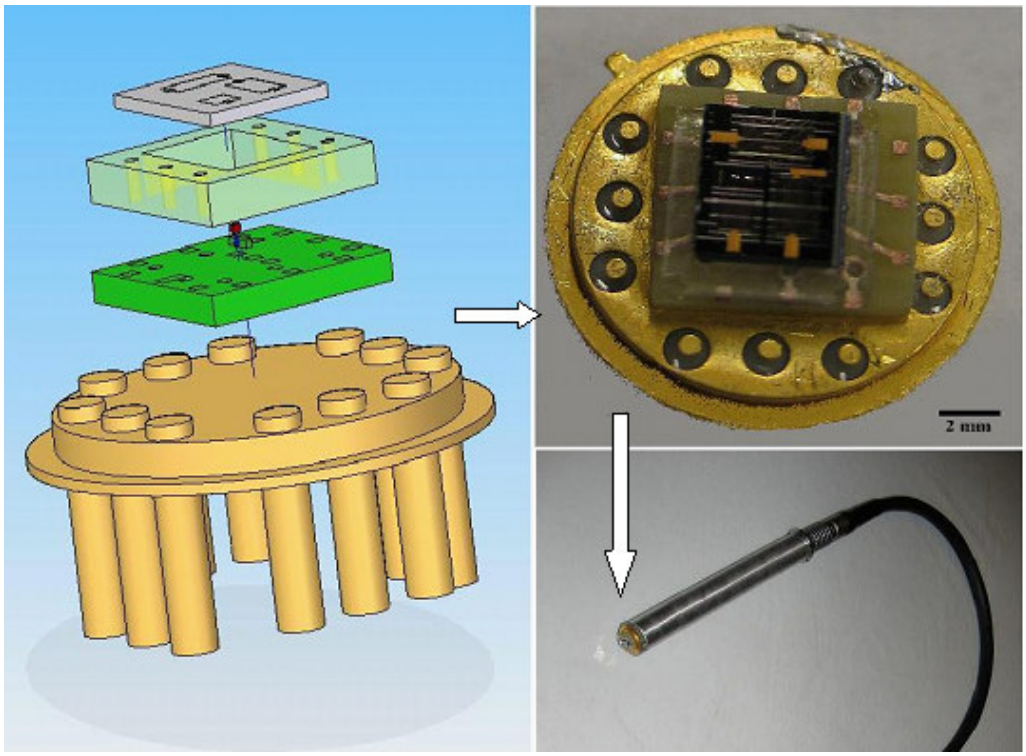


Figure 16: 3D model of the packaged microphone with integrated optoelectronics components (left). The picture of fully integrated directional microphone head (upper right) and the picture of integrated microphone head with the electronics tube and the standard 12-pin LEMO connector and cable (lower right).

After placing the photodiode, the laser light source, VCSEL, is placed and wirebonded. SLA spacer is used for holding the microphone chip in place. The thickness of this SLA piece is designed such that the optimum order separation of the reflected light beam is achieved. This optimum height of 600μm is found by the optical model as described in the next section. The picture on the upper right of Figure 16 shows the packaged differential microphone with optoelectronic components. This packaged microphone header fits into the custom made tube which contains the trans-impedance amplifiers and the necessary electronic components to drive the VCSEL. The picture of this electronics tube attached to the standard 12-pin LEMO connector can be seen from the lower right of Figure 16. The final step is to wirebond the device in order to access the electrostatic ports. This allows the application of electrostatic actuation and force feedback signal to microphone electrodes. The dimensions of the final integrated package which contains 2 directional and 1 omnidirectional microphone, shown in Figure 16, is 8mm x 8mm x 2mm.

There are numerous advantages in using the optical detection method with the biomimetic microphone structures. Since the dominant diaphragm motion consists of pure rocking about the central axis, the volume of the air-filled space under the diaphragm does not change, minimizing the squeeze film damping effect [18]. Combining this novel microphone design that has low thermal mechanical noise levels with the optical detection method makes small sized, high sensitivity and low noise directional microphones feasible [18, 55].

Another important advantage of using an optical detection method is that the electrical port of the microphone is left open. With this port, electrostatic actuation is

possible and can be used for tuning the diaphragm position to get the highest sensitivity and applying the force feedback active control operation to alter device dynamics in a desired manner [56, 57].

## Characterization of Biomimetic Optical Directional Microphones

Acoustic characterization of the biomimetic directional microphone is performed in an anechoic chamber in order to eliminate reflections and ambient noise sources from the microphone response. In this characterization, the sensitivity, noise and directionality of the microphone are measured. A Larson Davis model 2541 microphone is accurately calibrated and used as a reference microphone for these measurements.

First step in characterization is to find the optical modulation curve of the microphone in order to calibrate and optimize the sensitivity. For this purpose, the diaphragm is actuated using electrostatic forces by applying a DC bias. The output voltage obtained from a photodiode capturing a single diffracted order is collected as a function of the applied DC bias. Then the diaphragm position is tuned to its most sensitive position using the DC bias. The acoustic sensitivity of the directional microphone, which is the voltage output per sound pressure input, is measured using a broadband signal and can be seen from Figure 17. At low frequencies, the acoustic sensitivity of the directional microphone is low, as expected. Around 720 Hz, diaphragm has highest sensitivity because of the first mode resonance. This high resonance causes transient ringing and low dynamic range. The dynamic range at the 1$^{st}$ resonance frequency is calculated to be 92 dB.

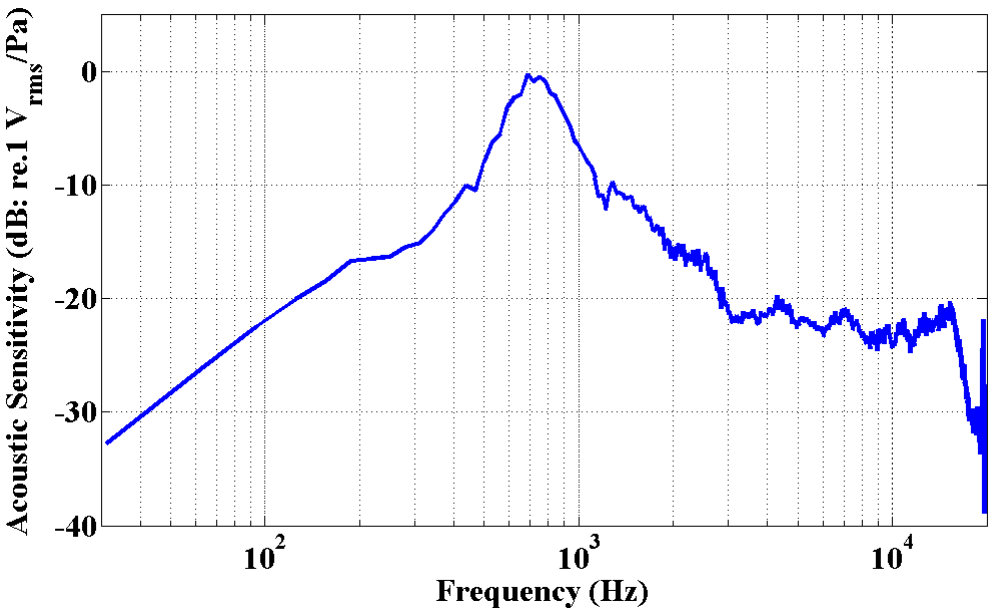


Figure 17: Measured acoustic sensitivity of the optical directional microphone as a function of frequency

Since the optical detection method enables electrostatic actuation, an alternative way to characterize these optical microphones is to measure the electrostatic frequency response without applying any acoustic signal. The measured electrostatic frequency response is plotted in Figure 18. In this measurement, a chirp signal is applied electrostatically, and the transfer function between the output of the microphone and the input chirp signal is analyzed with a signal analyzer.

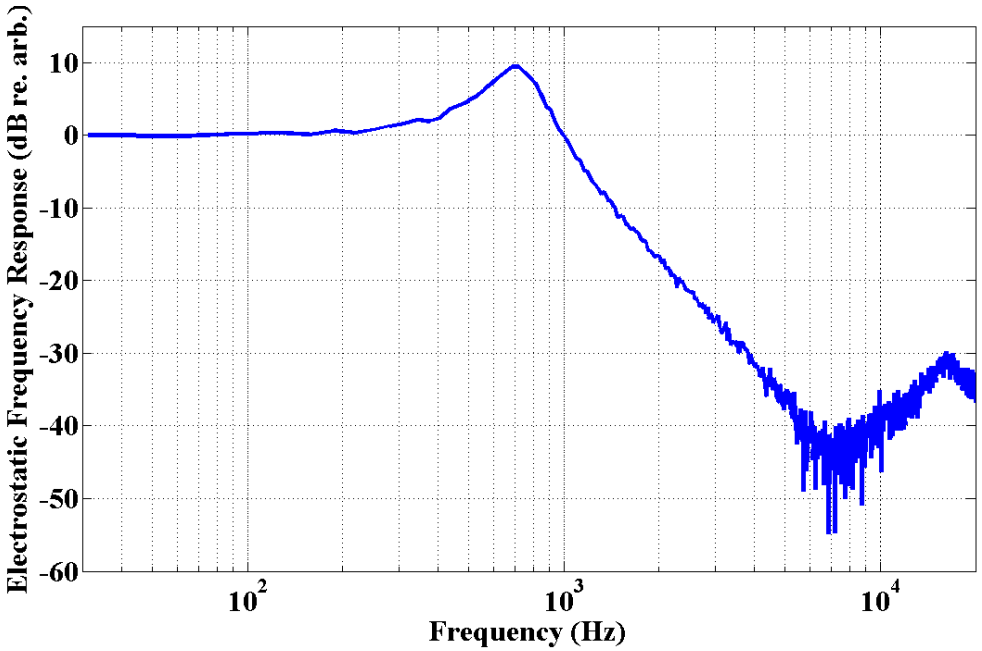


Figure 18: Measured electrostatic frequency response of the optical directional microphone with applied chirp signal

The next step of the characterization procedure is to get the directionality pattern of the integrated directional microphone. In order to measure the directionality, the microphone is placed on a rotation stage, driven by a motion controller. A pure tone signal at 720 Hz, the resonance frequency of the microphone diaphragm, is applied from a speaker while the microphone is rotated 360° by 3° increments. Figure 19a shows the directionality response of the biomimetic gradient microphone at the first resonance frequency, which shows a pattern similar to an ideal "Figure-8" pattern. When the sound source is at 90° or -90°, the response reaches its minimum because the pressure on each side of the diaphragm is nearly equal. However, this directionality response is highly dependent on the frequency of the acoustic wave. In the earlier response prediction, it is shown that the biomimetic gradient microphone responds to the average pressure instead of the pressure gradient because of the second mode movement. In order to test the

second mode effect on the directionality pattern, the directionality test is repeated at 3000 Hz, away from the first resonance frequency. The directionality plot at 3000 Hz is shown in Figure 19b. In this plot, the response goes to its minimum value at 90° or -90° showing directional response. However, there is an offset at these minima which comes from the second mode movement. Since this mode responds to pressure gradient like an omnidirectional microphone, the directional response starts to deviate from ideal "Figure-8" pattern as shown in Figure 19b. Also the directionality plot becomes asymmetrical which is described in Chapter 4.

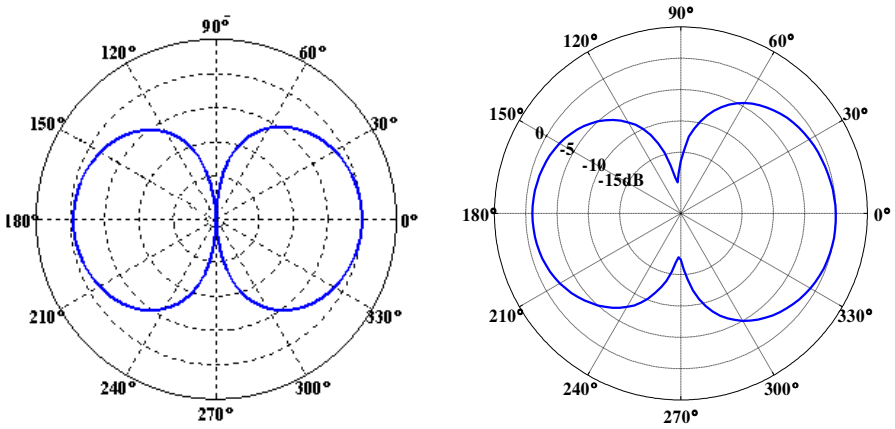


a) b)

Figure 19: Measured directivity plot of the optical directional microphone with applied pure tone signal a) at 720 Hz and b) at 3000 Hz.

After finding the sensitivity and directionality of the gradient microphone, the last characterization step is to obtain the pressure noise spectrum from the measured voltage noise. After filtering pressure noise spectrums by A-weighting filter, the measured noise level of the gradient microphone, plotted in Figure 20, is found to be 36 dBA.

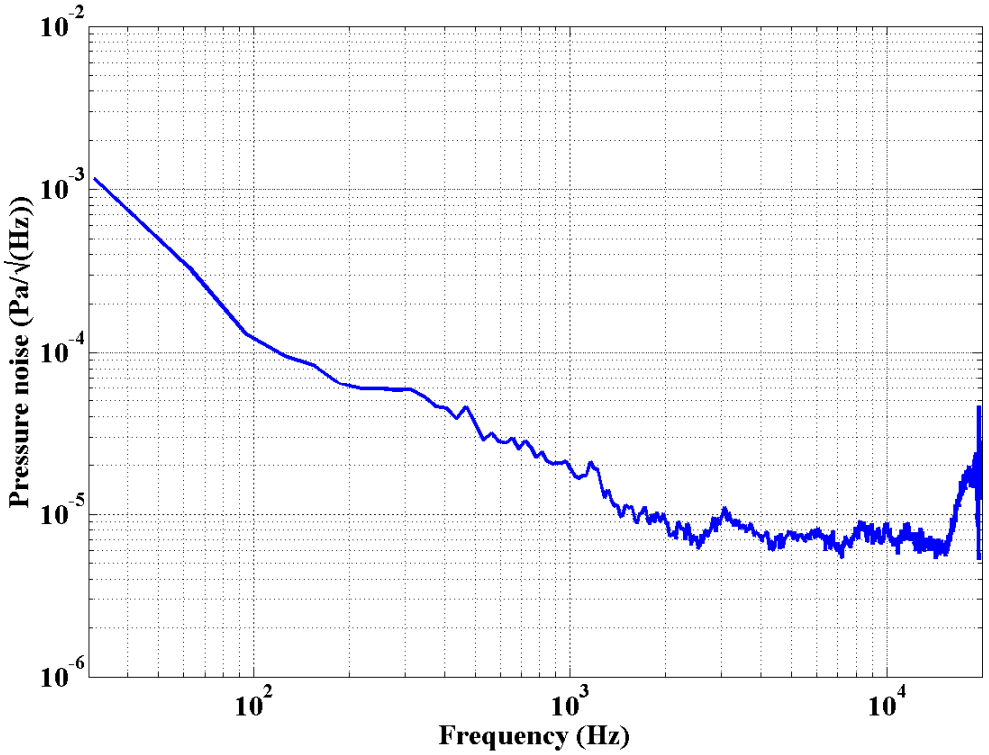


Figure 20: Measured pressure noise of the differential microphone as a function of freq.

This noise level, achieved with only 1mm port spacing, is superior when compared to the current directional microphone technology which uses two omnidirectional microphones that are put side by side with a spacing. The comparison of the noise levels is shown in Figure 21. Especially in the low frequency range, up until 3 kHz, the noise floor of the optical gradient microphone is lower then the current directional microphone with 10mm port spacing. For the overall audio band, the noise level of the gradient microphone is 12 dB lower than the current directional microphone.

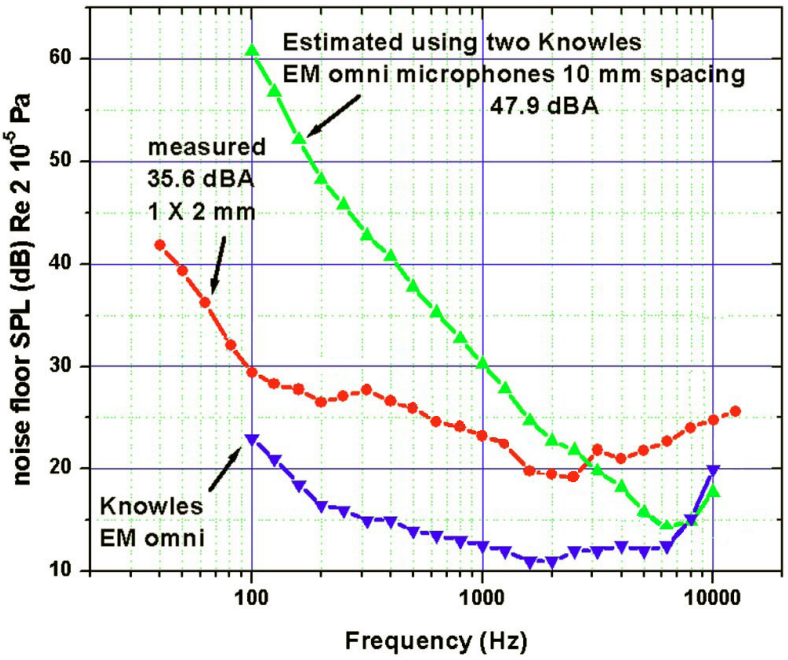


Figure 21: Noise comparison of the biomimetic gradient microphone (with 1mm port spacing) with current directional microphone (with 10mm port spacing)

To see if the noise level is limited by the thermal mechanical noise of the diaphragm or the detection method, the displacement noise comparison is shown in Figure 22. The solid curve is the measured displacement noise of the microphone showing the first resonance peak around 720 Hz. The dotted curve shows the predicted thermal-mechanical noise limit of the diaphragm. From these plots, it can be concluded that from 100 Hz to 2 kHz, the noise is limited by the thermal-mechanical noise. The shot noise limit, as shown with the dashed curve in this figure, is much smaller than the diaphragm's mechanical noise until 4 kHz.

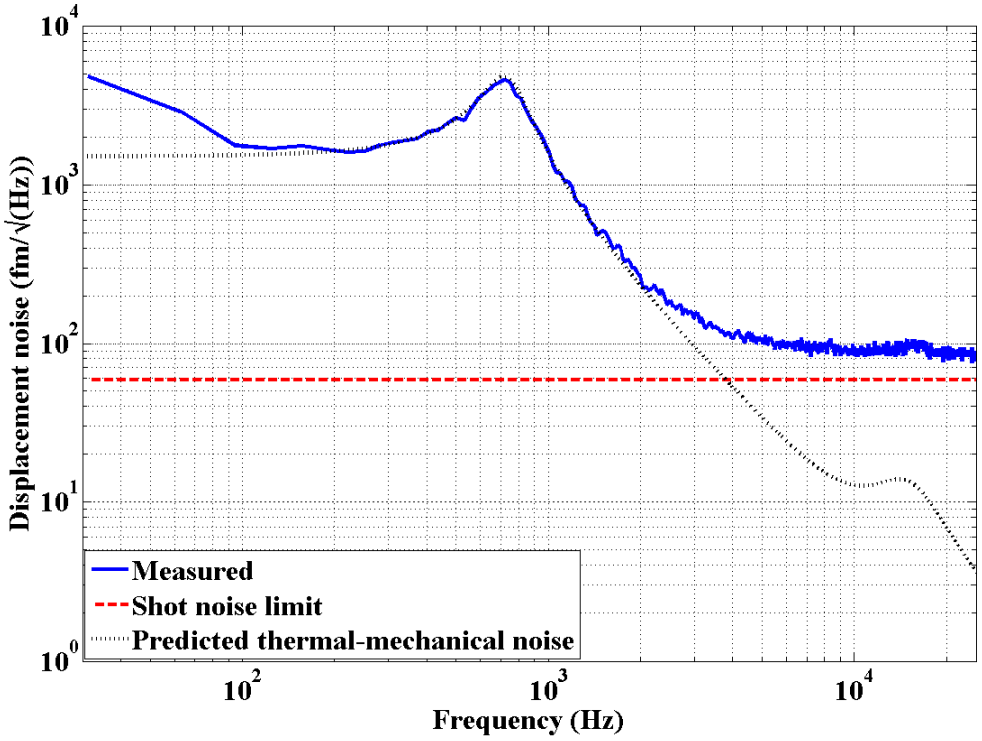


Figure 22: Measured displacement noise of the differential microphone compared with the calculated shot noise and predicted thermal-mechanical noise limits

Since the optical detection method enables measurement of the displacement of microphones with minimum electronic noise, the total noise of the system is dominated by the thermal noise of the microphone diaphragm. The thermal noise floor of the microphone can be lowered by minimizing the passive damping of the microphone structure. However, this will result in an even stronger resonance, resulting in transient ringing and low dynamic range, which are not desirable.

Although the optical detection method gives acceptable results with the integrated biomimetic directional microphone, it needs improvements in terms of efficiency. With the current design, 20μW incident laser power is measured on the single photodiode from a VCSEL light source, having 2mW nominal laser output power. This sets the overall

efficiency of the optical detection method to be 1%. This low efficiency mainly comes from two problems. The first problem in the integration of the optical detection method with the directional microphones comes from the manual positioning of optoelectronic components and manual aligning of the microphone diaphragm-grating pair with respect to the optoelectronic components. Misalignments and small tilts in the integration and positioning of components can degrade the efficiency of the optical detection method. These misalignments and tilts can also come from the micro-fabrication of microphone structures. Because of the stress issues, it is hard to have perfectly flat membranes and gratings. As a future work, using a pick & place system instead of manual positioning is suggested to get better alignments. The other problem comes from the diverging behavior of the VCSEL that is used as a light source. Since there needs to be an optimum space between the optoelectronics plane and the membrane plane, the small divergence angle of the VCSEL can result in a large laser spot on the grating plane because of the propagation. If the laser spot is larger than the grating area, reflection from the diaphragm that is outside of grating areas occurs. This is not desirable because the directly reflected light does not interfere with the diffracted light and can cause lower power efficiency of the optical detection method. Because of these issues, a detailed optical model needs to be developed, and the performance of the optical detection method with this model should be investigated.

## Optical Modeling

The power efficiency of these optical microphones is important, especially for applications like hearing aids, which are operated with batteries. Since the optical source

is the most significant factor in power consumption, the overall power efficiency of the optical detection method needs to be analyzed. For this purpose, a detailed optical model to calculate the optical fields at different observation planes is developed. An earlier model, based on ABCD matrix formulation, was described and used for predicting an initial approximation of the optical field [58]. However these earlier models did not consider the finite size and the non-ideal shape of gratings and the gold reflector. To account for these factors, a new optical model is developed. The finite size of the gratings is significant especially if the optical beam is highly divergent as in the case of a VCSEL with small aperture. The second factor is the non-ideal shape of the grating and the gold reflector, namely these surfaces being not perfectly flat or parallel to each other, which is the case in practice.

The parameters used in the current optical model are summarized in Table 1, and the code of the model is given in Appendix B. The optical field profile at the output of the VCSEL aperture is assumed to be Gaussian in the radial direction. To retrieve the field profiles of the VCSEL light as it propagates through the distance between the VCSEL aperture and the grating plane, the model employs the Fresnel (near-field) approximation to the Huygens-Fresnel diffraction integral [59]. In the Fresnel approximation, 2-D Fourier Transform is used because of the non-symmetrical geometry caused by gratings. The finite grating size is implemented in this model using a windowing function.

Table 1: Parameters used in optical modeling

| | |
|---|---|
| VCSEL operating wavelength, | $\lambda = 850$ nm |
| VCSEL nominal output power, | $P_0 = 1.25$ mW |
| VCSEL beam waist size, | $w_0 = 2.27$ μm |
| Distance from plane of VCSEL aperture to plane of grating, | $z = 900$ μm |
| Distance from plane of grating to plane of photodiode array, | $L = 850$ μm |
| Tilt angle of reflective gold reflector, | $\theta = \tan^{-1}(3/80)$ |
| Gap between grating plane and point on reflector closest to grating plane, | $d_0 = 2$ μm |
| Grating $x$-dimension, | $g_x = 100$ μm |
| Grating $y$-dimension, | $g_y = 100$ μm |
| Grating period, | $\Lambda = 4$ μm |
| Grating offset from center in $y$-direction, | $y_0 = -50$ μm |
| Points defined in $x$-direction, | $N_x = 2048$ |
| Points defined in $y$-direction, | $N_y = 2048$ |

After finding the field on the grating plane, it is observed that the size of the VCSEL beam arriving at the grating plane depends on the full width at half-maximum (FWHM) divergence angle of the VCSEL. Having a beam larger than the size of the grating causes reflection from areas outside of the grating area. To account for the reflectivity of the region outside the finite grating, the field that is not captured in the grating is reflected back from the diaphragm. As a result, the field arriving at the photodiode plane is the summation of the field arriving from the windowed finite grating and the field arriving from the region outside the grating. While calculating the field arriving from the finite grating, diffraction of the beam between the grating plane and the

gold reflector is ignored. Since the distance between the grating plane and the gold reflector is small compared to other distances, basic ray theory is used for that region.

The optical field profiles arriving at the photodiode plane are found using the optical model and can be seen in Figure 23. All the plots are obtained by assuming that the gratings and the gold reflector are flat and perfectly parallel to each other.

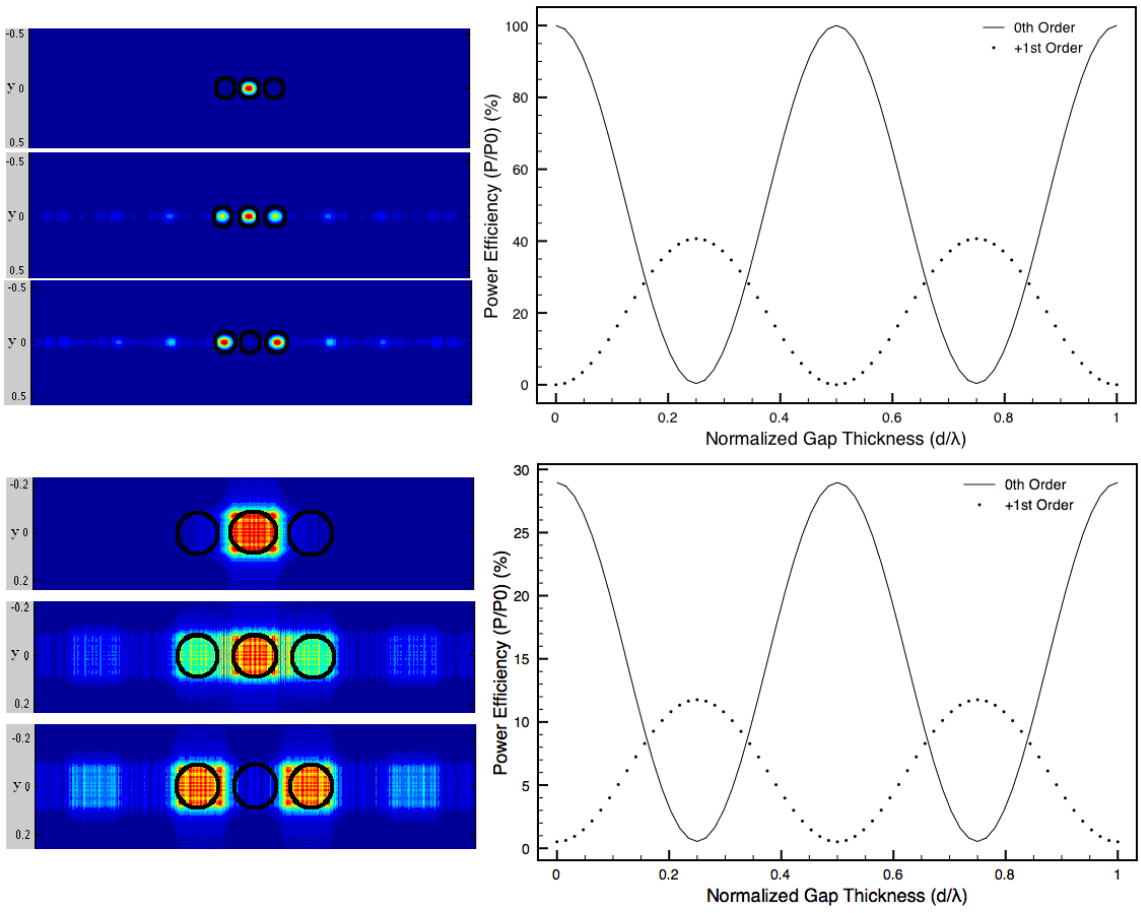


Figure 23: Profile of field arriving at photodiode plane with low divergence (upper left) and high divergence angle (lower left).Acquired phase shift in gap between grating plane and the gold reflector, top to bottom: Ø= 0, Ø = π /2, and Ø = π. Circles show the active regions of photodiodes for detecting the diffracted orders. Effect of modulating gap thickness d on retrieved optical power for the $0^{th}$ and $+1^{st}$ order is plotted with low divergence (upper right) and high divergence angle (lower right).

The plot on the upper left shows the optical field profile when the divergence angle of the VCSEL is low. When the phase angle between the grating plane and the gold reflector is zero, i.e. $\phi = 0$, the structure acts like a perfect mirror and all the light is reflected back as a zero order output, which can be seen from the top plot. When $\phi = \pi$, the light is reflected back as first orders which can be seen from the bottom plot. The plot on the lower left shows the optical field profile with the same structure when the divergence angle of the VCSEL is large. This case is more realistic if the output characteristic of the VCSEL used in the current design is considered. Because of this diverging behavior, the beam that arrives to the grating plane is much larger than the size of the grating area. The schematic and the picture of the diverging beam on the grating plane are shown in Figure 24. As a result of this behavior, the plot on the lower left of Figure 23 shows the reflected orders in square pattern. Circles on these plots show the active area of photodiode positions which are positioned at points corresponding to ($x$, $y$) = (±200 μm, 0 μm) for the 1$^{st}$ orders and (x, y) = (0 μm, 0 μm) for the 0$^{th}$ order.

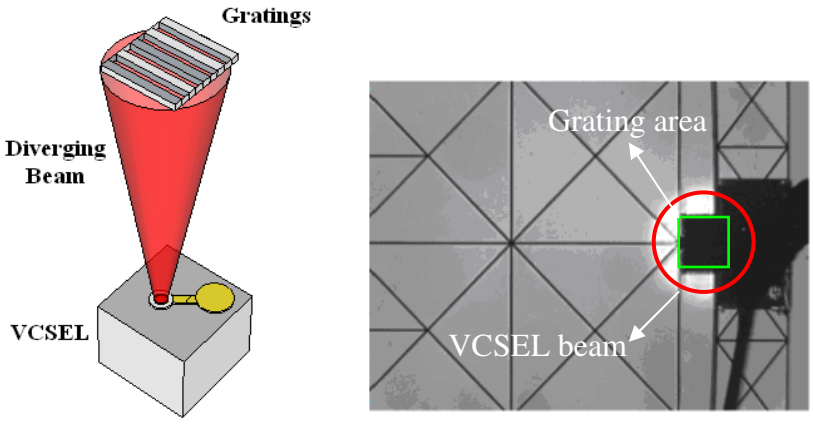


Figure 24: The schematic showing the diverging beam on the grating plane (left) and the captured microscope image showing the relative dimensions (right)

Although the model can handle reflection from outside of the grating, the reflectivity of the region outside the finite grating is taken as 0 for simplicity. In order to examine the effect of modulating the initial grating-membrane distance $d_0$ and the overall efficiency of the method, the power arriving at each photodiode is swept for a range of initial gap thicknesses $d_0$. The power arriving at photodiodes is calculated by integrating the optical field on the active region of photodiodes. By sweeping the parameter $d_0$ over a range of values and calculating the power arriving at the photodiodes, the effect of modulating the gap distance (i.e., optical modulation curves) can be retrieved. The optical modulation curves for low divergence (upper right) and high divergence angle (lower right) can also be seen from Figure 23. In both these plots, $1^{st}$ order and $0^{th}$ order curves are perfectly out of phase. The power efficiency of the $0^{th}$ and $1^{st}$ orders decreases from 99% to 29 % and 40% to 12% respectively when the VCSEL divergence angle increases from 1.5˚ (low divergence) to 8˚ (high divergence). The decrease in efficiency results from the overlapping of the diffracted orders in the *x*-direction when the divergence angle of the VCSEL gets higher. This overlap decreases the retrieved modulation efficiency because of the interference of the orders.

Until this point, all the optical modeling results assume that the grating plane and the gold reflector are perfectly parallel to each other, which is unrealistic. In order to show the effect of the tilt between the grating plane and the gold reflector, the optical model is used with the tilted gold reflector. The plots on the left of Figure 25 show the field profiles of the diffracted orders with different tilt angles when the VCSEL beam divergence angle is low (upper left) and high (lower left). The power efficiency of these

different tilted cases is plotted on the right of Figure 25 with respect to the normalized gap thickness.

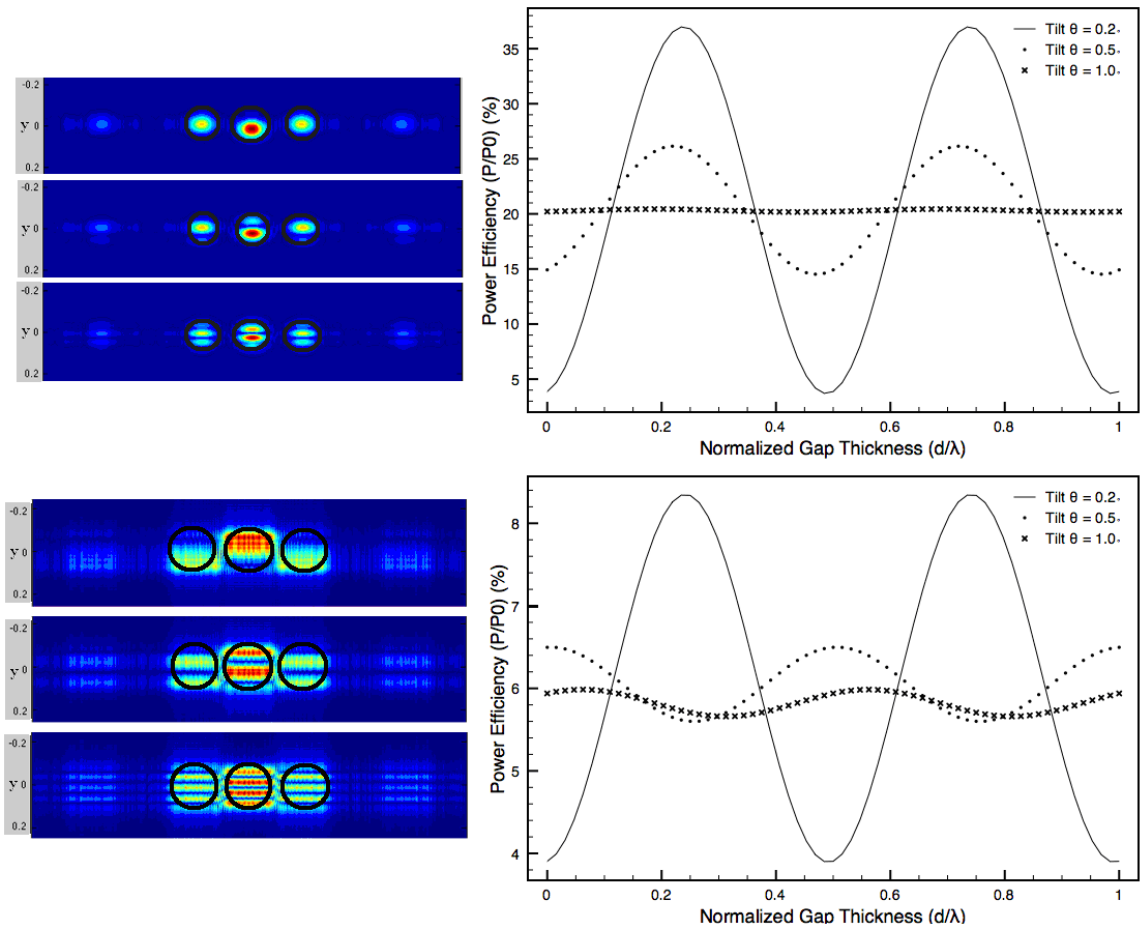


Figure 25: Effect of gold reflector tilt angle on profiles of fields arriving at photodiode plane with low divergence (upper left) and high divergence angle (lower left). Gold reflector tilt angle, top to bottom: θ= 0.2°, θ = 0.5°, θ = 1°. In this case, Circles show the active regions of photodiodes for detecting the diffracted orders. Optical curve generated for the tilted cases with low divergence (upper right) and high divergence angle (lower right) for θ = 0.2°, θ = 0.5°, θ = 1°.

It is obvious from the field profiles that with increasing tilt angle, interference fringes in the y-direction become evident due to the interference of the field arriving from

the gratings and the gold reflector. Power efficiency curves show that with increasing tilt angle, the retrieved power drops because the field arriving from the tilted membrane increasingly does not overlap with the photodiode active area. Also note that the retrieved average power efficiency falls to some DC level due to the constant reflection from the grating fingers as the tilt angle increases. As in the no-tilt case, the overall power efficiency of the high divergence angle case is lower than the low divergence case because of the overlapping of the diffracted orders in the *x*-direction. The solution to this problem is to reduce the VCSEL beam diameter on the grating plane so that the size of the beam is actually smaller than the grating size. Optical elements such as a micro-lense can be used to collimate the beam and decrease the beam diameter. This is one of the possible changes that can be done in the future to increase the efficiency of the optical detection in micromachined microphones.

# CHAPTER 3

# CHARACTERIZATION OF BIOMIMETIC DIRECTIONAL MICROPHONES FOR PARTICLE VELOCITY MEASUREMENT

In the previous chapter, it was shown that optical directional microphones have good sensitivity in measuring pressure gradients which in turn can be used in particle velocity measurement to determine sound intensity. This chapter describes the evaluation of biomimetic optical gradient microphones as particle velocity sensors for sound intensity measurements. For this purpose, a comparative study is performed where the results of the optical gradient microphone are compared with a commercial sound intensity probe and a commercial particle velocity sensor. To perform these measurements, several measurement setups are developed in controlled environments such as a standing wave tube and an anechoic chamber. The experiments are described in detail and the results are presented. It is demonstrated that the gradient microphone is useful for particle velocity measurement in a narrow frequency range, and the problem causing this bandwidth limitation is discussed.

## Measurements in Anechoic Chamber

Characterization of the optical gradient microphone in terms of measuring the particle velocity and the sound intensity was performed in the anechoic chamber. In this characterization, a Larson Davis Model 2260 intensity probe is used as a PP-probe reference. This intensity probe consists of two phase matched microphones and the

spacing between the microphones can be adjusted with different spacers. The relationship between the useful frequency range of the measurement and the spacer dimension was described in Chapter 1. Figure 26 shows the picture of the PP-probe which is mounted on a stand that is placed in front of a sound source. In this configuration, it can be seen that the sensitive direction of the intensity probe is aligned with the normal to the surface of the sound source.

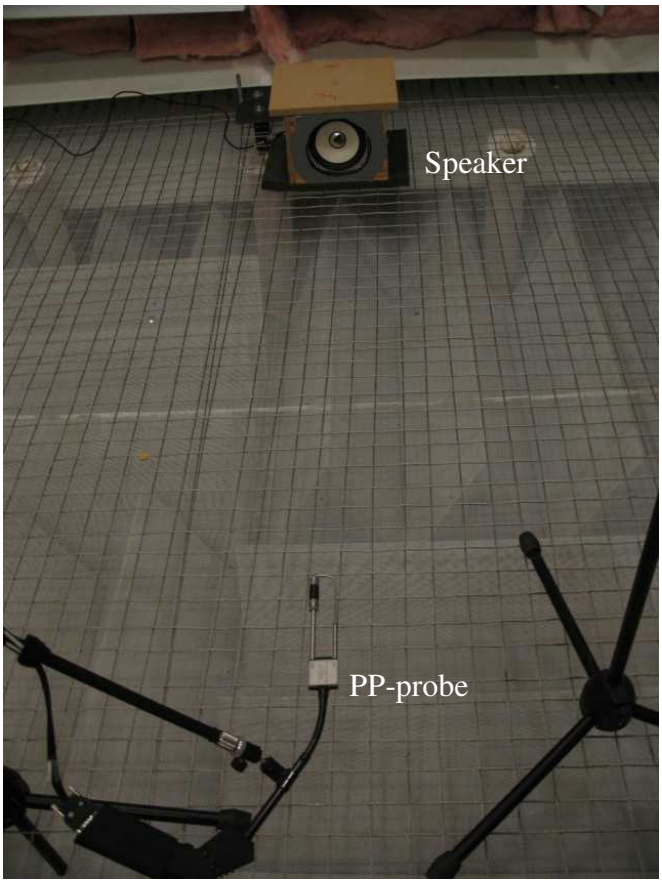


Figure 26: Intensity measurement setup in the anechoic chamber with Larson Davis (LD) Model 2260 PP-probe

A chirp signal is applied from the speaker and the LD PP-probe is used to measure the intensity in the direction of the probe. In order not to disturb the field in the

anechoic chamber, the output of the two channels are taken out of the anechoic chamber and fed into the signal conditioner and analyzer. While keeping all the parameters and configuration constant, the LD PP-probe is replaced with the optical gradient microphone to measure the particle velocity and a LD microphone for pressure measurement. This configuration is shown in Figure 27. The optical gradient microphone and the pressure microphone are placed as closely together as possible. The other important point in this configuration is to align the most sensitive direction of the gradient microphone with the normal direction to the surface of the speaker.

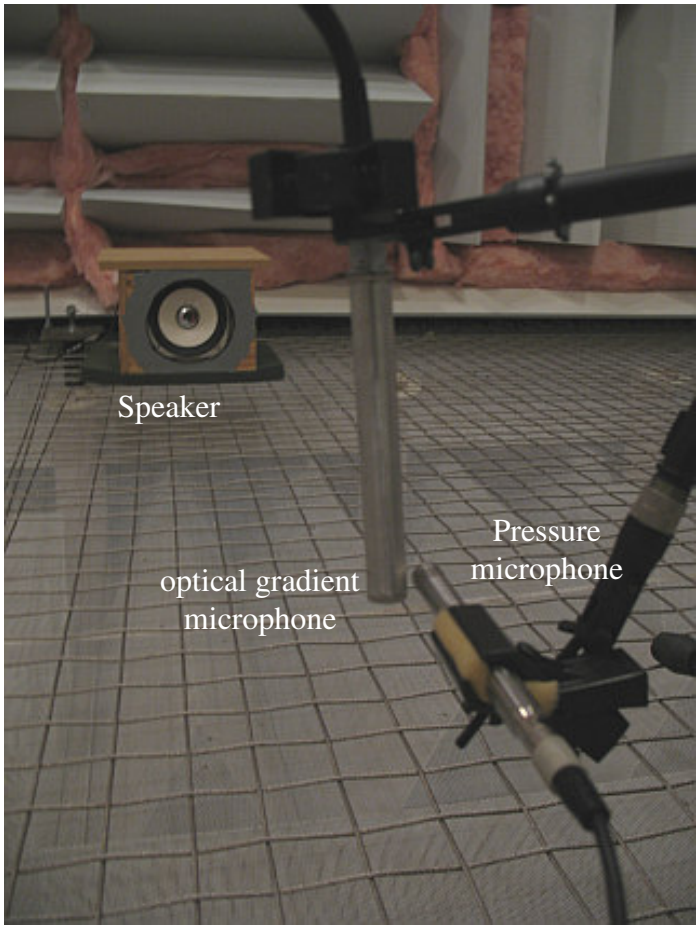


Figure 27: Intensity measurement setup in the anechoic chamber with optical gradient microphone and Larson Davis Model 2541 pressure microphone

For both setups, the sound intensity is calculated from the measured particle velocity and pressure, and the results are plotted in Figure 28. The measured intensities show that the optical gradient microphone combined with a pressure sensor measures the sound intensity similar to the PP-probe between 250 Hz to 3 kHz. In this measurement, 25mm spacing is used with the PP-probe, which sets the useful frequency range of the measurement to be 50 Hz-2.5 kHz. As a result, the difference between the two measurements below 50 Hz and above 3 kHz can be due to the phase mismatch and finite difference approximation error of the PP-probe respectively.

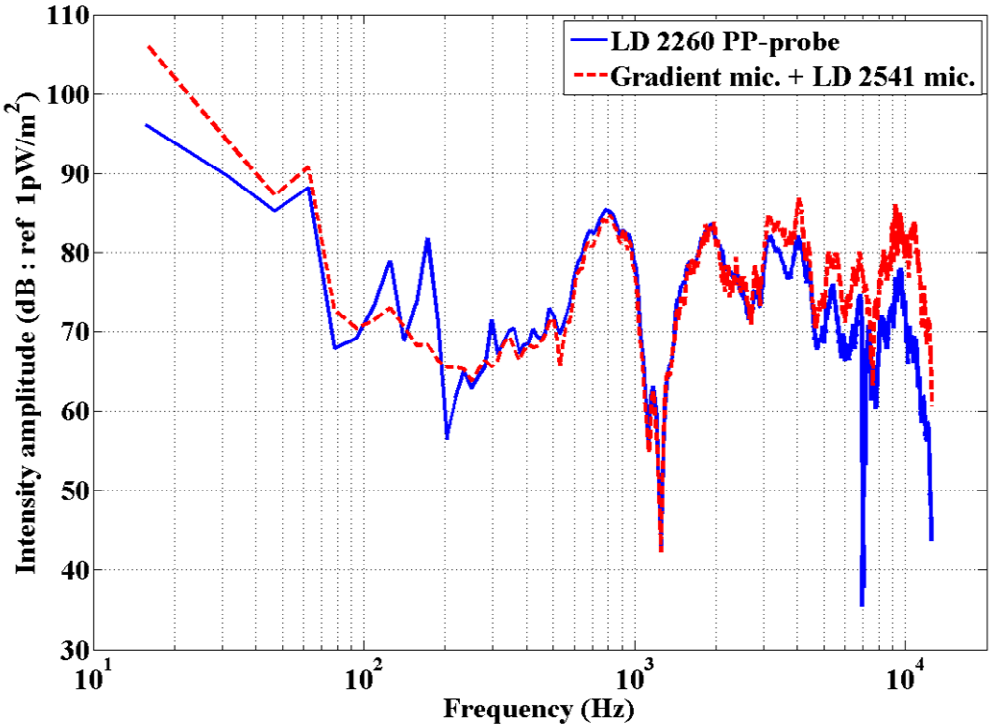


Figure 28: Comparison of measured intensities from LD intensity probe with 25mm spacing and from the combination of optical gradient microphone + LD 2541 microphone

In order to check the difference between the measured intensities at lower and higher frequencies, the 25 mm spacing is replaced by 12 mm spacing, which now sets the useful frequency range to be 100 Hz-5 kHz. The comparison of the measured intensities plotted in Figure 29 shows that there is a better agreement with the measurements from 200 Hz to 4.5 kHz with smaller spacer. This experiment shows that the difference between the measured intensities mainly comes from errors in the PP-probe and by using the optical gradient microphone; one can cover the same frequency range without a need for two separate spacers. In both measurements, from Figure 28 and 29, there is a difference between measured intensities between 100-250 Hz. This difference decreases from 10 dB to 5 dB maximum with decreasing spacer size. In all the measurements with LD probe, spikes and irregularities at these frequencies are observed. These irregularities may be the distortion of the sound field with the presence of probe in the field.

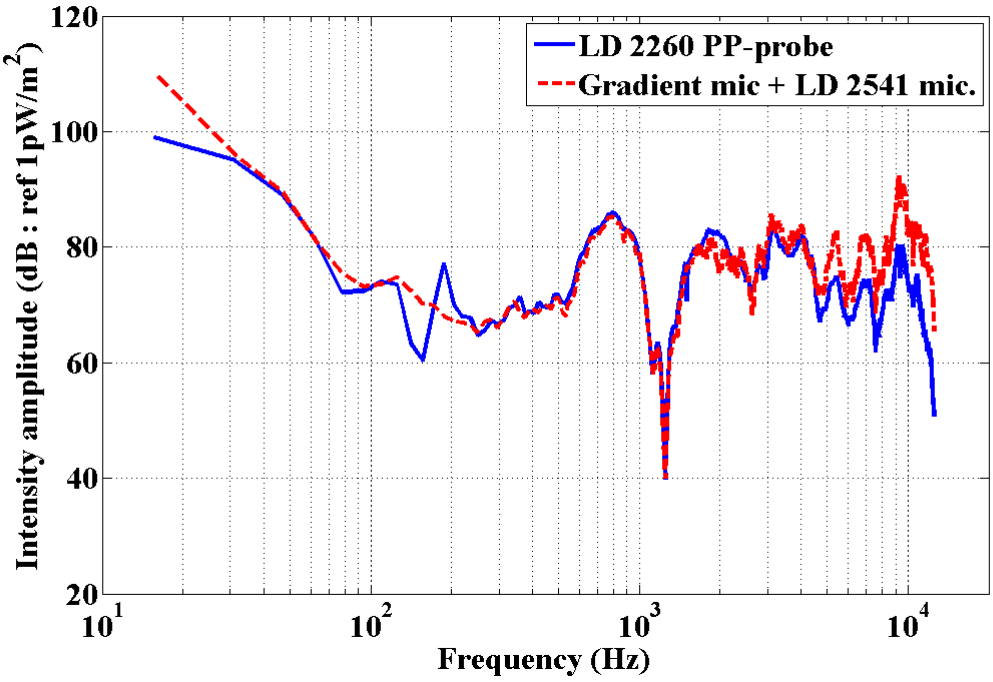


Figure 29: Comparison of measured intensities from LD intensity probe with 12mm spacing and from the combination of optical gradient microphone + LD 2541 microphone

## Impedance Tube Measurements

In order to investigate the ability of the optical gradient microphone to measure particle velocity, a well controlled environment is needed. Pressure is simple to measure using a single pressure microphone; however, measuring the gradient of the pressure, which is used for calculating the particle velocity, is challenging. For this purpose, an impedance tube with alternate terminations is used for creating a medium in which the pressure and velocity are known at every point. Since the relation between the pressure and the particle velocity is known, the gradient microphone can be tested with a pressure microphone to see the accuracy of the pressure gradient measurement.

An impedance tube is a hollow rigid cylinder, with a termination port at one end and a sound source at the other. The picture and a simple schematic view of this impedance tube can be seen from Figure 30.

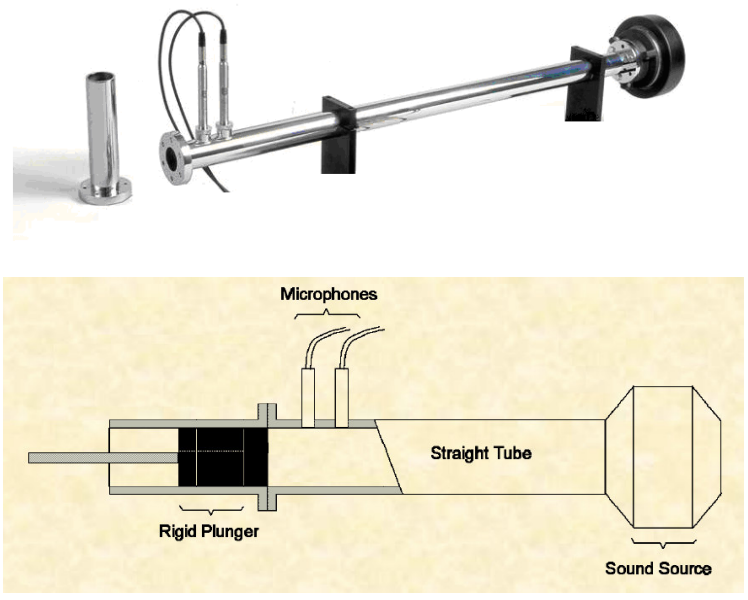


Figure 30: Picture (top) and the schematic (bottom) of the impedance tube.

Microphone ports are mounted at two locations along the wall of the tube. In the top picture of Figure 30, the impedance tube is shown as open ended. A rigid plunger can be used to close that end in order to create a reflection surface. In contrast to an anechoic chamber where all sound is ideally absorbed at the walls, in the impedance tube all sound is reflected if it has a rigid end condition.

Table 2: Specifications and dimensions of the impedance tube

| | |
|---|---|
| Frequency range | 50 Hz – 5700 Hz |
| Maximum SPL in tube | ~ 150 dB |
| Ambient noise in tube | < 30 dBA |
| Microphones accepts standard | ½ inch |
| Tube inside diameter | 34.9 mm |
| Tube outside diameter | 41.3 mm |
| Overall length | 1.20 m (with sample holder) |
| Distance from face to center of downstream port | 50.62mm |
| Distance between two ports | 29.31mm |

Specifications and dimensions of the particular impedance tube used in this study are listed in Table 2. In an impedance tube, which is rigidly terminated with rigged walls, the sound travels only in one dimension and all the sound is ideally reflected back from the end of the tube. However, this assumption is true only for certain frequencies. As a result of this, the most important characteristic of the impedance tube is the frequency range. The lower frequency limit, $f_l$, depends on the spacing of the microphones and the

accuracy of the analysis system. It is recommended that the microphone spacing exceed one percent of the wavelength corresponding to the lower frequency of interest. Also at lower frequencies, small leaks in the microphone mountings can influence the measurements. To avoid these leaking effects, the ports for the microphones have to be sealed with a rubber ring. The upper frequency limit, *fu,* depends on the diameter of the tube and upon the speed of sound. In order to maintain plane wave propagation, the upper frequency limit is defined as follows:

$$f_u \leq \frac{c}{Kd} \tag{11}$$

where, $f_u$ is the upper frequency limit in hertz, $c$ is the speed of sound in the tube in meter/sec, $d$ is the diameter of the tube in meters and $K = 1.71$ [60]. As can be seen from this equation, when the diameter of the tube decreases, the upper frequency limit increases, which means that the frequency bandwidth of the impedance tube is widened. However, since the diameter of the tube should be large compared to the size of the ½ inch microphones, the diameter can not be chosen too small. From the dimensions of the impedance tube that is given in Table 2, the upper frequency is found to be 5.7 kHz.

**Experimental Setup with Impedance Tube**

The experimental setup includes the impedance tube which is described above, two Larson Davis ½ in. (LD2560) random incidence microphones, power supplies for these microphones, SIGLAB hardware and a laptop for data acquisition and signal processing (see Figure 31).

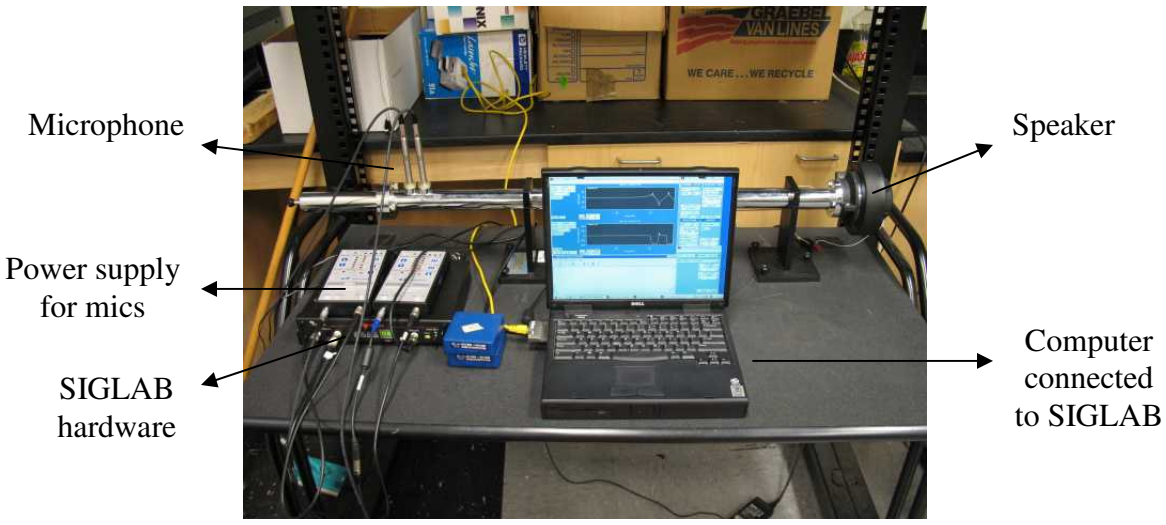


Figure 31: Picture of the impedance tube experimental setup.

In order to fully characterize the impedance tube, the two microphone-method is used [61]. The speaker is driven by a virtual function generator (by SIGLAB) that applies a random signal with a bandwidth of 5.0 kHz. The microphone outputs are recorded and processed for different configurations. When the rigid plunger is used to close the end of the impedance tube, this termination acts like a rigid end (close end case) and when the rigid plunger is not used, the termination at the end of the impedance tube acts like a pressure release end (open end case). Then all the data is collected for those two different configurations by swapping microphones. So the microphone which is in the upstream port (close to the speaker) will be in the downstream port (away from the speaker) and vice versa.

**Signal to Noise Ratio (SNR) Analysis**

SNR is a good indication of whether the measured data is valid or not. First an experiment is done to find SNR values for different configurations mentioned above.

SNR vs. frequency data is plotted in Figure 32. In the close end case, SNR values are larger than 20 dB down to 20 Hz. However this low frequency limit increases to 90 Hz in the open end case. As a result of this, the data is valid at frequencies which are higher than 90 Hz. These SNR values can be increased by increasing the output level of the speaker; however, the pressure inside the tube should be lower than the maximum allowable pressure limit that the microphone can measure without distortion.

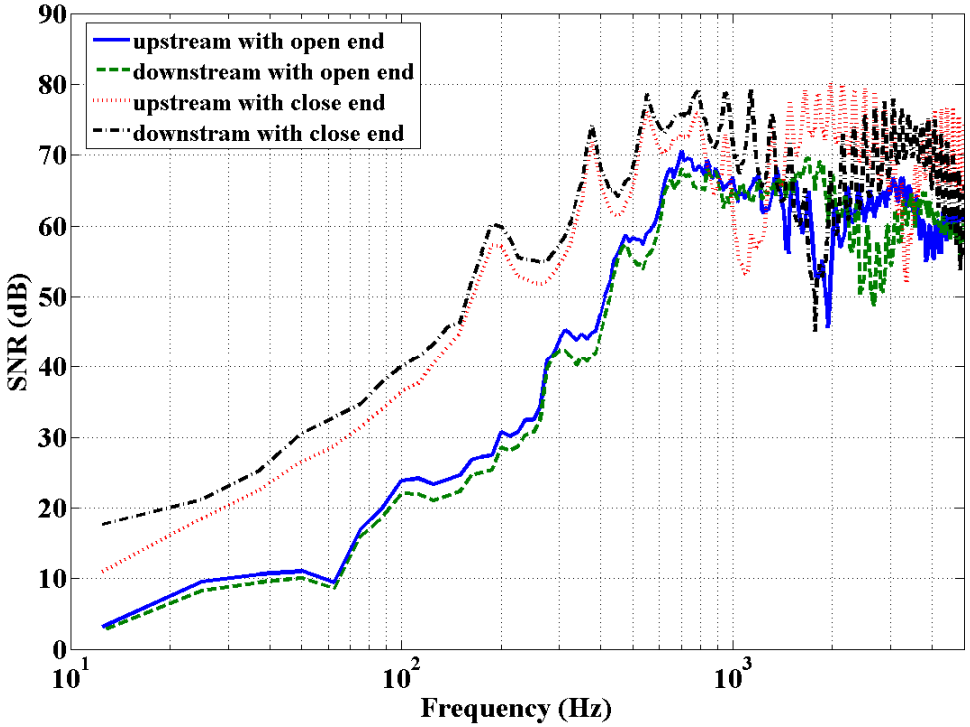


Figure 32: Signal to Noise Ratios at two different microphone ports (upstream, downstream) with two different configurations (open end, close end)

The difference in SNR's between the open end and the close end cases comes from the background noise in the room. The background noise in the tube is higher for

the open end case, which decreases the SNR. However with this value of the background noise, SNR is good enough to continue on characterization of the impedance tube.

**Pressure and Velocity Measurement Analysis**

Using two Larson Davis microphones at two different microphone ports, the pressure at those points is measured. In order to find the particle velocity at these two points, the reflection coefficient should be calculated according to the different end condition configurations. The transfer function method is used to find the reflection coefficient in the tube. Before going into details of the transfer function method, it should be noted that the transfer function is a complex ratio of the acoustic pressure responses and any mismatch in the amplitude or phase responses of the two microphone systems will affect the accuracy of the transfer function measurement. Because of that, the calibration function should be found to compensate for the amplitude and phase mismatch between the two microphones.

The first step in calibration is to measure the transfer function between the two microphones, $H_{12}$. Then the microphones are swapped so that the upstream microphone becomes the downstream microphone. In this configuration, the transfer function between the two microphones, $H_{21}$, is measured again. The calibration factor can be found as:

$$H_{cal} = (H_{12}H_{21})^{1/2} = \left|H_{cal}\right|e^{j\phi_{cal}} \quad \textbf{(12)}$$

The magnitude and the phase of the calibration function are plotted in Figure 33. The magnitude is the correction for the amplitude mismatch and the phase is the correction for the phase mismatch between the two microphones. After finding the calibration factor, the transfer function calculated directly from the complex ratio of the

Fourier transform of the acoustic pressure at the microphone at downstream to the microphone at the upstream can be corrected as,

$$H = \frac{\overline{H}}{H_{cal}} \tag{13}$$

where, $\overline{H}$ is the measured transfer function, $H_{cal}$ is the calibration function and $H$ is the corrected transfer function.

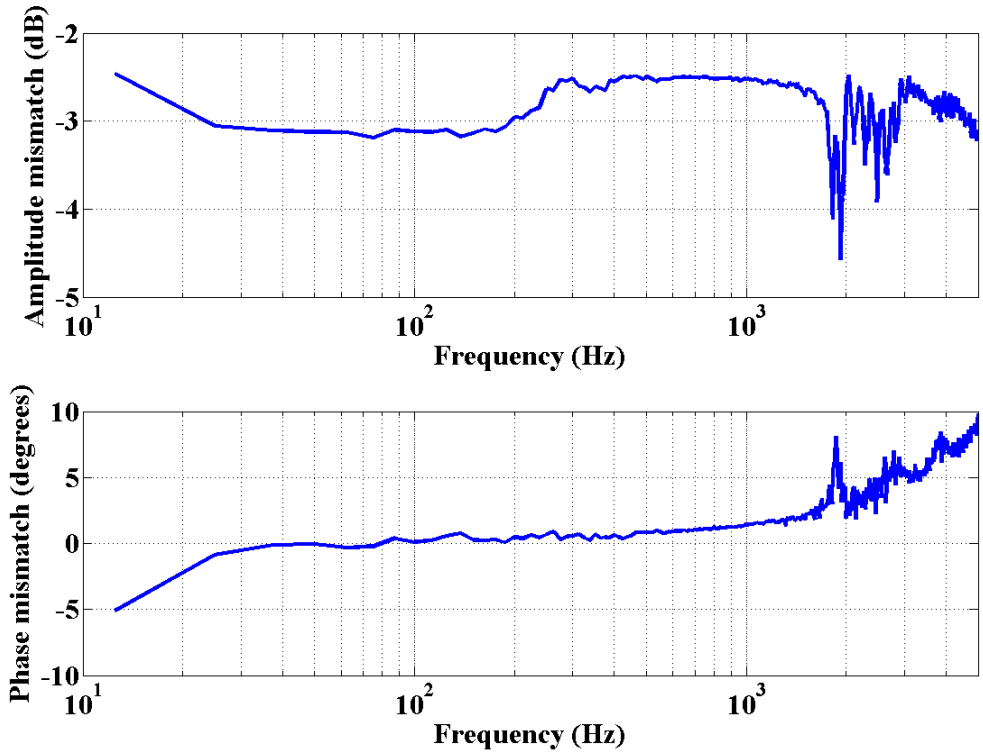


Figure 33: Amplitude (upper) and phase (lower) mismatch between two LD microphones

After getting the corrected transfer functions between the microphones, the reflection coefficient is found as follows;

$$P_{upstream} = P^{+}(e^{jk(l+s)} + R\, e^{-jk(l+s)}) \tag{14}$$

$$P_{downstream} = P^{+}(e^{jkl} + R\, e^{-jkl}) \tag{15}$$

$$H = \frac{P_{downstream}}{P_{upstream}} = \frac{P^{+}(e^{jk(l+s)} + R\, e^{-jk(l+s)})}{P^{+}(e^{jkl} + R\, e^{-jkl})} \tag{16}$$

where, R is the complex reflection coefficient, $l$ is the distance between the tube termination and center of downstream microphone, s is the spacing distance between upstream and downstream ports and k is the wavenumber. R can be extracted from this equation as follows;

$$R = |R| e^{j\phi_R} = \frac{H - e^{-jks}}{e^{jks} - H} e^{j2k(l+s)} \tag{17}$$

where, |R| is the magnitude and $\phi_R$ is the phase of the reflection coefficient. Figure 34 shows the reflection coefficient vs. frequency for open end and close end cases. For the open end case, the reflection coefficient decreases with increasing frequency. However for the close end case, the reflection coefficient is close to 1 for all frequency range as expected. At 1.1 and 3.4 kHz, there are dips in the measured reflection coefficient curve. These dips may be the result of low SNR at those frequencies because as seen from Figure 35, those points corresponds to pressure minima points.

Since the pressures at the two microphone ports are measured directly and the reflection coefficient is found for different configurations, the particle velocity can be calculated using the equations below, with the plane wave assumption.

$$U_{upstream} = \frac{P^{+}}{Z_0}(e^{jk(l+s)} - R\, e^{-jk(l+s)}) \tag{18}$$

$$U_{downstream} = \frac{P^{+}}{Z_0}(e^{jkl} - R\, e^{-jkl}) \tag{19}$$

where, $Z_0$ is the specific acoustic impedance in the tube.

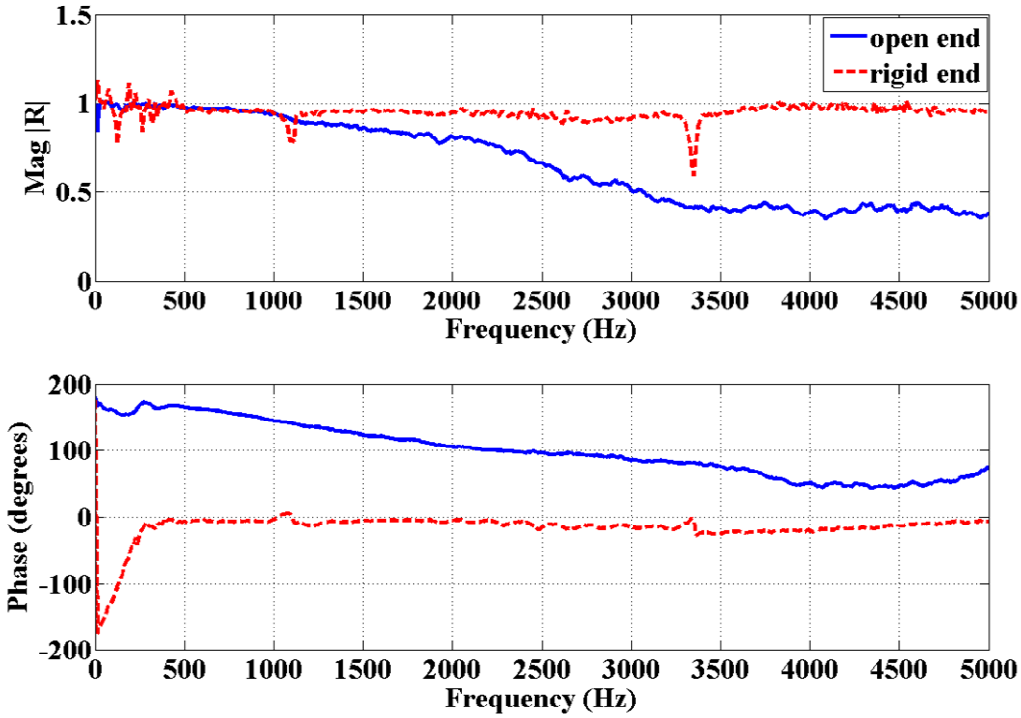


Figure 34: Magnitude (upper) and phase (lower) of the reflection coefficient vs. frequency

Measurement of the normalized pressure with LD microphone at the upstream port and the ideal normalized pressure are plotted in Figure 35. Both these plots show the normalized pressure with the rigid ended tube. Using equation 14, the normalized pressure can be written as;

$$\left|\frac{P_{upstream}}{P^{+}}\right| = \left|e^{jk(l+s)} + R\, e^{-jk(l+s)}\right| \tag{20}$$

For the measured case, *R* values are used from Figure 34 for the rigid end case. In ideal case, the reflection coefficient of the end is taken as unity which is slightly different from the measured reflection coefficient values which can be seen from Figure 34. This

difference causes the normalized pressure values to be different, especially at the low frequencies, from 100 Hz to 400 Hz.

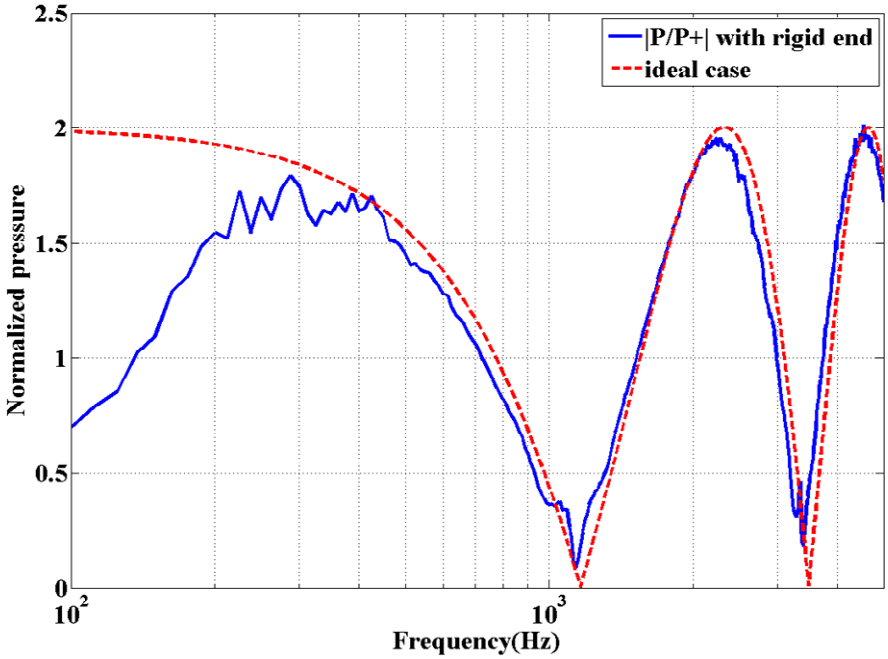


Figure 35: Measured (solid line) and ideal (dashed line) normalized pressure at the upstream microphone port of the impedance tube with rigid end

Figure 36 shows the measured and ideal normalized particle velocity at the upstream port with the rigid end. The normalized velocity can be written by using equation 18 as;

$$\left|\frac{U_{upstream} Z_0}{P^+}\right| = \left|e^{jk(l+s)} - R\, e^{-jk(l+s)}\right| \qquad \textbf{(21)}$$

Since the normalized pressure and velocity are known at any point in the impedance tube, the real values of pressure and velocity can also be obtained.

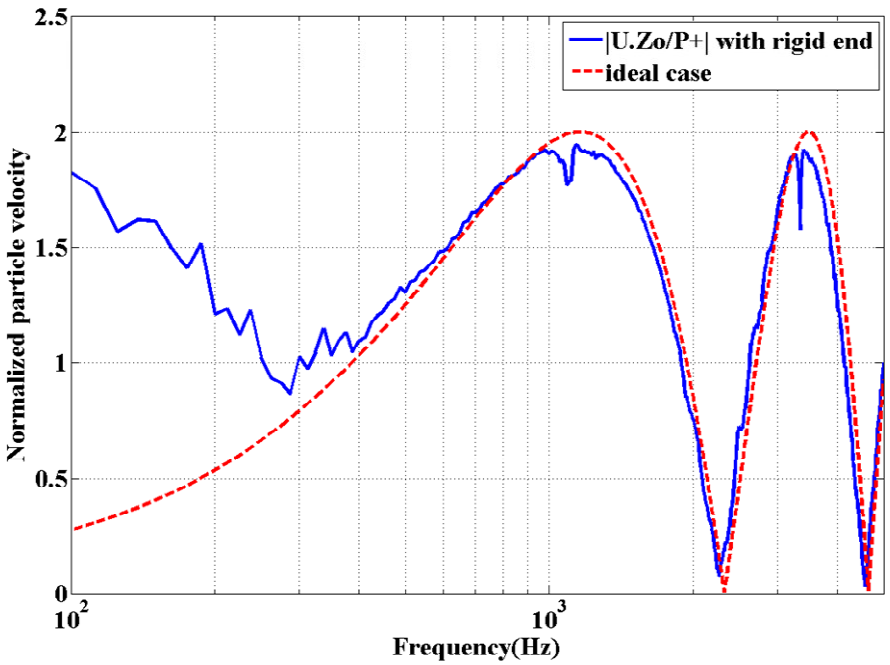


Figure 36: Measured (solid line) and ideal (dashed line) normalized particle velocity at the upstream microphone port of the impedance tube with rigid end

## Comparison of Optical Gradient Microphone with Larson Davis Calibration Microphones

After finding the particle velocity in the impedance tube, the gradient microphone is used at the same position to find if this measured particle velocity can be calculated from the measured pressure gradient of the optical gradient microphone accurately. In order to do that, the comparison of the measured velocity with the optical gradient microphone is done with the Larson Davis 2640PM 1/2" phase matched microphone pair. The result of this comparison can be found in Figure 37. The dashed curve shows the measured particle velocity using two Larson Davis phase matched microphones in the impedance tube. The solid curve shows the measured velocity with the optical gradient microphone at the same position while keeping all other parameters constant.

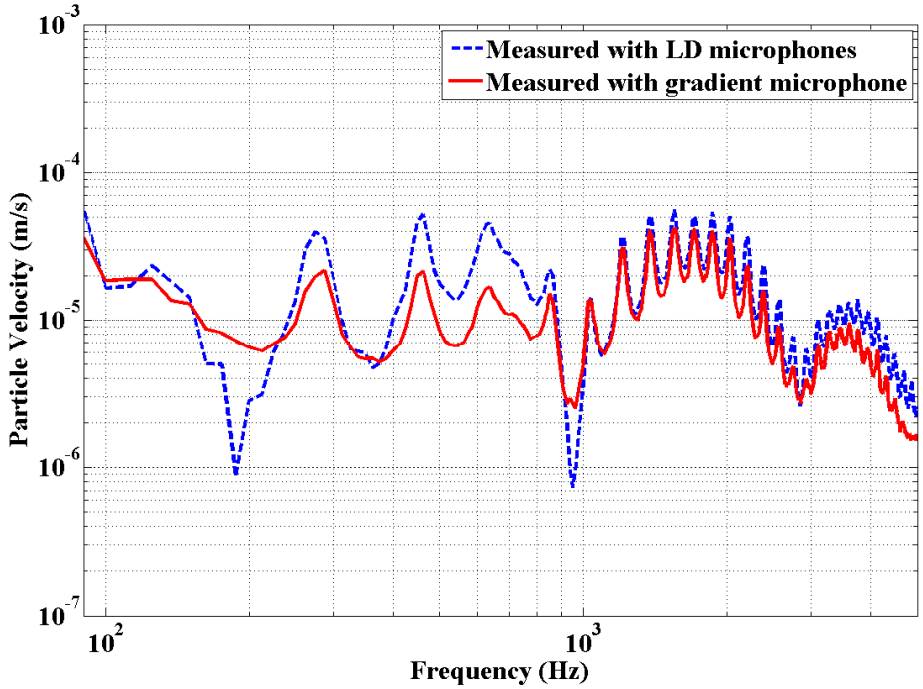


Figure 37: Comparison of measured particle velocity spectrums with optical gradient microphone and Larson Davis microphone

The useful frequency range of this comparison is between 100 Hz – 5 kHz. In this useful frequency range, the measured velocities show similar behaviors. However there is one important result of this comparison that needs to be investigated. As can be seen from Figure 37, when the measured velocity has its minima, the velocity is overestimated by the optical gradient microphone as compared to the Larson Davis microphone measurement. The reason for this is the second mode of the optical gradient microphone, which is sensitive to pressure instead of pressure gradient. The effect of this mode needs to be investigated because this will cause errors in pressure gradient measurements.

### Comparison of Optical Gradient Microphone with Particle Velocity Sensor

The second comparison of the optical pressure gradient microphone is done using a commercial particle velocity sensor, called *Microflown*. The same experimental procedure is followed by using the particle velocity sensor and the optical pressure gradient microphone in the impedance tube.

The *Microflown* is placed into the impedance tube using one of the microphone ports. The optical gradient microphone is placed to the other microphone port. While the speaker is driven by a broadband signal, the particle velocity is measured by optical gradient microphone and the particle velocity sensor at the same time. The ports of the velocity sensor and the optical gradient microphone are then swapped and the same measurement is performed again while keeping all other parameters as well as the speaker signal constant. The comparison of the two measured velocities at the same position using two different sensors is shown in Figure 38. The dashed curve shows the measured particle velocity in the impedance tube by using the *Microflown* velocity sensor. While placing this sensor, the sensitive direction of the sensor is aligned with the longitudinal axis of the impedance tube. The minimum velocity points in this measurement come from the standing wave phenomena. These points depend on the dimensions of the tube and match with the expected values.

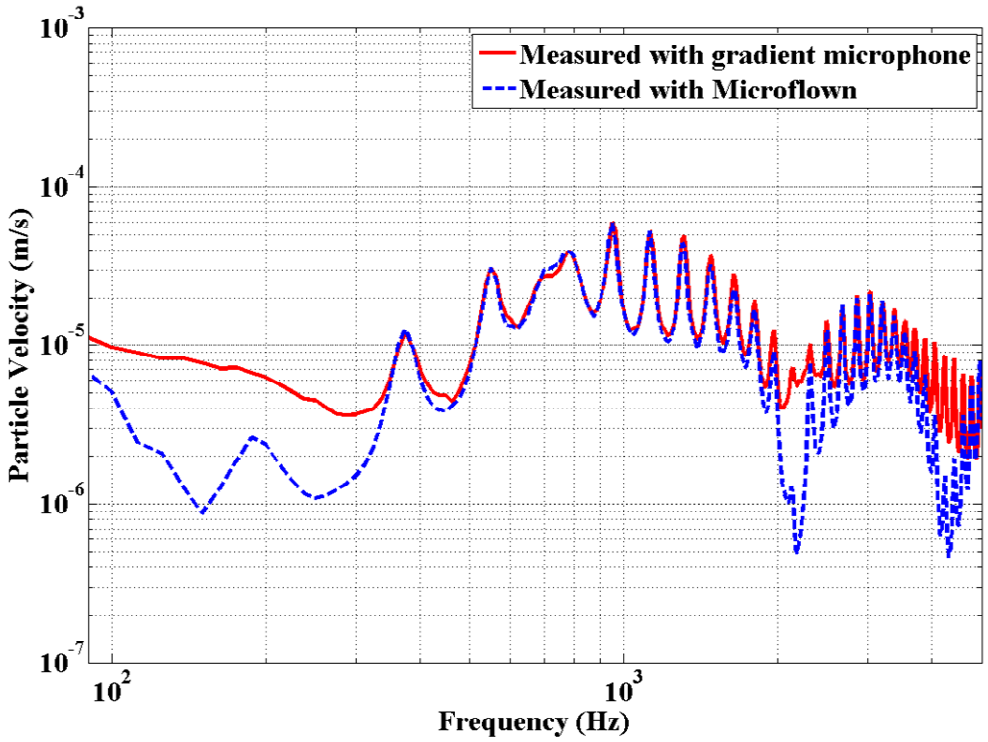


Figure 38: Comparison of measured particle velocity spectrums with optical gradient microphone and Microflown particle velocity sensor

The solid curve shows the measured velocity with the optical gradient microphone at the same position. These two curves show similar behavior except at certain frequencies. While the locations of minimum velocity points match in these two measurements, the amplitudes of those minima are different. As seen from the figure, the gradient microphone measurements overestimate the velocity value at the minimum velocity points. Also at lower frequencies, there is a difference between the measured particle velocities. The reason is the second mode effect of the gradient microphone on the pressure gradient measurement. This effect is investigated in detail and will be described in the modeling section.

**Pressure Residual Intensity Index Measurements**

For sound intensity measurements that use PP-method, the accuracy is strongly dependent on the phase and amplitude matching between the two measurement channels. Even the same signal is applied to both measurement channels; measured intensity is not usually zero. The intensity caused by the phase and amplitude mismatch between the microphones including the processing unit is known as the residual intensity. In order to measure the mismatch between two measurement channels, the residual intensity calibrator, shown in Figure 39, can be used.


Figure 39: Larson Davis residual intensity calibrator

Residual intensity calibrator applies the same signal with zero phase difference to two channels in which two microphones are plugged. As an external noise source, usually a pink or white broadband noise is used. Measured residual intensity amplitude depends on the amplitude of the applied pressure. However, the difference between the sound pressure level and the residual intensity level is not dependant on the applied sound level. This difference between the pressure level and the residual intensity when the intensity probe is placed in a sound field in such an orientation that the particle velocity in the direction of the probe measurement axis is zero is called pressure residual intensity index (PRII) [30]. In sound intensity measurements, for a specific spacer distance, the pressure

residual intensity index should ideally be as large as possible. For a constant pressure input, larger residual intensity index corresponds to lower residual intensity which means lower error in intensity measurement that comes from the mismatch of the two measurement channels.

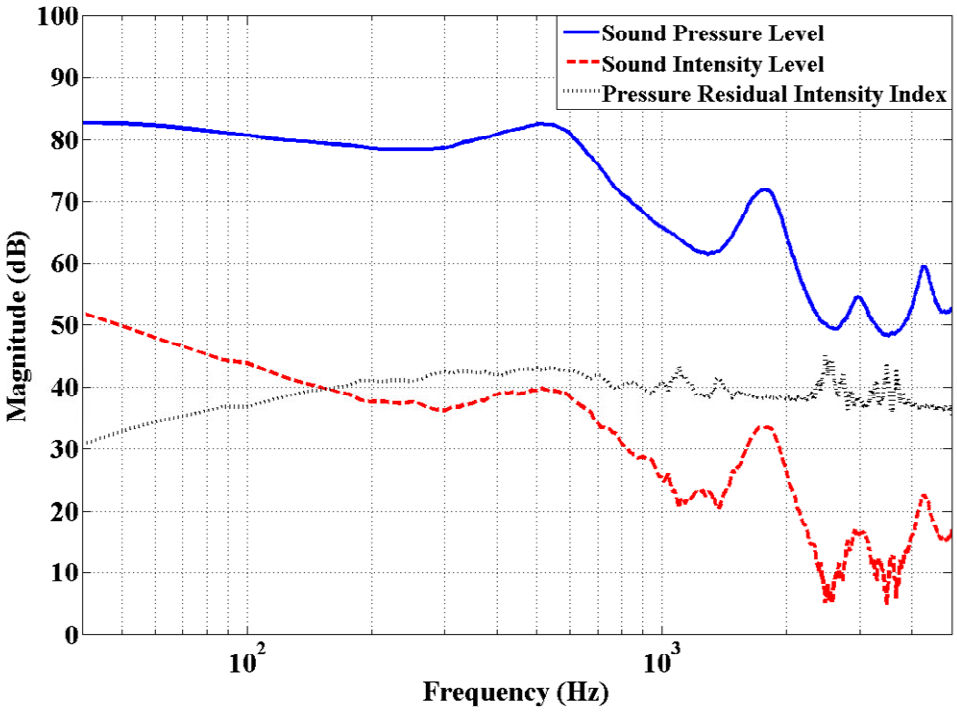


Figure 40: Pressure Residual Intensity Index calculated from measured sound pressure and intensity level of LD 2260 probe with phase matched microphones

Figure 40 shows the measured pressure residual intensity index of the LD Model 2260 PP-probe with two phase matched microphones. It is shown in the graph that, even if the same pressure signal is applied to the both channels of sound intensity probe; the measured intensity is not zero. At low frequencies, the measured residual intensity, shown with the dashed curve, is larger, which is expected since the phase mismatch of the microphones becomes more significant at low frequencies. The PRII that is calculated

from the measured pressure level and intensity level decreases at the low frequencies because of high residual intensity as shown in the dotted curve. The residual intensity measured is the lower limit below which the intensities can not be measured accurately. In the whole measurement frequency range, the PRII of the Larson Davis probe is greater than 30 dB.

With the same approach, PRII of the gradient microphone is measured. In order to use this residual intensity calibrator with the gradient microphone, some adjustments are needed. The optical gradient microphone is placed to one port of the calibrator as seen from Figure 41. Applying the same signal to two pressure microphones is similar to applying the same signal to both sides of the gradient microphone diaphragm. This can be achieved by applying the same sound field directly on to the diaphragm. In the ideal case, since the pressure on both sides of the differential diaphragm is equal, the measured pressure gradient should be zero. However, as in the case of phase mismatch with pressure microphones, any mismatch in the diaphragm and the processing unit results in a pressure gradient which is an error to be corrected.

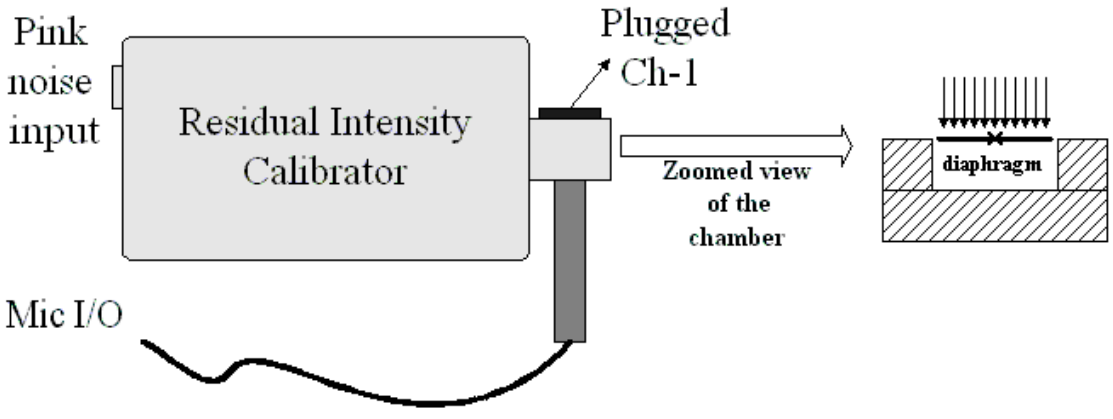


Figure 41: Schematic of the test-up to measure the residual intensity index of the differential microphone

Figure 42 shows the measured pressure and the intensity level in addition to the pressure residual intensity index with the gradient microphone. As can be seen from the dashed curve, even the pressure applied directly and equally on each side of the gradient microphone diaphragm, the measured intensity level is not zero. This dashed curve shows the minimum limit below which the sound intensity can not be measured accurately with this gradient microphone. The difference between the applied pressure level and the measured intensity level is plotted with the dotted curve. This dotted curve has higher values when the gradient microphone response is dominated by the first mode shape which is sensitive to the pressure gradient. When the gradient microphone response is affected by the second mode shape which is sensitive to the pressure, the measured intensity values at those frequencies have errors.

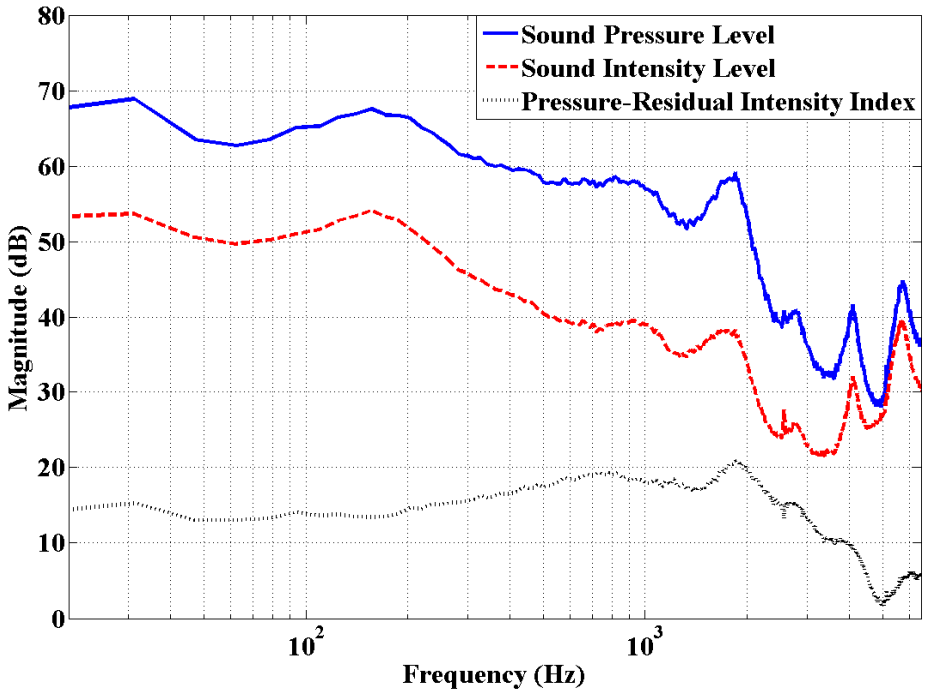


Figure 42: Pressure Residual Intensity Index of gradient microphone in combination with pressure microphone

The PRII measured with the gradient microphone is compared with the IEC 1043 standard requirements [62, 63]. Since the standards are given for the standard PP-probes with spacers, the gradient microphone is compared with these standards even it doesn't use any spacer. These standard curves set the lowest limit of the allowable PRII for an instrument measuring the sound intensity. The comparison of pressure residual intensity indexes for the gradient microphone and IEC 1043 requirements are plotted in Figure 43. Ideally, the PRII of the gradient microphone should be as high as possible. The gradient microphone with 1mm port spacing meets the IEC Class 1 requirements with 12mm spacing until 2.5 kHz. After 2.5 kHz the pressure residual intensity index shows a gradual decrease. As described earlier, after 3-4 kHz, the gradient microphone starts to respond pressure because of the in-phase mode motion, which increases the measured residual intensity and decreases the PRII.

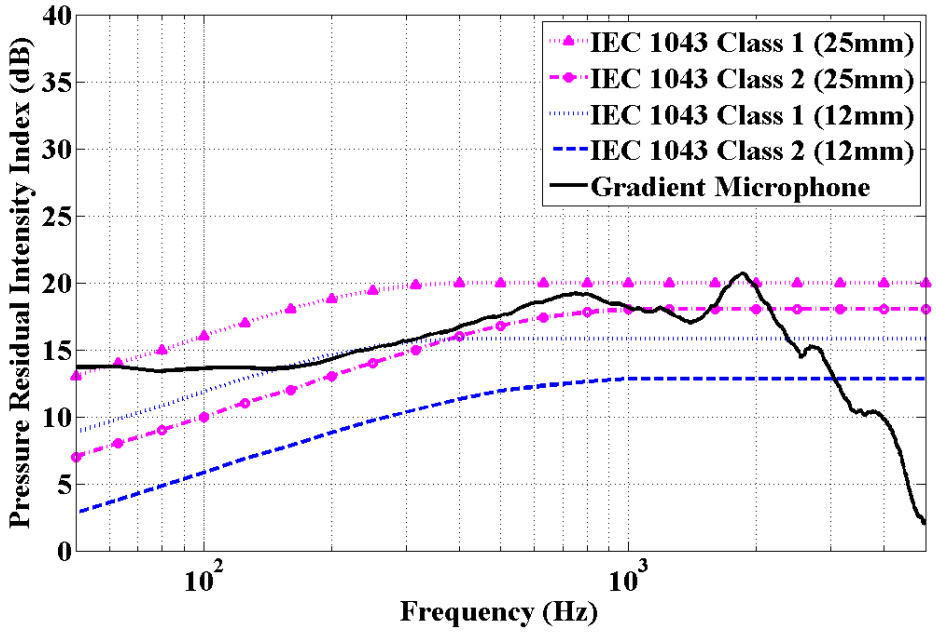


Figure 43: Comparison of measured pressure residual intensity index of gradient microphone with IEC 1043 requirements

## Sound Power Measurements

Sound power is the energy of the sound source per time and the sound power measurement methods of noise sources are well established with existing measurement standards [64]. Measuring sound intensity accurately is the key point in sound power measurements. Therefore, sound power measurements can be used as an indication of the optical gradient microphone's sound intensity measurement capability.

The schematic of the experimental set up that is used to measure the sound power level of a reference sound source is shown in Figure 44. A hemispherical surface is used as the closed surface to measure the sound pressure or the sound intensity around the sound source. Given the geometrical parameters of this surface, and the pressure or sound intensity values measured on the surface, sound power level of the source can be calculated.

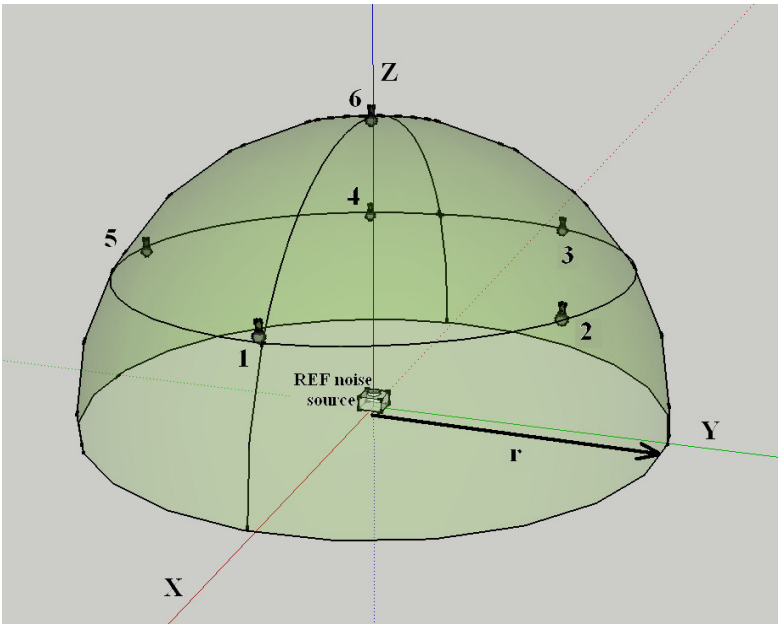


Figure 44: Experimental setup for measuring sound power with six-point hemispherical measurement surface

The microphone positions on the hemispherical surface are shown by numbers. There are a total of six different measurement points in this setup. All the sound power measurements using this set up are done in the hemi-anechoic chamber. A Larson Davis REF 600 reference sound source which has well known power output specifications is placed at the center of this hemispherical measurement surface [65]. All the measurement points on the surfaces have the same radial distances from the source. In the first part of the experiment, Larson Davis Model 2541 microphones which are facing towards the sound source are used to measure the sound pressure at those six different measurement points. The same experiment is performed by using the optical gradient microphone with a pressure microphone and measuring the sound intensity on that hemispherical surface. Figure 45 shows pictures of the experimental setup in the hemi-anechoic chamber. In Figure 45a, LD microphone which is placed at measurement location 6 is shown. The reference sound source is placed directly under this measurement location. In Figure 45b, the optical gradient microphone is shown as placed at the same measurement location. The important point about this measurement is the placement of the gradient microphone. Since the optical microphone is directional and sensitive to the pressure gradient in one direction, the sensitive direction is aligned with the reference sound source. However, while placing the LD microphone, it is made sure that the microphone faces towards to the sound source. From these experiments, the sound power level of the reference noise source is calculated by using the measured pressure and pressure gradient values by using the LD microphone and the optical gradient microphone respectively.

a) b)

Figure 45: Sound power measurement setup in the hemi-reverberant chamber with a) Larson Davis microphone, b) optical gradient microphone at location 6.

Before using the Larson Davis microphone, it is calibrated with a piston-phone calibrator to find its sensitivity. The sensitivity of the LD microphone is constant over the frequency range of the measurements. However, this is not the case for the optical gradient microphone. Initially the optical gradient microphone is calibrated using a reference microphone in the anechoic chamber. The sensitivity curve as a function of frequency is found. Then this sensitivity is used for converting the measured pressure gradient measurements into the particle velocity. For calculating the sound power level from the measured sound pressure values, the following equation is used [66];

$$L_w - L_p = 10\log_{10}(\frac{4\pi r^2}{Q}) - 10.5 \quad \textbf{(22)}$$

where $L_w$ and $L_p$ is the sound power and pressure level respectively, r is the radius of the measurement surface and $Q$ is the directivity factor. Since all the experiments are done in the hemi-anechoic chamber, the directivity factor is taken to be 2 ($Q=2$) for calculations. It represents the configuration of placing the sound source on a rigid surface when all the other walls act like a free field. This directivity factor determines the sound wave radiation pattern. Figure 46 shows the comparison of the A-weighted 1/3 octave band sound power level of the reference noise source.

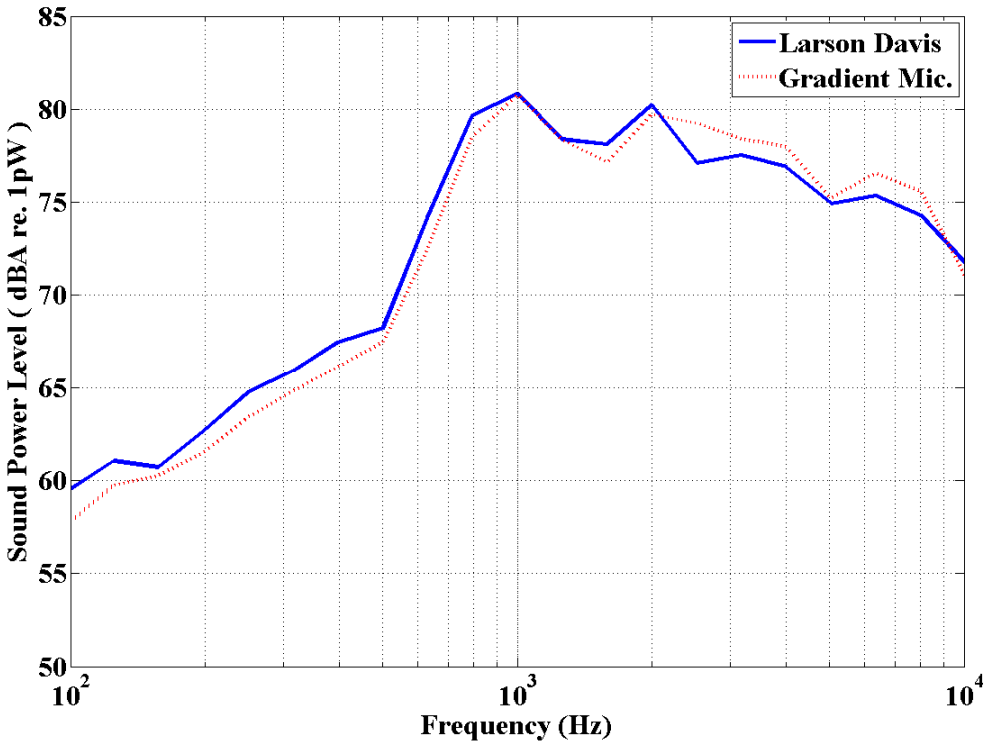


Figure 46: Comparison of the measured 1/3 octave band Sound Power Level of the reference sound source in the semi-anechoic chamber

The figure shows that the measured sound power levels show the same behavior over the whole frequency range. Between 500 Hz- 1.5 kHz at which the gradient

microphone is highly sensitive in measuring the gradient, the difference between the sound power measurements is minimal. When the overall A-weighted sound power level is calculated, it is found that the measured power levels are 88.7 and 89.0 dBA with LD microphone and optical gradient microphone respectively. These numbers match well with the specifications of the REF 600 reference noise source which has 88.8 dBA sound power level in the frequency range of 50 Hz- 10 kHz.

Characterization of these gradient microphones in terms of particle velocity measurement capability shows that these microphones have non-ideal response to pressure gradient. As predicted in Chapter 2, the second mode effect causes errors in particle velocity measurements. Impedance tube characterization shows that the gradient microphone has problems in measuring particle velocity at velocity minima. To quantify this problem, PRII is the real metric that needs to be considered. PRII characterization shows that above 3 kHz, the measured PRII has a gradual decrease and the values are lower than the minimum limits set by standards. As mentioned in Chapter 2, these errors come from the unwanted mode shape of the diaphragm which responds to pressure instead of pressure gradient. In order to investigate this issue, an equivalent circuit model is developed which predicts the separate responses of the diaphragm mode shapes and the overall response of the gradient microphone. Modeling chapter will describe the results of the different mode shape responses and the effect of these mode shapes on intensity measurements and options to suppress the unwanted mode shapes in order to get optimized pressure gradient measurements.

# CHAPTER 4

# EQUIVALENT CIRCUIT MODELING

Equivalent circuit models, which allow circuit analysis techniques to be used to link the electrical, mechanical and acoustic domains, have been used to predict the frequency response, sensitivity and noise performance of electro-acoustic devices since their inception [67, 68]. These models have also been helpful in the analysis of micromachined microphones [1, 69]. In many cases, the equivalent circuit models provide an analytical description of the mechanical behavior of the microphone diaphragm as a combination of lumped circuit elements obtained from the duality principle. In some cases, especially for devices such as considered here, complicated mechanical structures with multiple vibration modes and complex interactions with surrounding air, finite element modeling tool must be used to fully characterize and model the device [70-72].

The electrical output in response to the acoustic input pressure is usually the main quantity of interest, and it is obtained through an electromechanical transformer [68, 73]. In the device considered here, where the readout is optical, the coupling of the electrical signals to the mechanical domain is especially important, since this provides the means to affect the mechanical behavior of the microphone diaphragm through the application of force feedback signals.

In the following, a small signal electromechanical equivalent circuit model for the biomimetic microphone with optical readout and electrostatic actuation is developed and described. To determine the lumped circuit elements in the mechanical domain finite

element (FEM) based structural and fluid modeling tools ANSYS (ANSYS v11.0, ANSYS Inc., Canonsburg, PA) and FLOTRAN are used, respectively. The calculations of the equivalent circuit modeling results are performed in MATLAB.

## Equivalent Circuit Model of Biomimetic Microphone

The basic schematic of the biomimetic diaphragm integrated with optical detection method can be seen in Figure 47. The diaphragm, which pivots about hinges at the center, can be actuated by three external sources. The first is the incoming sound wave at an angle $\phi$ to the diaphragm normal, denoted by $P_{acoustic}$. The others are the electrostatic actuation signals, which can be applied between the rigid reflective backplate connected to the substrate and to the end of the diaphragm on each side. This electrostatic actuation signal, $V_e$, can be used for both biasing the diaphragm to the most sensitive point of the optical detection method and applying the force feedback signal [52]. The displacement in response to these actuation signals can be measured at either end of the diaphragm by the optical detection method (in Figure 47, optical readout is from the left end). Other important parameters that determine the diaphragm response are the air flow in and out of the backside cavity and the air filled volume of the backside cavity.

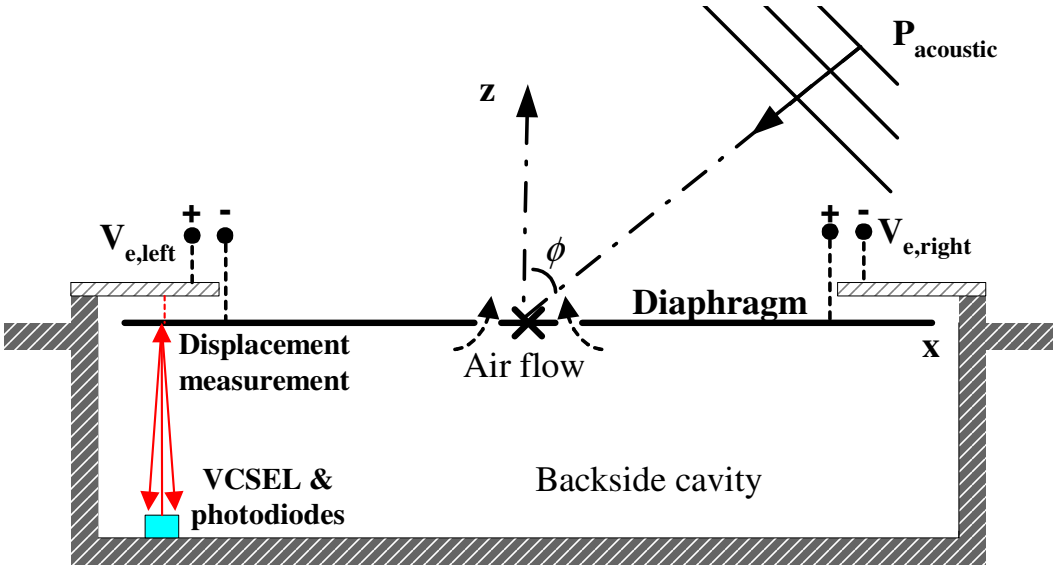


Figure 47: Basic schematic of the biomimetic microphone with electrostatic actuation ports and the integrated optical detection (left readout).

In addition to the rotation of the diaphragm, which is represented by a rocking mode around the pivot, referred as the first mode, the biomimetic directional diaphragm also has a second mode in the audio frequency range. This in-phase mode corresponds to the flapping motion of the diaphragm in response to the spatial average of the difference in the pressure between the front and back side of the diaphragm. In order to understand and predict the overall response of the directional microphone, the effects of both of these modes need to be accounted for. Because the mode shapes of these two modes are substantially different, their responses result in different restoring forces created by the compression and viscosity of the air in the backside cavity. Taking all these external and internal factors into account, a small signal linear equivalent circuit model for predicting the overall response of this directional microphone can be drawn as shown in Figure 48. This equivalent circuit model uses only the first and the second modes to predict the

overall microphone response in audio frequency range. This assumption is verified later in this chapter by showing the effect of the higher order modes on the overall response.

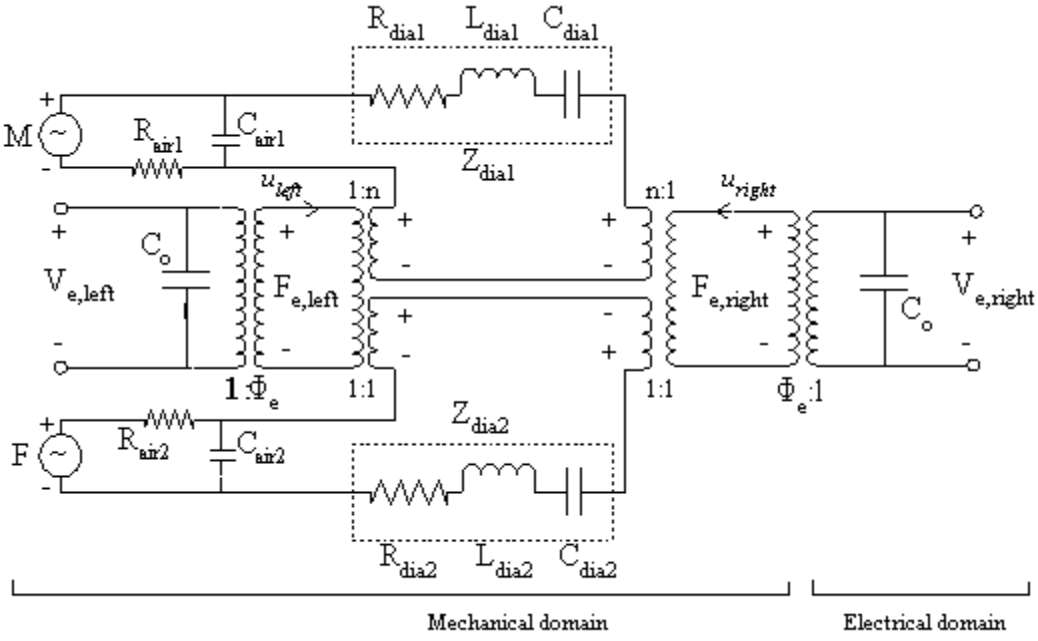


Figure 48: Equivalent circuit model of the directional microphone accounting for two resonant modes in the audible frequency range. Two acoustic and two electrostatic ports are used as inputs. The response of the diaphragm is measured from left or right side with an optical detection method.

In this circuit representation, inputs are the moment and force generated by the acoustic signal applied by the incoming pressure wave and the electrostatic forces which are applied to electrodes located on both sides of the diaphragm. If the incoming acoustic wave is taken as a plane wave, then the pressure on the diaphragm can be expressed as;

$$P(x,t) = P_0 e^{i\omega(t-\frac{x}{c}\cos(\varphi))} \quad \textbf{(23)}$$

where $P_0$ is the amplitude of the acoustic pressure, ω is the angular frequency, t is time, x is the distance measured from the centre of the diaphragm in the length $L$ direction, $c$ is the speed of sound, and $\phi$ is the angle of an incoming plane sound wave relative to the plane of the diaphragm.

The moment, M, applied by the acoustic input about the axis of rotation of the rectangular diaphragm can be written as [18],

$$M = \frac{P_0 I_A \omega \cos(\phi)}{c} \tag{24}$$

where $I_A$ is the area moment of inertia of the rectangular diaphragm with width $b$ and length $L$ about the axis of rotation ($I_A = bL^3/12$). In addition to the moment which is caused by the pressure gradient, the average pressure on the diaphragm results in force which drives the second mode resonance of the diaphragm. The force that drives the second mode can be written as,

$$F = P_0 A \cos\left(\frac{kL}{2}\sin(\phi)\right) \tag{25}$$

where $A$ is the area of the diaphragm and $k$ is the wavenumber. The dependence of the second mode response on the incoming sound wave angle is determined by $kL/2 = \pi L/\lambda$. Since $L << \lambda$ the cos(.) term is nearly unity, causing the response of the second mode to be independent of the angle of incidence of the incoming sound wave.

In addition to the acoustic inputs, $M$ and $F$ shown in Figure 48, two electrostatic inputs, $V_{e,left}$ and $V_{e,right}$, are used to actuate the diaphragm. In order to model the conversion between the electrical and mechanical domain, a transformer is used. The transformer ratio can be found from the small signal approximation of the parallel plate solution [74].

$$\Phi_e = \frac{\varepsilon_o A_{electrode} V_{DC}}{2g^2} \quad \left( \frac{force, N}{voltage, V} \right) \tag{26}$$

where $\varepsilon_o$ is the permittivity of free space, $A_{electrode}$ is the area of actuation electrodes, $V_{DC}$ is the applied DC voltage and $g$ is the gap between the grating plane and the reflector plane. After finding the electrostatic forces from each side, $F_{e,left}$ and $F_{e,right}$, these forces are divided between the two modes by another transformer with multiple secondary windings. For the first mode, the transformer's ratio $n$ is used to convert this electrostatic force into the moment that drives the first mode shape. The ratio $n$ is found to be $L/2$ which is the length of the moment arm (distance between the pivot points to the end of the diaphragm). For the second mode, the electrostatic force is directly used, since this mode is driven by a force instead of a moment.

Table 3: Parameters of the equivalent circuit model and corresponding analysis tool to extract them.

| | |
|---|---|
| $R_{dia1}$ | *Measurement in Vacuum* |
| $C_{dia1}$ | *FEM Structural Analysis* |
| $L_{dia1}$ | *FEM Structural Analysis* |
| $R_{dia2}$ | *Measurement in Vacuum* |
| $C_{dia2}$ | *FEM Structural Analysis* |
| $L_{dia2}$ | *FEM Structural Analysis* |
| $C_{air1}$ | *FLOTRAN CFD Analysis* |
| $R_{air1}$ | *FLOTRAN CFD Analysis* |
| $C_{air2}$ | *FLOTRAN CFD Analysis* |
| $R_{air2}$ | *FLOTRAN CFD Analysis* |

All the equivalent circuit parameters used in the equivalent circuit model are listed in Table 3. In order to find these parameters, different analysis tools are used. The diaphragm mode shapes are modeled as R-C-L circuit. $R_{dia}$ for the first and the second

mode are found from the measurements in vacuum. $C_{dia}$ and $L_{dia}$ terms for each mode are found from finite element structural analysis. $Z_{dia1}$ and $Z_{dia2}$ are calculated mechanical impedances of the diaphragm in the 1st mode with units of *Nm/(rad/s)* and the 2nd mode with units of *N/(m/s)* respectively. Using the transfer functions given in Equations 8 and 9, $Z_{dia1}$ and $Z_{dia2}$ can be found with units of *N.m/(rad/s)*and *N/ (m/s)* respectively.

$$Z_{dia1} = \frac{I_A}{H_{pt} c} \tag{27}$$

$$Z_{dia2} = \frac{bL}{H_{px} \omega} \tag{28}$$

To model the influence of the air on the diaphragm response, two different impedance terms are extracted from a FLOTRAN analysis. This analysis solves the simplified Navier-Stokes equations for the fluid domain underneath the microphone diaphragm. The other important detail of this analysis is the fact that the displacement profile of the diaphragm is obtained from the FEM structural analysis and coupled into the FLOTRAN analysis as an input. The first impedance, $Z_{air1}$, is defined as the ratio of the moment on the diaphragm to the rotational velocity. The second impedance, $Z_{air2}$, is defined as the ratio of the average pressure on the diaphragm to the translational (in-phase) velocity extracted from the structural analysis. In this FLOTRAN analysis, the diaphragm is considered as rigid, which results in the series connection of $R_{air}$ and $C_{air}$ parameters in the equivalent circuit model shown in Figure 48. Using this information, $R_{air}$ and $C_{air}$ terms in the equivalent circuit can be written as;

$$R_{air} = \mathrm{Re}(Z_{air}) \tag{29}$$

$$1/(i\omega C_{air}) = \mathrm{Im}(Z_{air}) \tag{30}$$

where Re(.) and Im(.) are real and imaginary parts of the impedance respectively.

As mentioned earlier, the acoustic radiation impedances of the microphone diaphragm for both mode shapes are ignored in the equivalent circuit model, which needs to be verified. The radiation impedance of the in-phase mode can be roughly estimated from the radiation impedance calculation of a rectangular piston [75]. This radiation impedance can be written as;

$$Z_{radiation} = \rho cA\left[R(kL) + jX(kL)\right] \tag{31}$$

where A is the area of the diaphragm with length $L$, $kL$ is a normalized wave number, $R(kL)$ and $X(kL)$ are normalized radiation resistance and reactance coefficients of the rectangular diaphragm. For the audio frequency range (20-20000 Hz), $R$ and $X$ can be expressed as follows;

$$R_{inphase} \cong (kL)^2 (1/2\pi r) \tag{32}$$

$$\begin{aligned} X_{inphase} \cong kL\Big\{&(1/3\pi r)\left[1 + r^3 - (r^2+1)^{3/2}\right] + (1/\pi)\cosh^{-1}(\left[r^2+1\right]^{1/2})... \\ &... + (r/\pi)\cosh^{-1}(\left[r^2+1\right]^{1/2}/r)\Big\} \end{aligned} \tag{33}$$

where $r$ is the aspect ratio of the rectangular diaphragm. For comparison these real and imaginary parts of the radiation impedances of the 2nd mode shape are plotted in the audio frequency range as shown in Figure 49. The radiation impedance for the second mode is at least 5 orders of magnitude smaller than the impedance of the air for the same mode shape ($|Z_{air2}|$). Therefore the radiation impedance of the second mode shape is ignored in the equivalent circuit model for the simplicity.

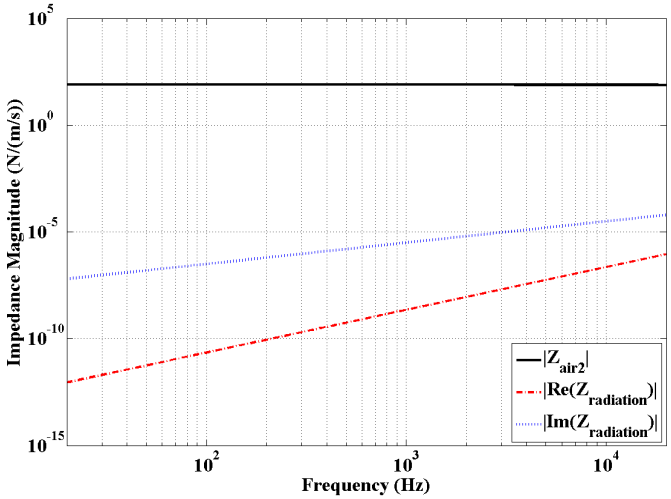


Figure 49: Comparison of the air impedance with the calculated acoustic radiation impedance terms for the 2nd (in-phase) mode.

The radiation impedance of the first (rocking) mode can be found by using the out of phase velocity distribution as an input and the moment resulting from the generated pressure. This gives us the impedance with the correct units in the mechanical loop for the out-of-phase mode. The derivation of the radiation impedance of the rocking mode is shown earlier [76]. For the audio frequency range where kL<<1, the radiation efficiency of the rocking mode of a rectangular diaphragm can be written as;

$$\sigma_{outofphase} \cong \left(\frac{1}{72\pi r}\right)(kL)^4 \tag{34}$$

As can be seen from equations 32 and 34, the radiation efficiency of the in-phase and out-of phase modes are proportional to $kL^2$ and $kL^4$ respectively. From this comparison, it can be concluded that the first mode for small $kL$ is much less efficient in radiating sound than the second (in-phase) mode. Since the second mode radiation impedance is ignored and the first mode is less efficient than the second mode, the

radiation impedance of the first mode can also be ignored safely in the equivalent circuit model.

Furthermore, one needs to consider the polarity of the transformers for each mode in the equivalent circuit model. If the same electrostatic signal is applied from both sides of the diaphragm, the resulting forces should be added when driving the second (in-phase) mode. However, if out of phase electrostatic signals are applied, the resulting forces should be added for the first mode, while cancelling each other for the second mode. These requirements are met by adjusting the polarity of the transformers as shown in Figure 48. Note that this mode-selective actuation capability can be used to suppress undesired modes without changing the design of the diaphragm.

Finally, out-of-plane displacements at each end of the diaphragm, resulting from the velocity signals, $u_{left}$ and $u_{right}$ in the equivalent circuit, can be sensed by the integrated optical interferometer.

## Determination of Equivalent Circuit Elements

Several analysis tools are required for finding the individual parameters shown in the equivalent circuit model shown in Figure 50. The parameters of the diaphragm and the air are extracted from finite element models based on the ANSYS structural and FLOTRAN packages respectively. In addition to these analyses, measurements in vacuum are performed to find the structural damping of the microphones. After that, the effects of all of these parameters are combined by using the equivalent circuit model. The process flow of this combined model is shown in Figure 50.

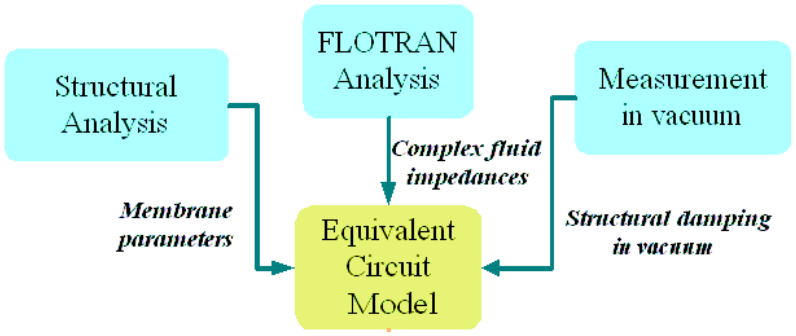


Figure 50: Process flow of the combined model

**Measurements in Vacuum**

As mentioned earlier, $R_{dia}$ terms for each mode are found from the measurement in the vacuum. The microphone is placed into a vacuum chamber and the response is measured in order to isolate the structural damping from the damping due to air flow and sound radiation. The schematic and the picture of the vacuum chamber setup used for these experiments can be seen from Figure 51.

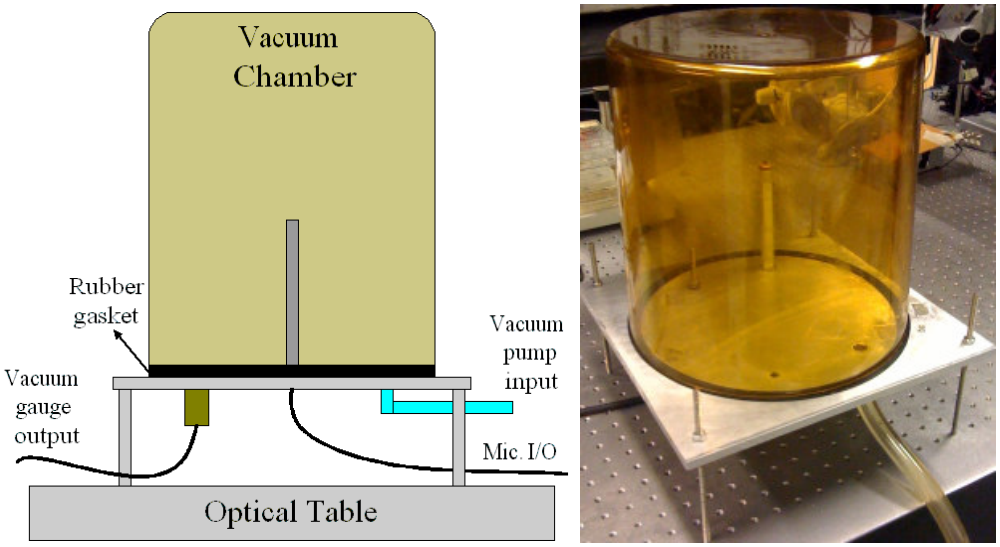


Figure 51: Schematic (left) and the picture (right) of the vacuum test set-up

Since electrostatic actuation does not require a propagation medium, it is used to actuate the diaphragm in vacuum to obtain the frequency response. The frequency response resulting from electrostatic actuation is measured with integrated optical detection while the diaphragm is driven by a broadband signal from one electrode located on the side of the diaphragm. Even the diaphragm is actuated from one side; one-sided electrostatic actuation excites both mode shapes because the excitation signal has both odd and even part to drive the first and the second mode respectively. The results of these measurements at different vacuum levels can be seen in Figure 52. As seen from the 30 Torr data in Figure 52, two distinct resonances are clearly detected. This data is used to fit the structural damping parameter of each mode.

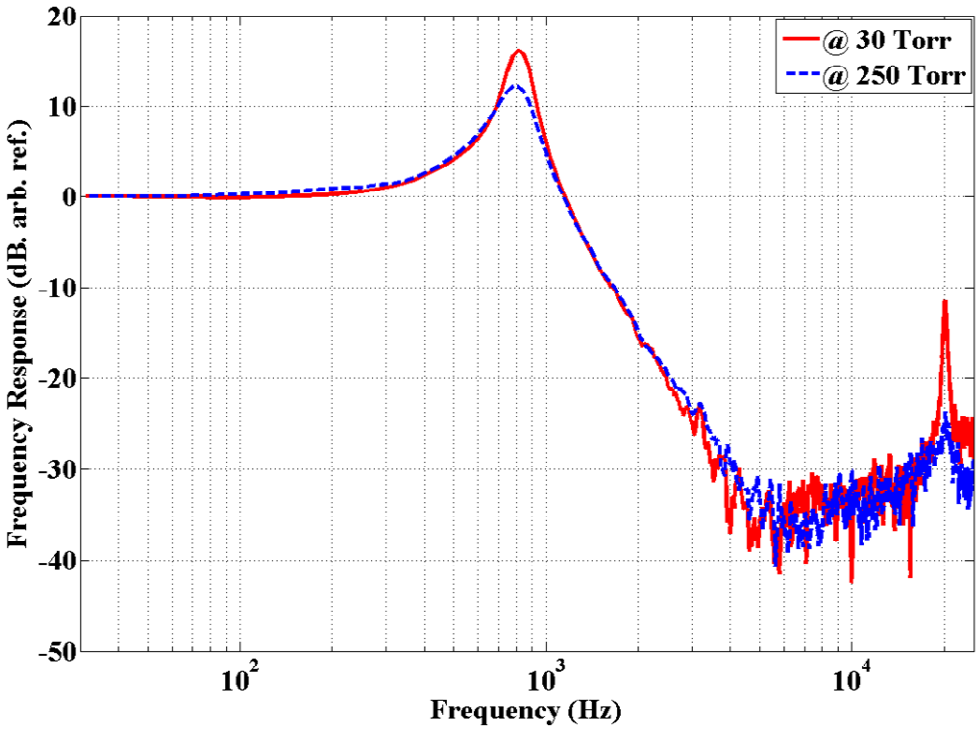


Figure 52: Measured and normalized electrostatic frequency response of the differential microphone with different vacuum pressures.

As expected, the quality factor of the first mode, which is a measure of the sharpness of the resonance, is less affected by evacuating the chamber. The quality factor is increased by 1.5 times going from atmospheric pressure to 30 Torr. In contrast, the in-phase mode is significantly affected, and the quality factor increases by more than 10 times. It can be concluded that the air loss is more significant in the second mode because of the in-phase movement causing the air under the diaphragm to get squeezed. This is further verified through computational fluid dynamics analysis later in this chapter.

To show the effect of the air damping on different modes, the change of the quality factors is plotted in Figure 53. When the pressure changes from 30 Torr to 250 Torr, which corresponds to a change from 96% to 65% vacuum respectively, the quality factor of the first and second mode of the differential microphone is reduced by ~47 % and ~89 % respectively, showing the effect of air in the second mode motion.

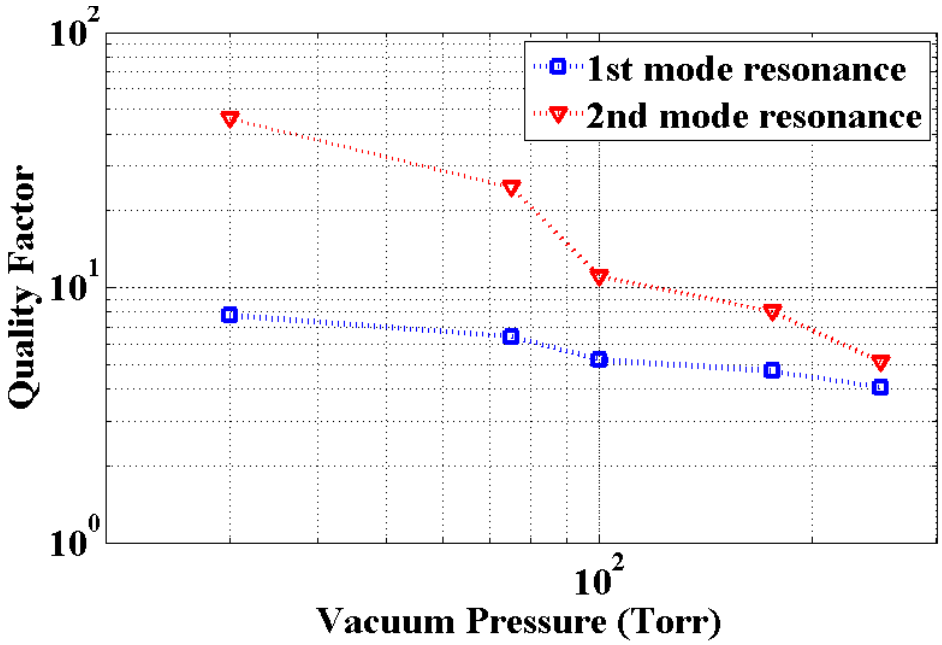


Figure 53: The change of the quality factor of two resonance modes with changing vacuum levels between 30-250 Torr

**Structural Analysis**

The model of the microphone diaphragm that is shown in Figure 54 is used for the structural analysis.

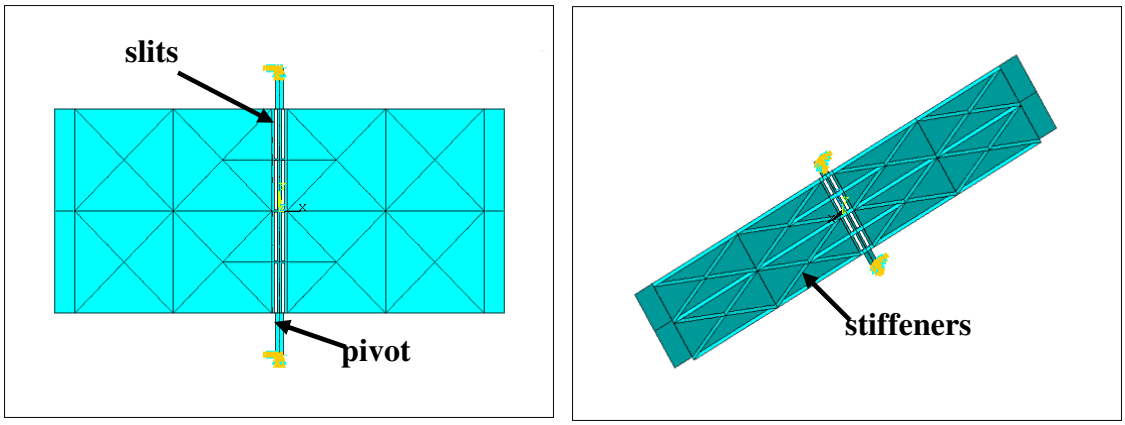


Figure 54: Top view (left) of the differential diaphragm model and the angled view (right) to show the stiffeners on the diaphragm

Finite element modal analysis is used to extract the resonance frequencies of the modes and diaphragm parameters like stiffness and the equivalent masses to find mechanical impedances. After creating the model and setting all the material properties, boundary conditions are applied. The first and second mode shapes can be seen in Figure 55. The first mode shape consists of a rocking motion in which two sides of the diaphragm rotate about the central pivot in opposite directions. The resonance frequency of this mode is around 800 Hz. The second mode shape of the diaphragm is shown on the bottom of Figure 55. In this mode, each side of the diaphragm moves in the same direction, which results in in-phase movement. The resonance frequency of this mode is around 14 kHz.

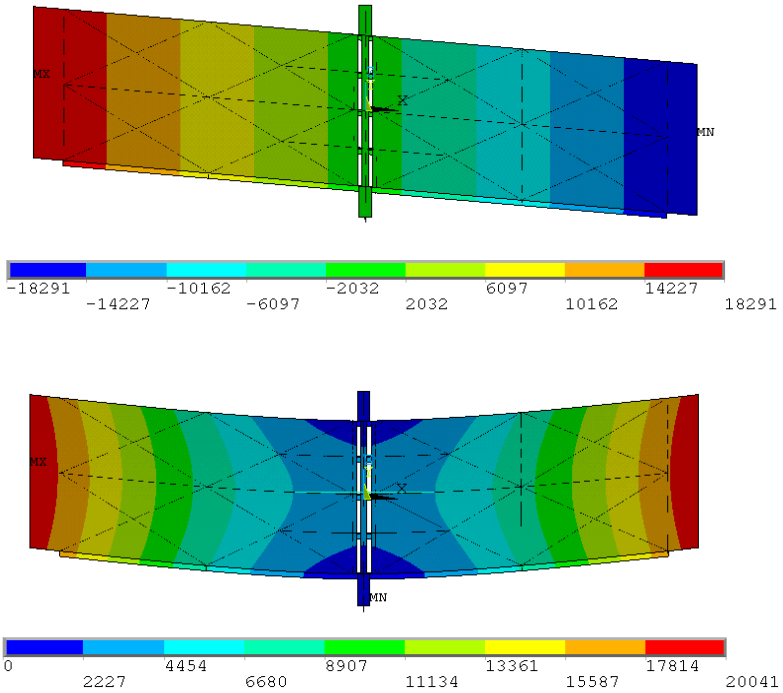


Figure 55: 1st out of phase mode shape (top) and 2nd in-phase mode shape (bottom) of the gradient microphone diaphragm

In addition to the mode shapes and resonance frequencies that are extracted from the structural analysis, effective mass and mass moment of inertia of different modes are also found. Effective mass of the 2nd mode, $m_{eq}$, and the mass moment of inertia of the 1st mode, $I_{yy}$, are found to be $4\text{x}10^{-8}$ *kg* and $5\text{x}10^{-15}$ *kg* $m^2$ respectively. These values are used in equations 27 and 28 to calculate the mechanical impedances of the diaphragm modes, $Z_{dia1}$ and $Z_{dia2}$.

**Computational Fluid Dynamics Analysis**

In the structural analysis that is described above, viscous loss or any effect of air is not taken into consideration. However, the dominant loss mechanism in microelectromechanical system (MEMS) devices is air damping. In order to take this into account, FLOTRAN computational fluid dynamics (CFD) analysis is performed [77]. Before performing the analysis with the directional microphone, the FLOTRAN model is verified by using a well known Helmholtz resonator model. The results are compared with theoretical results and the model is found to be accurate. The details of this Helmholtz resonator model are explained in Appendix A.

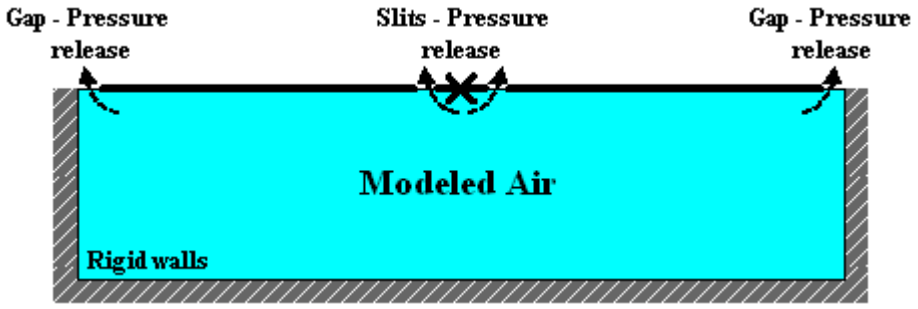


Figure 56: Fluid model of air in the backside cavity with boundary conditions

In the analysis with a directional microphone, only the air under the diaphragm is modeled as seen from Figure 56. This analysis solves the simplified Navier-Stokes equations for the fluid domain. Since the model involves moving interfaces and the movement of air, an Arbitrary Lagrangian-Eulerian (ALE) formulation is used. The air is modeled by using FLUID141 2-D fluid element, which can support the mesh displacement. After modeling, air is meshed and the boundary conditions are given such that the three surrounding walls of the backside cavity are modeled as rigid with no

translational and rotational movement. The slits on the diaphragm and the gap between the diaphragm and the substrate are modeled as pressure release boundaries through which the air can move in and out. The meshed model and boundary conditions are shown in Figure 57.

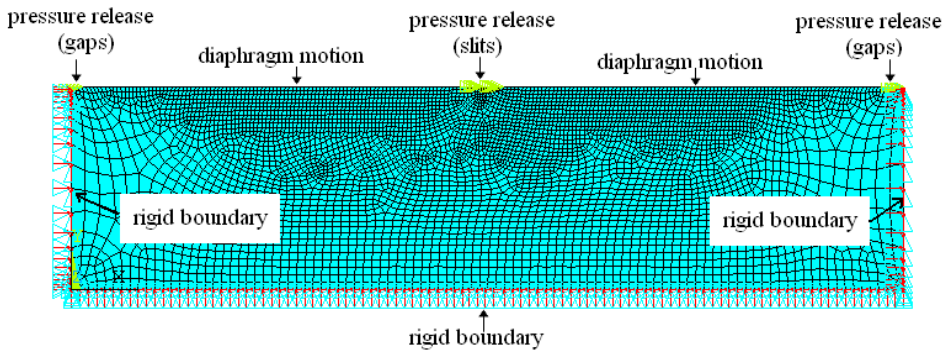


Figure 57: Meshed air domain and corresponding boundary conditions

Finally the top surface of the air, which is in contact with the diaphragm, is driven by the diaphragm motion using a short pulse velocity input as shown in Figure 58. The spatial variation of the velocity input depends on the particular mode shape obtained from structural analysis. For example, in the first mode, rocking movement causes the air in contact with each side of the top surface to move out of phase with the other. In the second mode, flapping movement causes the air to move up and down with in-phase motion. Figure 58 shows the time traces of the velocity input signal and the average pressure signal output for the second mode. Since the 2D model is used, the air movement in the third dimension is neglected. In addition to this, the CFD air model neglects the coupling effect between the two modes and solves for the single velocity at

each resonance modes. Because of these assumptions, the solution gives an approximation for the air effect which needs to be verified by measurements.

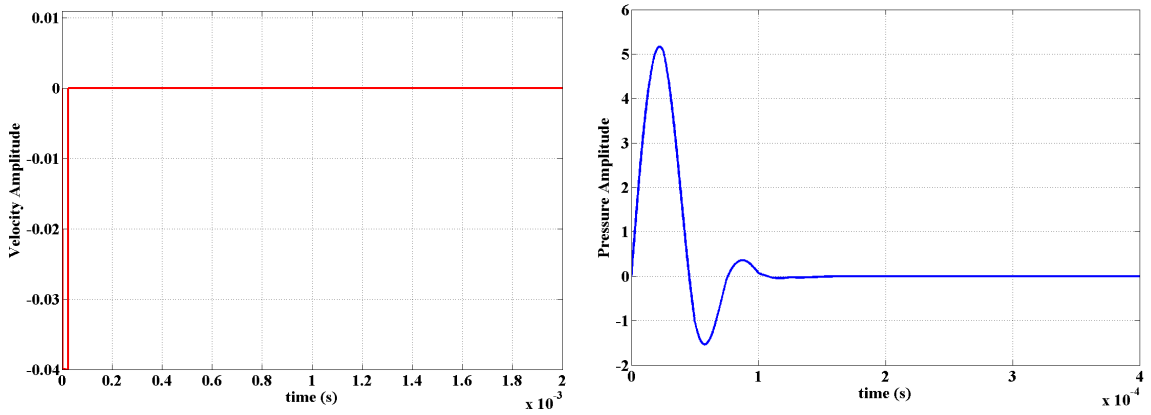


Figure 58: Velocity input and average pressure signal in time domain for the 2nd mode

Figure 59 shows the motion of the fluid under the diaphragm in the first mode. It can be seen that when the left side of the membrane moves downward and the right side moving upward, the air flows from left to right in the backside cavity. The vectors in this plot show the direction of the air flow. The velocity goes to zero by getting closer to the rigid walls. Since the dominant air movement is the movement from side to side, it does not cause much volume change and the damping effect of the air is small for the first mode.

Figure 60 shows the motion of the fluid under the diaphragm in the second mode. When the membrane is moved downwards, the pressure in the backside cavity is increased. Since there is a pressure difference between the backside cavity and the outside pressure, air starts to flow from slits on the diaphragm and from the gap between the diaphragm and the substrate. As mentioned earlier with the vacuum measurement results, the second mode motion causes the air to get squeezed. This behavior results in

higher air resistance terms for the second mode. The comparison of the air resistance terms are plotted in Figure 61.

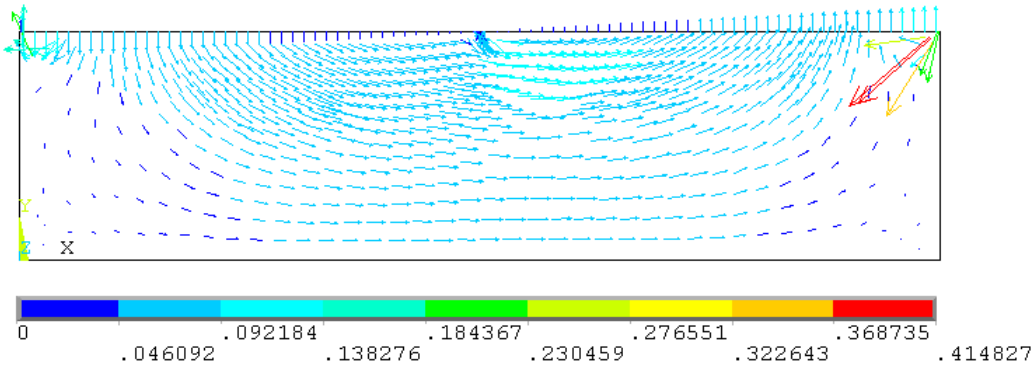


Figure 59: Vector plot showing the fluid velocity in the first mode (out of phase) of the directional diaphragm

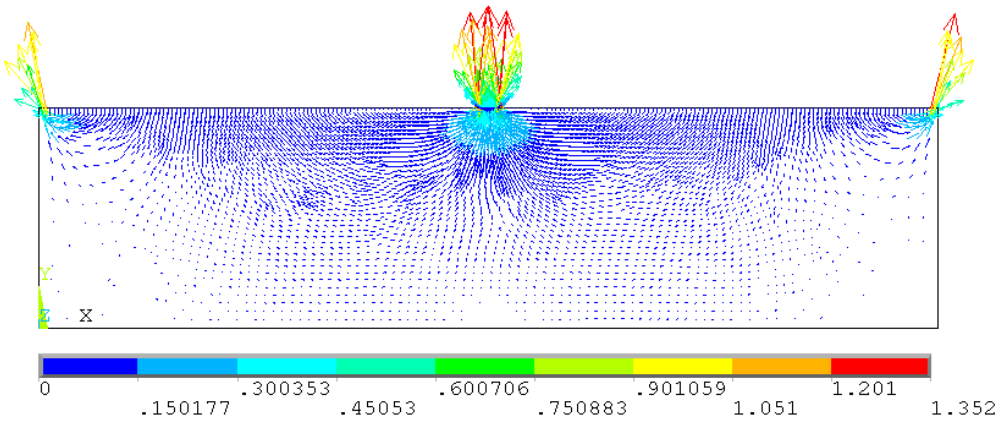


Figure 60: Vector plot showing the fluid velocity in the second mode (in phase) of the directional diaphragm

Figures 59 and 60 show only one time instant of the transient solution. The problem is solved until the effect of the input dies out and the pressure in the backside cavity equalizes with the external pressure. At each of these time steps, the position of the

nodes on the diaphragm, the pressure at each of those points, the calculated moments which cause the membrane to rotate along the pivots in the first mode are saved for post processing. Post processing is done with Matlab software by calculating the impedances from the extracted pressure output, moment output and velocity input values. The acoustic impedances caused by the effect of the air are calculated for two different modes. These complex impedances have both the resistance effect because of the flow of the air through slits and gaps, $R_{air}$, and the capacitance effect because of the air in the backside cavity, $C_{air}$, as described earlier. Figure 61 shows the calculated real and imaginary part of the impedance of the air for the first and second mode shape of the diaphragm. As seen from these figures, for both modes, the real part of the impedance, the resistance term, is constant over the frequency range. The imaginary part shows the typical capacitance impedance behavior. Since the imaginary part does not show any mass effect, using R and C for the air impedance in the equivalent circuit is acceptable. These values are used in the equivalent circuit model to predict the overall response of these microphones.

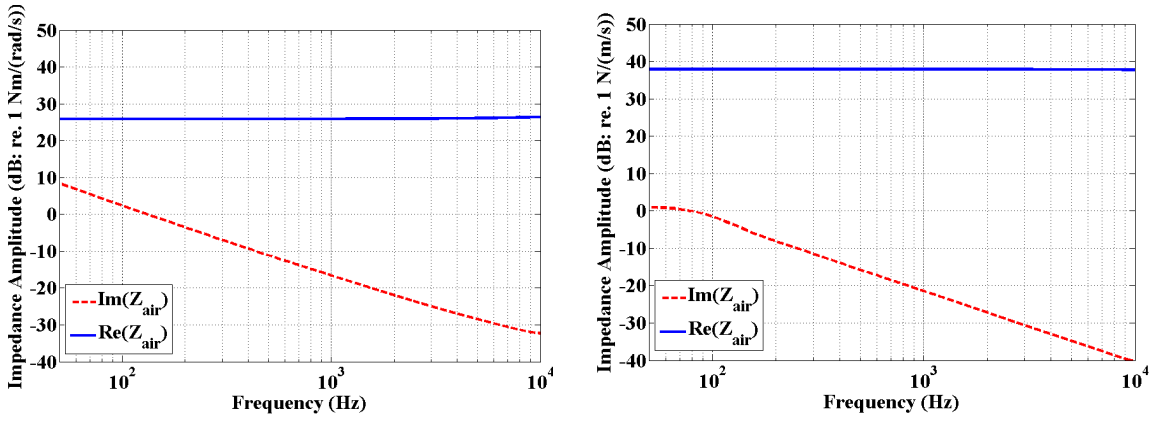


Figure 61: Impedance of the air extracted from the FLOTRAN fluid analysis for the first mode (left) and the second mode (right)

All the equivalent circuit elements, described above, have coupling effects to each other. For example, changing the equivalent mass of the first mode of the diaphragm will change the equivalent mass for the 2nd mode ($L_{dia}$), the stiffness of the modes ($C_{dia}$) and also the structural damping of the modes ($R_{dia}$). The effect of changing diaphragm parameters on the response of the microphone is investigated while optimizing the biomimetic diaphragm design [78]. In terms of the air parameters ($R_{air}$ and $C_{air}$ terms), the most important contribution for the 2nd mode, which needs to be modified for the pressure gradient measurements, comes from the term, $R_{air2}$. By simple parameter analysis, it is found that modifying $R_{air2}$ by 10% in the equivalent circuit model changes the sensitivity of the 2nd mode by 5.8%. This information is used to modify the diaphragm design to suppress the 2nd mode effect which causes problems in pressure gradient measurements.

### Effect of Higher Order Mode Shapes on the Microphone Response

The equivalent circuit model described in this chapter only uses 1st and 2nd mode shapes of the rectangular biomimetic diaphragm to predict its response. Before analyzing the predicted results with the experimental data, the validation of two mode assumption is done. In order to show the validation of this assumption, the effect of higher order modes are modeled using a finite element analysis and the contribution of each mode to the overall response is predicted. Modal participation factor analysis is used for finding the contribution of higher order mode shapes. Participation factors for each mode can be used to judge the "significance" of that vibration mode and is given as;

$$\gamma_i = \{\varphi\}_i [M_i] \{D\} \tag{35}$$

where $\gamma_i$ is the participation factor for the i$^{th}$ mode, $\{\varphi\}_i$ is the normalized eigenvectors for the i$^{th}$ mode, $[M_i]$ is the mass matrix and $\{D\}$ is the vector describing the direction. For example, for z-direction D can be written as $\{0,0,1,0,0,0\}$.

Table 4: Participation Factor Calculation (Rotation about y-direction shown in Figure 46, responding to pressure gradient)

| MODE | FREQUENCY (Hz) | PARTICIPATION FACTOR | PARTIC.FACTOR NORMALIZED | EFFECTIVE MASS (kg) |
|---|---|---|---|---|
| **1** | **810** | **0.60568E-07** | **1.000000** | **0.366844E-14** |
| 2 | 14148 | -0.10691E-13 | 0.000000 | 0.114307E-27 |
| 3 | 27909 | 0.71904E-14 | 0.000000 | 0.517025E-28 |
| 4 | 33981 | -0.48147E-13 | 0.000001 | 0.231809E-26 |
| 5 | 44598 | -0.14766E-15 | 0.000000 | 0.218026E-31 |
| 6 | 47552 | -0.38811E-15 | 0.000000 | 0.150632E-30 |
| 7 | 56884 | -0.12515E-10 | 0.000207 | 0.156620E-21 |

Table 5: Participation Factor Calculation (z-direction shown in Figure 46, responding to pressure)

| MODE | FREQUENCY (Hz) | PARTICIPATION FACTOR | PARTIC.FACTOR NORMALIZED | EFFECTIVE MASS (kg) |
|---|---|---|---|---|
| 1 | 810 | -0.14357E-10 | 0.000000 | 0.206134E-21 |
| **2** | **14148** | **-0.83862E-04** | **1.000000** | **0.703291E-08** |
| 3 | 27909 | 0.12135E-09 | 0.000001 | 0.147252E-19 |
| 4 | 33981 | 0.64880E-10 | 0.000001 | 0.420939E-20 |
| 5 | 44598 | -0.89485E-08 | 0.000107 | 0.800754E-16 |
| **6** | **47552** | **-0.47686E-04** | **0.568623** | **0.227396E-08** |
| 7 | 56884 | 0.53113E-09 | 0.000006 | 0.282099E-18 |

Tables 4 and 5 give the result of the participation factor analysis for the diaphragm responding to pressure gradient and to pressure respectively. Modes with high participation factors and high effective masses can be excited by the input excitation. From Table 4, it can be seen that the first order is the only significant mode shape that is excited with the applied pressure gradient. All the higher order modes have less than 0.02% contribution to the response as calculated from normalized participation factors. Table 5 shows the results with the applied pressure. In this case, 2nd and 6th mode, which are shown in Figure 12, are excited with the applied pressure. To see the effect of the 6th mode in audio frequency range, the frequency response of the microphone is predicted by only using 1st and 2nd mode and by adding the higher order modes. The comparison of two responses is shown in Figure 62.

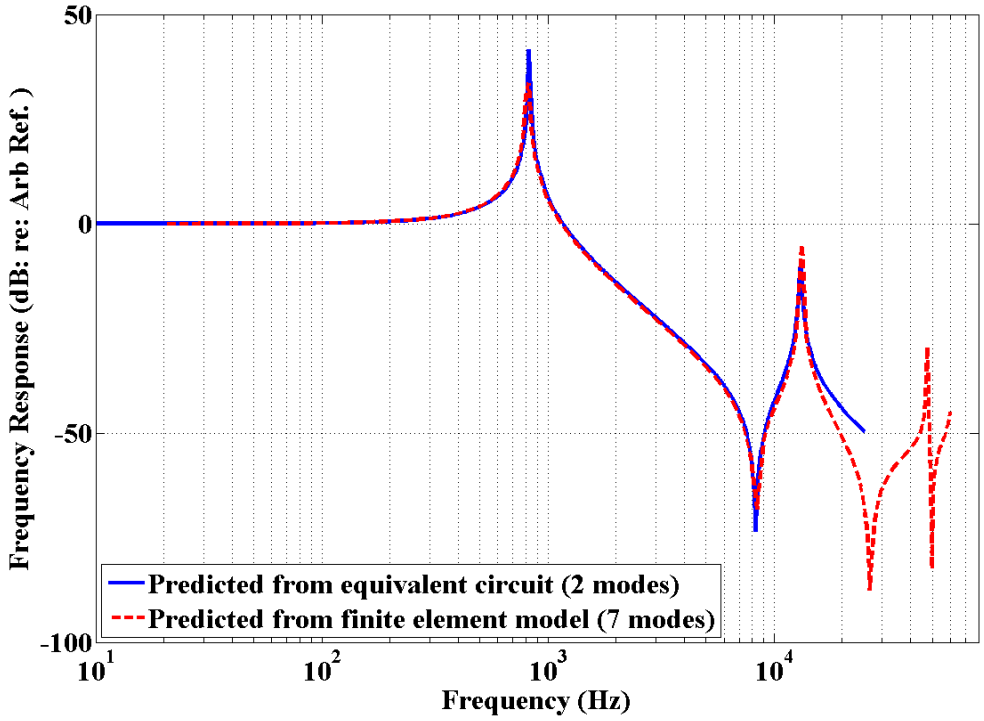


Figure 62: Predicted frequency response with equivalent circuit model that accounts for the first 2 modes and with finite element model that accounts for the first 7 modes.

Figure 62 shows that below 10 kHz, the difference between the two predicted responses is smaller than 1 dB. As the frequency goes up, the difference also increases and the maximum difference goes to 5 dB at 20 kHz. In conclusion, for most of the audio frequency range, between 20 Hz-15 kHz, the difference is smaller than 2 dB, and the effect of higher order mode shapes can be neglected.

## Verification of the Model

Since the microphone has a built-in electrostatic actuator, one can use the electrostatic response in addition to the acoustic response to verify the equivalent circuit model results. Before verifying the model, the electrostatic frequency response of the directional microphone is measured in vacuum in order to find the structural damping of different mode shapes. In order to find the response of the microphone in vacuum, a chirp signal is applied to the diaphragm from the electrostatic actuation port, and the optical detection output is monitored with a spectrum analyzer. Since the microphone is placed in vacuum, the effect of air at the backside of the differential microphone is neglected in the model. The measured data is used to find the structural damping of the mode shapes. Using this damping and other equivalent circuit parameters, the overall response is predicted as shown in Figure 63. All the parameters that are used in this model except the structural damping are extracted from FEM structural modeling for the specific diaphragm geometry.

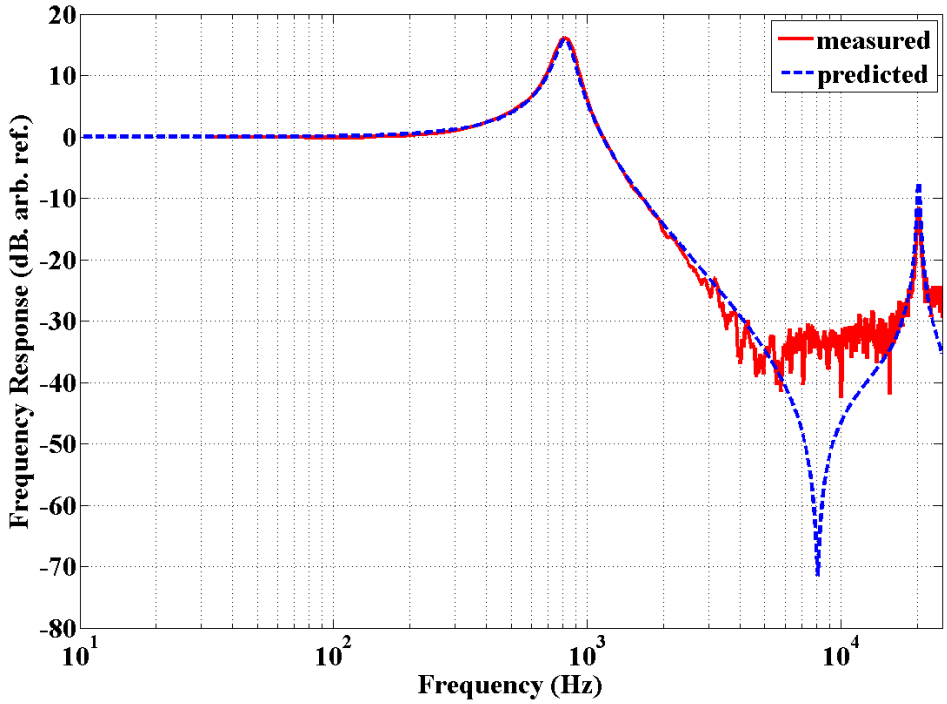


Figure 63: Measured and predicted electrostatic frequency response of differential microphone at 30 Torr vacuum.

As can be seen from Figure 63, even after the microphone is placed in vacuum, the resonance peak is damped up to a certain point. This damping comes mostly from the structural damping of the microphone diaphragm. The predicted frequency response shows good agreement with the measured response.

After finding the structural damping values by using the microphone response in vacuum, the response of the microphone in air is analyzed. In order to predict the response of the microphone in air, the equivalent circuit model is used with the parameters extracted from the ANSYS FLOTRAN model. Figure 64 shows the measured and predicted electrostatic frequency responses of the differential microphone in air. Since the measurement is performed in air, in order to reduce the effect of the external noise, the measurement is done in the anechoic chamber.

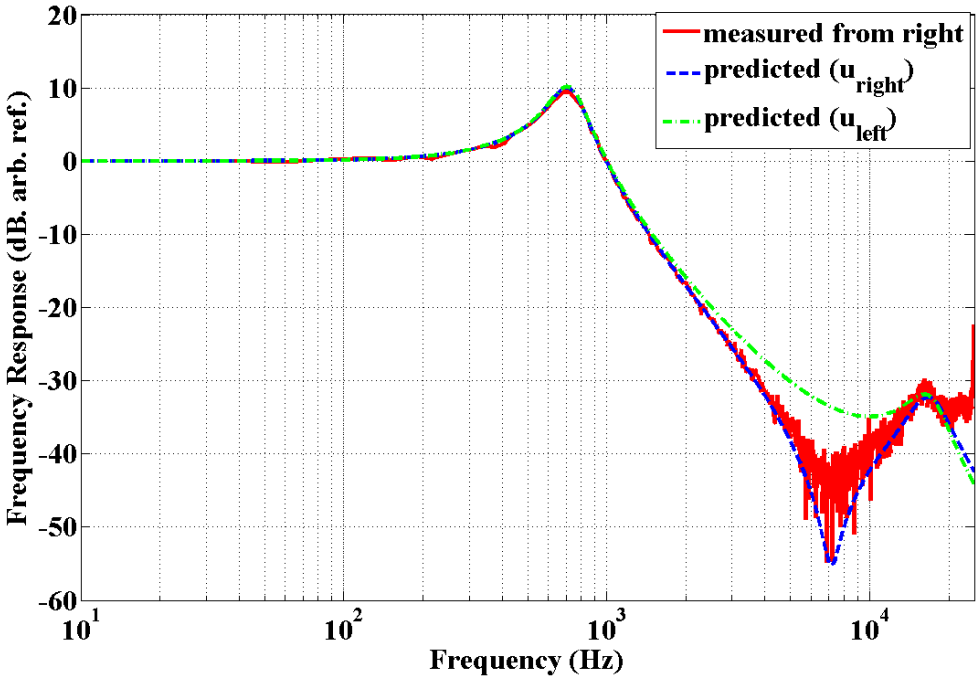


Figure 64: Measured and predicted electrostatic frequency responses of differential microphone with equivalent circuit model in the anechoic chamber

In this measurement, a chirp signal is applied to the electrostatic actuation port with proper DC bias. The signal to noise ratio (SNR) for this measurement is higher than 20 dB between 100 Hz and 20000 Hz. Even the SNR decreases below 100 Hz, overall SNR is greater than 15 dB for the measurement frequency range. The optical displacement detection output is monitored with a spectrum analyzer. The diaphragm parameters used in the model are found as described above, and while calculating the transformer constant, $\Phi_e$, the gap between the grating and the back reflector plane is taken as 4.5μm. This is reasonable since the unbiased gap of the microphone structure was designed and fabricated to be 5μm. Note that in Figure 64, there are two predicted electrostatic frequency responses with labels $u_{right}$ and $u_{left}$. These correspond to predicted optical readout signals from each side of the diaphragm as shown in the equivalent

circuit. The difference between the predicted frequency responses with left side and right side reading of optical detection method comes from the way that the diaphragm moves in different modes which is shown in Figure 65.

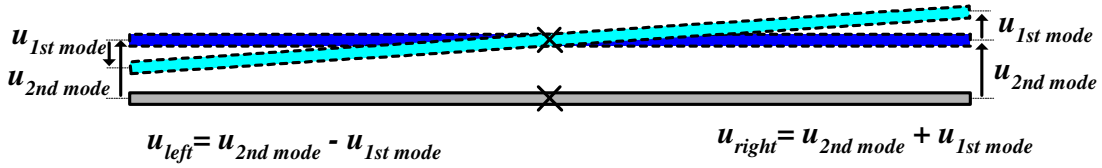


Figure 65: The effect of different mode shapes on the movement of different ends

Because the motions of the two dominant mode shapes are in opposite directions at the ends of the diaphragm, their net effect will be to add on one end and to subtract on the other end. When the second mode movement is negligible, the left side and right side motions have the same magnitude but are in the opposite direction. However if the second mode displacement is added to the first mode displacement, the overall displacement on each side of the diaphragm depends on whether the second mode movement is in the same direction or in the opposite direction of the first mode movement. Because of that, the measured optical response from opposite sides can show significant differences, especially when both modes have similar vibration amplitudes. For example, for this particular measurement shown in Figure 64, the predicted curve with $u_{right}$ matches well with the measurement especially in the 3-10 kHz range. This is expected, as the optical detection method measures the deflection from the right side of the diaphragm which is shown with the solid curve.

Overall, there is excellent agreement between the measured and predicted results, validating the air flow impedance modeling for the equivalent circuit. If the measurement

in air from Figure 64 is compared with the measured response in vacuum from Figure 63, the damping of the 2nd mode resonance peak can be easily seen because of the air effect.

The equivalent circuit model is also used for predicting the acoustic response of the directional microphones. Figure 66 shows the measured and predicted acoustic sensitivity of the biomimetic directional microphone when the acoustic wave is incident from the most sensitive point ($\phi$=90° shown in Figure 47) and the displacement is sensed from the right side of the diaphragm. For this measurement, the SNR is higher than 15 dB between 200 Hz and 15 kHz. The high frequency is limited by the speaker since it has a roll off after 15 kHz. The low frequency is limited by the amplifier of the speaker which has a low frequency cut off at 100 Hz. The SNR goes below 10 dB at frequencies below 100 Hz, which causes measurement errors.

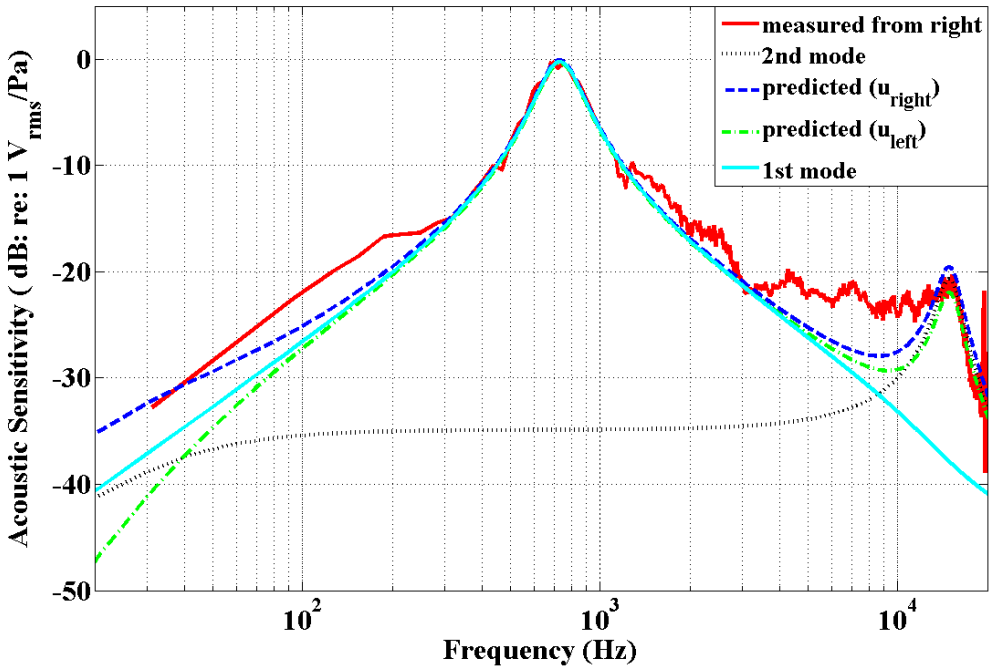


Figure 66: Measured and the predicted acoustic sensitivity of the biomimetic directional microphone when the sound is coming from the most sensitive direction, $\phi$=90°

The measured solid curve of Figure 66 is obtained in the anechoic chamber by using a Larson Davis calibration microphone as the reference. The dashed curve shows the overall predicted response of the microphone by using the equivalent circuit model. In this prediction $u_{right}$ is used, which is the case in the measured response. The measured and predicted curves show excellent agreement. If the output signal is obtained from $u_{left}$ instead of $u_{right}$ in the equivalent circuit model, the dashed-dotted curve of Figure 66 is obtained. The comparison between the two predicted curves shows that the side from which the measurement is performed affects the predicted response. As can be seen from these two predicted curves, when the first mode is dominant around its resonance frequency and the amplitude of the second mode is small compared to the first mode sensitivity amplitude between 200 Hz to 4 kHz, the difference between readings from the left or right side is not significant. However, when the second mode sensitivity is comparable to or greater than the first mode amplitude at frequencies below 200 Hz and above 4 kHz, the difference between the right and left side readings becomes significant. The reason is explained in Figure 65, which causes an unsymmetrical motion of the diaphragm. This motion results in the unsymmetrical behavior of the directionality plots described in Chapter 2. Also this second mode effect causes the PRII to be low at these frequencies described in Chapter 3.

One of the most important pieces of information that can be obtained from the model is the individual responses of the different mode shapes of the diaphragm. Since the optical detection method measures the total displacement of the microphone diaphragm, it is not possible to measure the individual responses of the different mode shapes. Because of that, predicting the individual responses with the equivalent circuit

model is a key advantage. If the pressure gradient is to be measured by using this microphone, the measurement at frequencies around the first resonance will give better results in terms of accuracy. When the effect of the second mode becomes dominant in the overall response of the microphone, especially around the second resonance frequency, the biomimetic directional microphone starts to measure the sound pressure instead of the pressure gradient because of the characteristic of the second mode. The individual prediction of the mode shapes helps one to design the microphone diaphragms according to the application.

In order to decrease the effect of the unwanted mode shape of the diaphragm and to get the desired microphone response, an optimization is done by using the equivalent circuit model. This optimization mainly includes changing the physical design of the diaphragm in order to develop a microphone for measuring pressure gradients by suppressing the second resonant mode response. In terms of the physical design, the most effective way to change the second mode response of the diaphragm is to modify the air openings in the microphone design to change $R_{air2}$ term in the equivalent circuit model. Since the second mode is an in-phase mode, it is already shown that the air in the backside cavity of the microphone has a dominant effect on the microphone response.

### Effect of Slits on the Mode Shapes

In the current design of the gradient microphones, there are slits on the diaphragm located at the center where the diaphragm is connected to the substrate with pivots. The reason for this placement is to use these slits effectively for suppressing the second mode effect while preserving the first mode sensitivity. In the first mode, when

the diaphragm moves, the air under the diaphragm moves from one side to other side and the movement of the diaphragm at the center is minimal. However, in the second mode, when the diaphragm moves up and down, the air is squeezed and some of the air flows out through the slits on the diaphragm. The slits on the diaphragm and the gap between the diaphragm and the substrate work as release holes which can be seen from Figure 62. As a result of this, by changing the dimensions and locations of the slits on the diaphragm, the effect of the second mode can be suppressed while minimally affecting the first mode response. Changing the slits and gaps dimensions affect the $R_{air}$ term in the equivalent circuit which results in the decrease of the 2nd mode sensitivity.

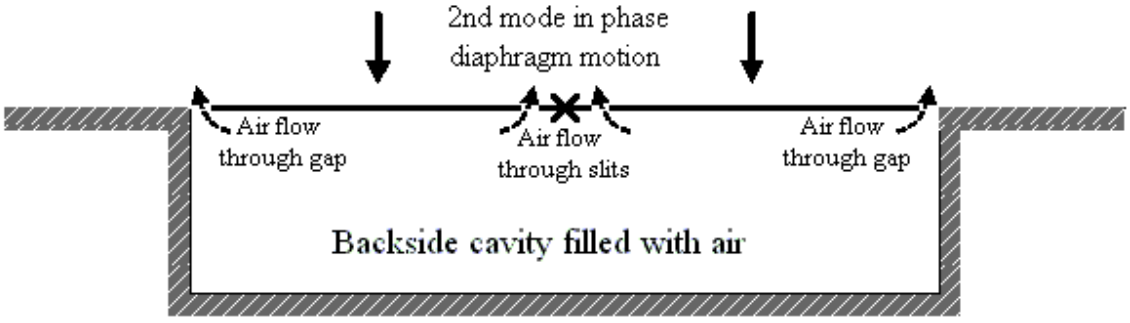


Figure 67: Schematic that shows the air flow through the gap and slits in the 2nd mode resonance (in phase mode) of the diaphragm

In order to find the optimum dimensions of the slits and holes on the diaphragm, the responses of the gradient microphone with different designs are investigated. In all the models the effect of the air is solved by using the FLOTRAN CFD analysis and is combined with the diaphragm parameters that are extracted from FEM structural analysis. The effect of the different slit dimensions on the displacement sensitivity of the diaphragm can be seen from Figure 68. The solid and the dotted-dashed curves show the

response of the directional microphone with the current design. Since the second mode response is comparable with the first order response at frequencies below 200 Hz and above 4 kHz, the overall response of the diaphragm is affected by the second mode effect. However, this second mode effect can be minimized by changing the slit dimension on the diaphragm or by changing the gap dimension between the substrate and the diaphragm.

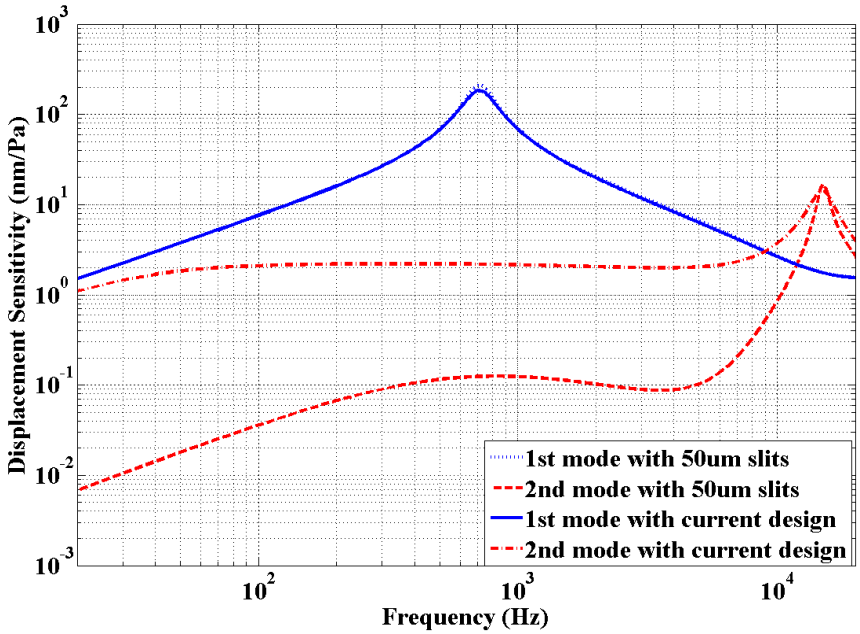


Figure 68: Displacement sensitivity of different modes of gradient diaphragm with changing slits dimensions

The dotted and the dashed curves in Figure 68 show the response of the individual modes of the diaphragm with 50μm slits on the center of the diaphragm. Increasing the slit dimensions helps the air in the back to move in and out more easily. This increases the quality factor of the diaphragm by reducing the losses and also causes the low frequency cut off to change. These changes can easily be seen from Figure 68. Since with

the larger gaps, there is less pressure difference on each side of the diaphragm, the second mode motion is driven by less pressure difference, causing the displacement sensitivity of the diaphragm to be much less than the first mode response. When the first and second mode responses are combined, it is found that with the larger slit designs, it is possible to have a diaphragm response which is only dominated by the first order mode in the 20-5000 Hz range.

The last important thing that is seen from the comparison of two different designs is the response of the first mode shape. Since the slits on the diaphragm are located at the center of the diaphragm, closer to the pivots, the sensitivity of the diaphragm does not change significantly when the dimensions of the slits are modified.

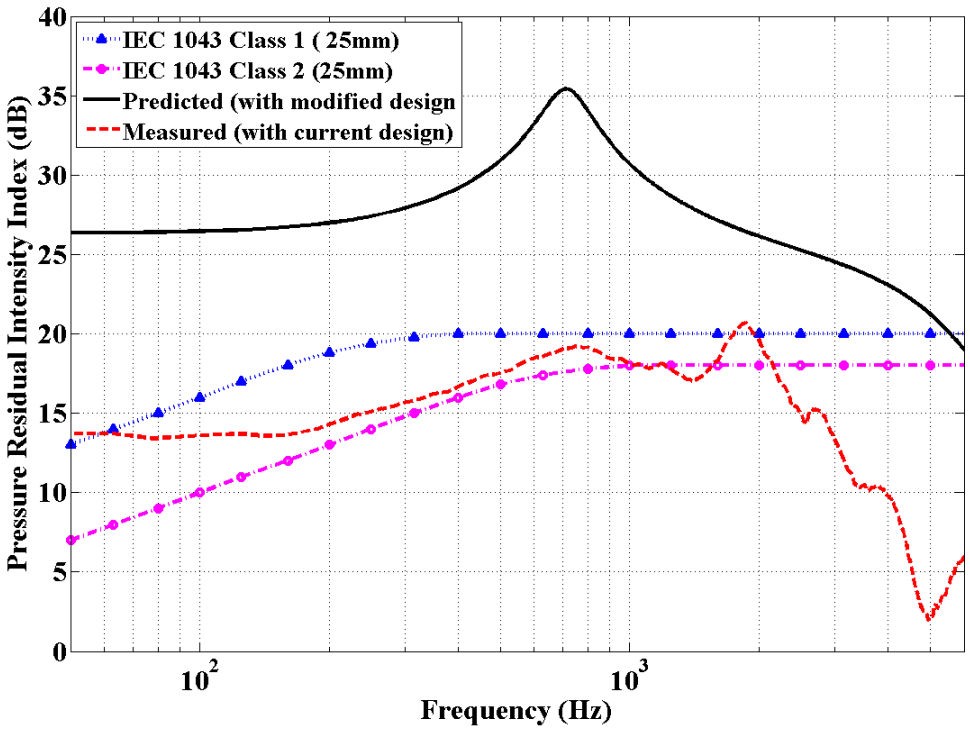


Figure 69: Comparison of pressure residual intensity index of modified gradient microphone with IEC 1043 requirements

With the suppressed second mode effect, the frequency range of the more accurate pressure gradient measurement becomes broader. To see the effect of the modifying slits on the pressure residual intensity index, the predicted response of the gradient microphone is plotted together with the IEC 1043 requirements in Figure 69. In this figure, the dashed curve shows the measured PRII with the current design and the solid curve shows the predicted residual intensity index of the gradient microphone with increased slit dimensions (50μm). Around the first resonance frequency, since the error in pressure gradient measurement is minimal, the measured intensity goes to minimum, causing a relatively high pressure residual intensity index. After 5 kHz, the pressure residual intensity index plot goes below 20 dB. The reason for that is again the effect of second mode response. With the current design modification, it can be seen from the plot that in the 50-5000 Hz range, it is possible to measure the intensity within the requirements of standards. Even the design change suppresses the second mode effect up to a certain point; an alternative method is proposed to change the dynamics of the microphone without a need for change in the design. The next chapter will describe this alternative method, namely the electrostatic force feedback method. This method is used to change the microphone's response in a desired manner. The high resonance peak and low dynamic range problems are solved by adding electronic damping with the force feedback. In addition to these improvements, the directionality and the PRII of the gradient microphones are improved by suppressing the $2^{nd}$ mode response without the design change and without adding significant noise.

# CHAPTER 5

# FORCE FEEDBACK METHOD FOR OPTICAL MICROPHONES

Using the optical detection method with biomimetic directional microphone structures enables small displacements to be measured with high sensitivity. This results in low noise directional microphones and pressure gradient measurements. As mentioned earlier, the noise floor of these directional microphones is mainly thermal noise limited. In order to decrease the thermal noise floor, passive damping of the microphone structure should be reduced. However, there is a limit in decreasing the damping of the microphone. Low damping causes high resonant peaks in microphone response which causes ringing of the microphone and reduces the dynamic range, which is not desirable. The other limitation of the optical detection method is the nonlinearity of the interferometric curve that comes from movement of the diaphragm greater than $\lambda/4$ [46]. In terms of pressure gradient and intensity measurements, it is shown that the effect of unwanted mode shapes limits the desired response. In order to eliminate the limitations of the optical detection method and to improve the performance of the optical microphones and intensity probes based on these microphones; active force feedback control can be used. This chapter describes the short history of the force feedback method and its application to different mechanical devices. Then the force feedback method with the optical microphones will be summarized. After giving the details of the force feedback theory, the implementation with optical microphones are described. Finally, the predictions of further improvements based on this technique are discussed.

## Background

Active feedback control methods have been used in many different sensor applications for improvement of dynamic range, linearity and robustness. In addition, they have been used to control thermal-mechanical noise, as in the cooling of a mechanical device, as early as the 1950s [79]. The effect of feedback on the thermal noise of the mechanical system is investigated by using a galvanometer as an example [80]. Another study shows that with force feedback, the resonant peak of the thermal noise spectrum can be attenuated [81]. One of the most important fields that uses the advantage of the force feedback method is atomic force microscopy. With the force feedback method, the resonance peak shape is determined, which is also known as Q-control [82-84]. The application of the force feedback method with the optical microphones is described earlier by Bilaniuk [22]. Using active electronic feedback for damping microphone dynamics is shown to result in low thermal noise microphones with the desirable frequency response and bandwidth [85].

## Force Feedback with Optical Microphones

As mentioned earlier, one of the most important advantages of the optical detection method is that the electrical port of the microphone is uncoupled from the sensing mechanism [22, 86]. As can be seen from Figure 70, this uncoupled electrostatic port can be used to apply a DC bias signal in addition to AC signals to the electrically conductive diaphragm and fixed gratings that form the electrode pair for electrostatic actuation. These signals can be used to pull the diaphragm to the most sensitive point on the optical curve for displacement detection sensitivity calibration and optimization [46].

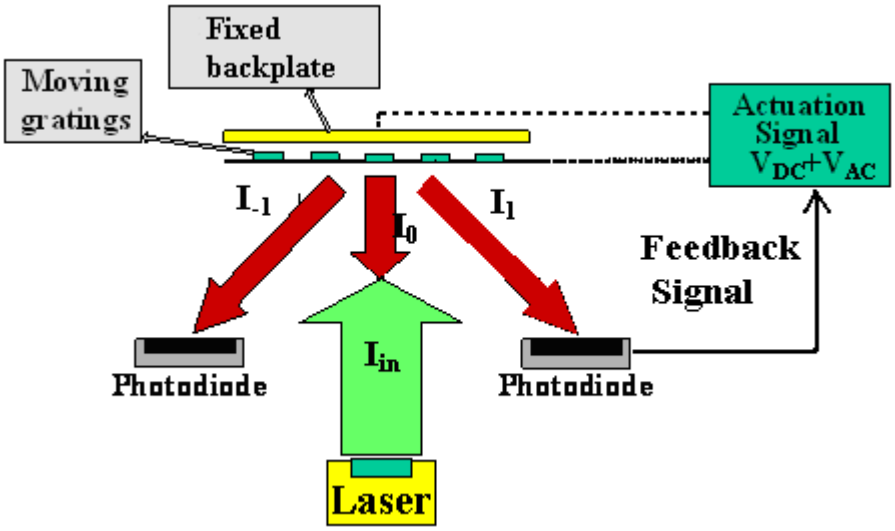


Figure 70: Basic schematic of the integrated optical detection method with electrostatic actuation capability which is used for force feedback application

Apart from tuning the optical microphone for the most sensitive point, another important use of the integrated electrostatic actuator is force feedback operation. In micromachined microphones, the force feedback capability can be used to improve the dynamics of the microphone and to operate the optical microphone in the linear range of interferometric curve, increasing its dynamic range. Used in conjunction with a low noise optical detector, this "active" damping can result in the desired frequency response and higher bandwidth without affecting the noise performance of the microphone [22, 87, 88].

### Active Force Feedback Theory

In micromachined microphones, a dominant noise source is the thermal mechanical noise due to the damping of the microphone structure. In order to minimize the noise of the microphone, damping should be minimized. As discussed earlier in this

dissertation, the gradient microphones with low damping have improved noise performance. However, low damping results in the transient ringing of the microphone and undesirable frequency response. By using the electronic force feedback method, the microphones are damped without adding significant noise. Force feedback is not only used for damping the microphones but also for increasing the bandwidth and dynamic range and improving the frequency response and linearity. The schematic of the force feedback method that is used for changing the characteristics of the optical microphones can be seen from Figure 71. In this schematic, $F_{ext}$ is the external force, $F_{tn}$ is the thermal mechanical noise force, $V_{shot}$ is the shot noise and $V_{fb\_n}$ is the feedback noise in terms of voltage. The device transfer function (DTF) gives the displacement output with the applied force in terms of m/N. For the biomimetic gradient microphone, the transfer function is derived in terms of m/Pa from the equivalent model of the diaphragm [78].

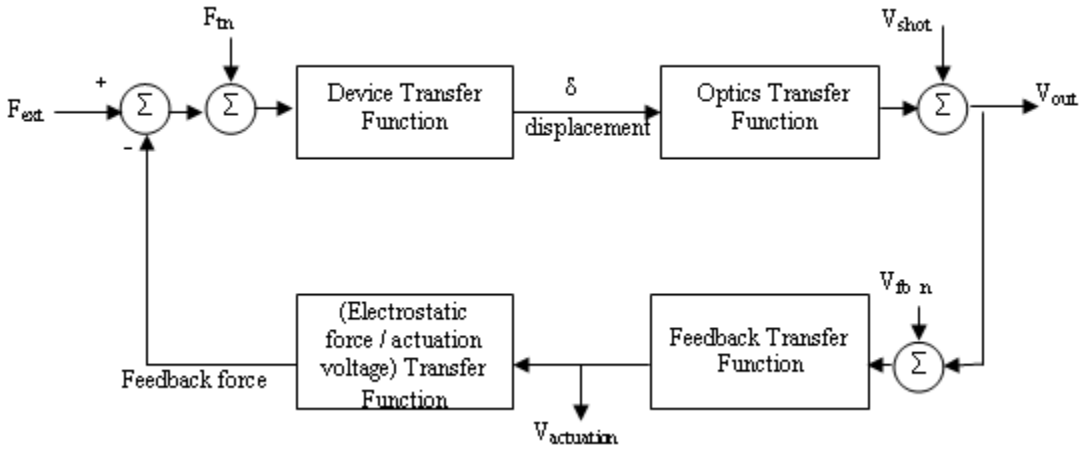


Figure 71: Block diagram of the force feedback method that is used for changing the characteristic of optical microphones.

The optical detection method senses the displacement of the diaphragm of the microphone and gives a voltage output according to this displacement. The optics transfer function (OTF), in Volts/meter, is given as,

$$OTF = \frac{2\pi V_{pp}}{\lambda} \tag{36}$$

where $V_{pp}$ is the peak to peak amplitude of the modulated signal after the transimpedance amplifier and λ is the wavelength of the light source VCSEL. This transfer function is equivalent to electrical sensitivity. Also, this sensitivity depends on the operating point on the optical curve. When the gap height does not correspond to λ/8, which is the most sensitive point on the optical curve, the displacement sensitivity will be less.

The optical detector output is fed into the feedback loop. The force feedback transfer function depends on the desired device parameter that is being modified. If the stiffness of the diaphragm needs to be changed, the proportional gain is used as the feedback signal. If damping is to be added to the system, the displacement signal is differentiated to obtain the velocity information. In that case, proportional and derivative control is used. The output of the force feedback block is the AC actuation voltage. In order to simulate the response of the diaphragm with this applied actuation voltage, this voltage needs to be converted into the actuation force. This transfer function can be found either from single parallel plate analysis or, for the complex cases, finite element modeling or direct measurements can be used to extract this value.

**Force Feedback Setup**

In order to show that the force feedback method can be used to change the device dynamics, the setup in Figure 72 is used. The optical detection method is used to detect the displacement of the diaphragm by capturing $0^{th}$ and $1^{st}$ order diffracted orders with different photodiodes. When the microphone diaphragm vibrates in response to sound, the light intensity changes in the zero and first orders are detected. The captured zero order displacement information is multiplied with a gain and differentiated to obtain the velocity output. Then this AC signal is fed into the actuation port of the optical microphone in addition to the DC bias voltage in order to operate the microphone at the most sensitive point on the optical curve. The first order output is monitored as the output of the microphone with the signal analyzer.

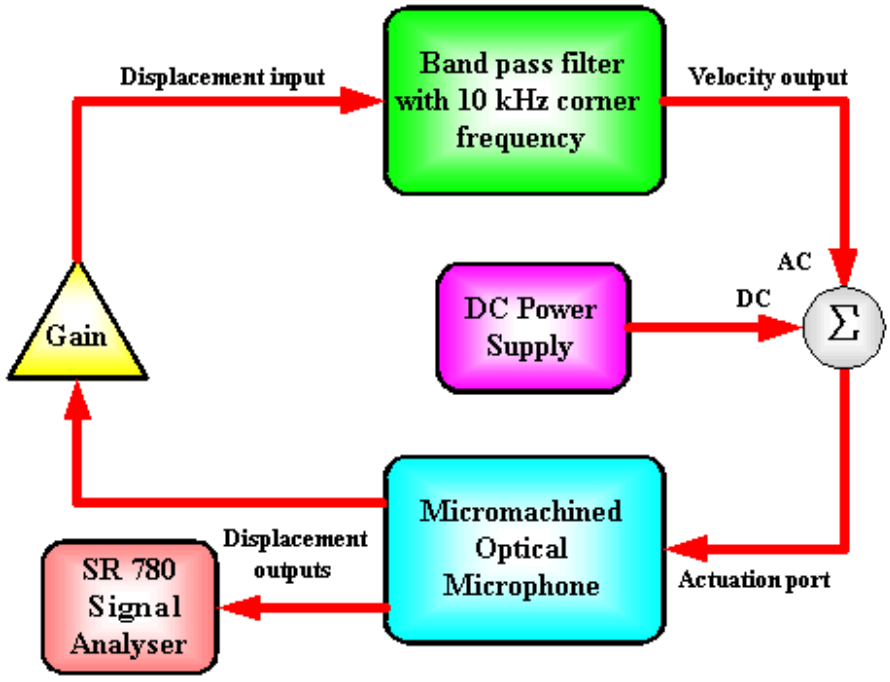


Figure 72: Force feedback test set up with micromachined optical microphone.

## Experimental Results

Using the test setup described above, it is shown that the resonant peak is reduced in level and broadened out significantly as the gain of the feedback is increased. The sensitivity of the microphone with and without feedback is plotted in Figure 73. The solid curve shows the measured sensitivity curve without applying any electrostatic force feedback signal. The resonant peak in this plot is not desirable for a good microphone because of the transient ringing and low dynamic range. With the force feedback, the sensitivity is decreased which is plotted with the dashed curve.

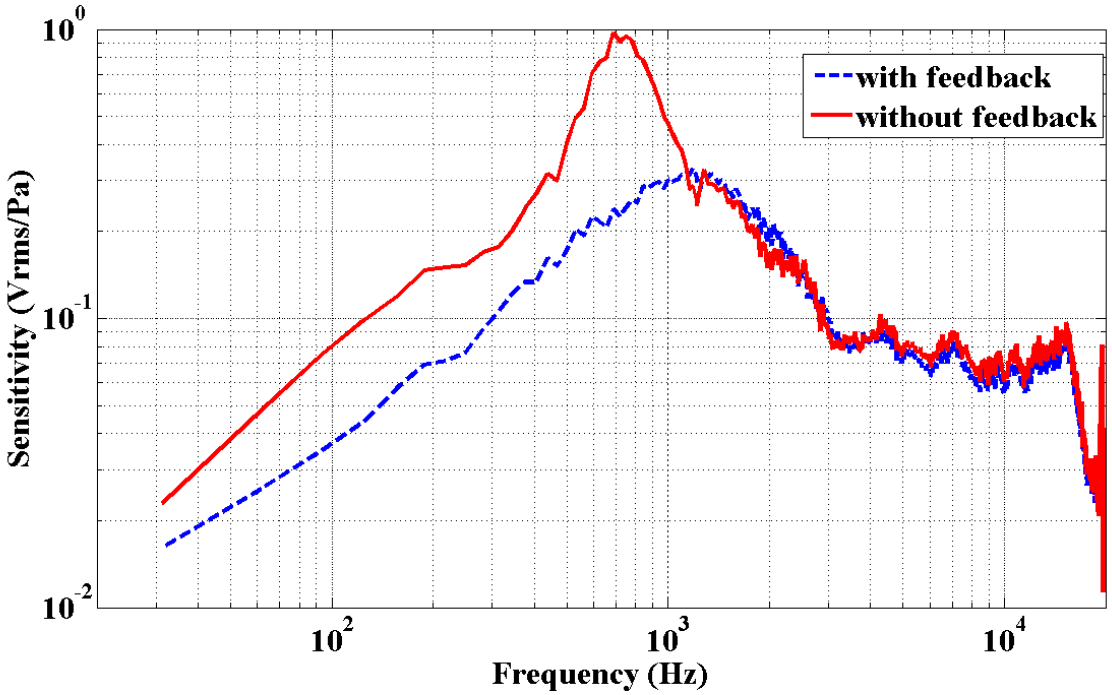


Figure 73: Comparison of microphone sensitivities with and without force feedback application.

In order to investigate the noise performance of the force feedback method, noise measurements are plotted with and without the feedback case in Figure 74. The

equivalent A-weighted noise level of the directional microphone with and without force feedback is 37 and 36 dBA, respectively. Therefore, it is concluded that force feedback does not add significant additional electronic noise across the whole frequency range.

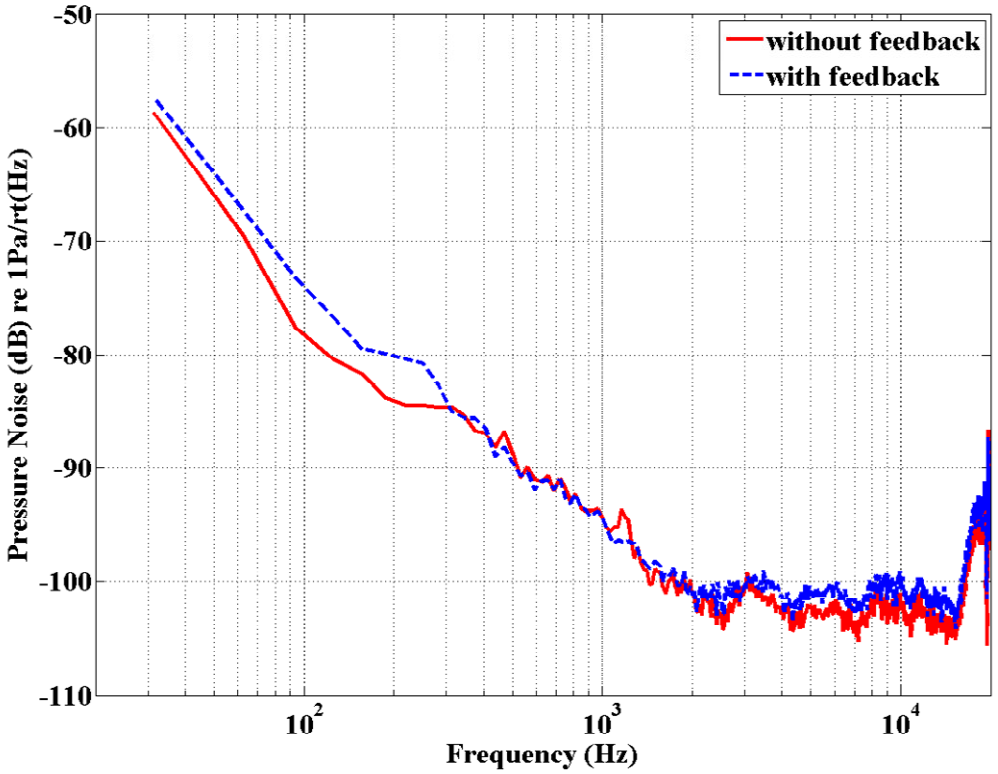


Figure 74: Comparison of pressure noise with (dashed line) and without (solid line) force feedback application.

## Modeling of Force Feedback Method

The electromechanical equivalent circuit model described earlier provides an especially useful tool to predict optical microphone response with force feedback. The modified model can be seen from Figure 75.

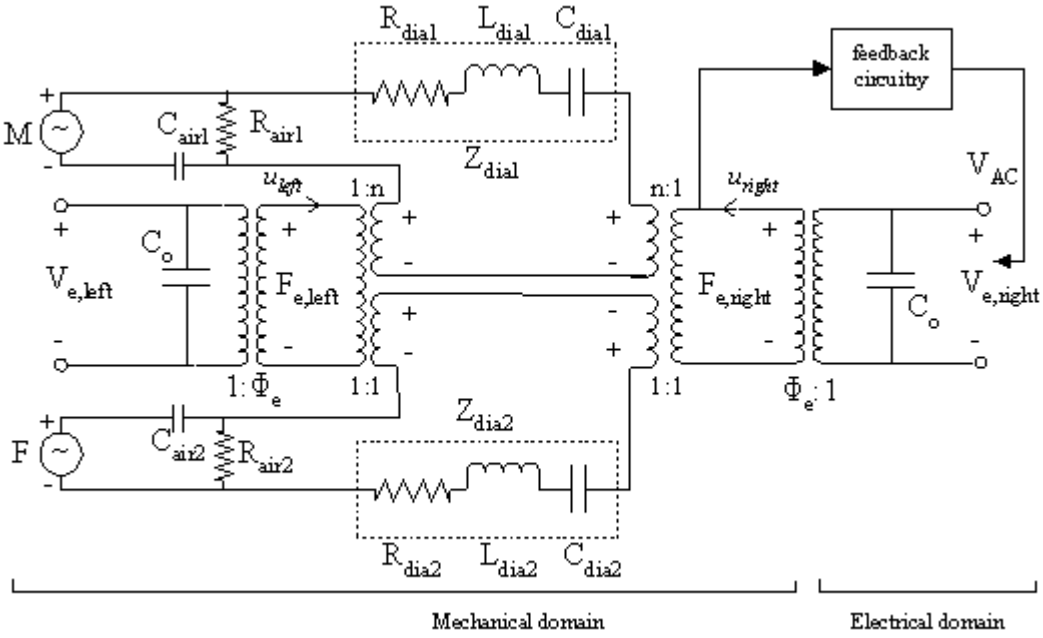


Figure 75: Equivalent circuit model of the optical directional microphone with force feedback application

As can be seen from this figure, the only modification in this circuit is the addition of the force feedback loop. In this circuit, the optical detection method detects the displacement of the circuit, and this information is sent to the force feedback circuitry. For this particular case, the damping of the microphone is changed by using proportional and differential signals generated by gain and filter applications. After this modification, this signal is fed back into the actuation port of the optical microphone. As a result of this, the total applied electrostatic application signal is the combination of DC bias, which is applied to hold the membrane at its most sensitive point, and AC signal which comes from the force feedback application. In this circuit, the optical detection senses the movement of the diaphragm from the right side and the force feedback actuation signal is fed back from the same side electrostatic actuation port. This selection

is just for demonstration. The force feedback signal can be applied to both sides of the diaphragm using the displacement information obtained from either side of the diaphragm readout. The effect of applying the force feedback signal from single or both sides will be described in detail later in this chapter.

Using the modified equivalent circuit that is described above, the response of the optical gradient microphones with force feedback is predicted. The results of this prediction along with the measured responses are plotted in Figure 76.

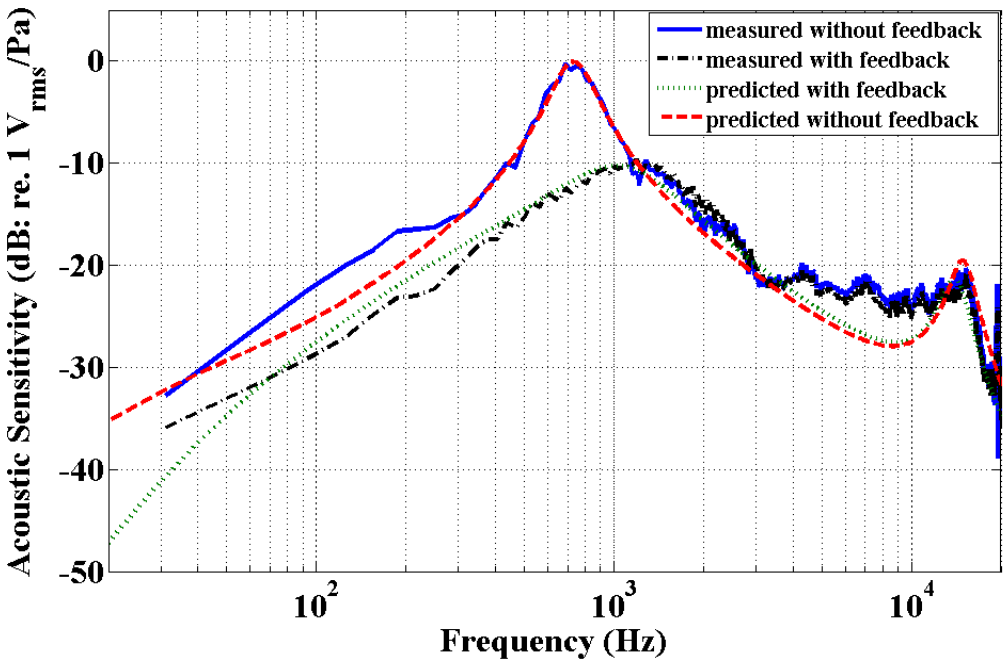


Figure 76: Comparison of measured and predicted acoustic sensitivities with and without force feedback application

The solid and dashed-dotted curves are measured responses with and without the feedback. The dotted curve shows the predicted acoustic sensitivity response of the optical gradient microphone with force feedback. This curve matches with the measured

dashed-dotted curve except frequencies between 4 kHz – 11 kHz. The difference between the measured and predicted curves at these frequencies may come from the measurement errors. With the application of force feedback, it can be seen that the first resonance peak of the microphone diaphragm is damped with additional electronic damping. This force feedback modification will prevent the excessive movement of the microphone diaphragm at its resonance frequency. As a result of this damping, the transient ringing and nonlinearity of the response are prevented.

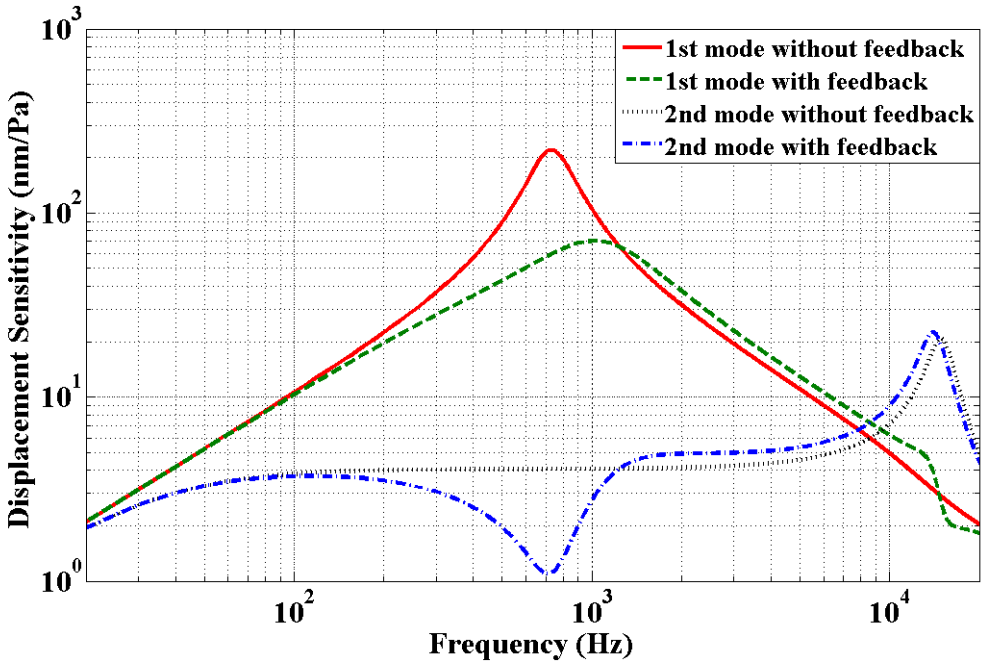


Figure 77: Comparison of predicted 1st and 2nd mode displacement amplitudes with and without feedback

Figure 77 shows the predicted displacement sensitivities of the 1st and 2nd mode shapes separately. The solid curve shows the predicted movement without the force feedback application. The maximum displacement of the microphone diaphragm at the 1st

resonance is around 220nm/Pa without force feedback. With the application of feedback, this movement is reduced to ~70nm/Pa, shown with the dashed curve. In the optical detection method, a laser with 850nm wavelength is used. This sets the linear operation range of the diaphragm movement to be less than 212nm. From this calculation, it can be concluded that the nonlinearity in the microphone response, caused by the excessive movement of the diaphragm at resonance, can be reduced by the force feedback application. This results in the linear response of the microphone with increased dynamic range. The calculated dynamic range at the 1$^{st}$ resonance frequency is increased from 91 dB to 104 dB with the application of force feedback. Table 6 summarizes the calculated dynamic range values. For the ideal dynamic range, shot noise limit is used as the minimum detectable level. However, for the dynamic range calculations with and without feedback cases, the measured noise limit is used as the baseline.

Table 6: Calculated dynamic range values with and without force feedback

| | |
|---|---|
| Ideal dynamic range<br>(calculated from shot noise limit) | **130 dB** |
| Dynamic Range<br>(without feedback) | **91 dB**<br>*at the 1$^{st}$ mode resonance* |
| Minimum detectable pressure limit<br>(without feedback) | **36 dBA**<br>*(noise floor in the audio band)* |
| Dynamic Range<br>(with feedback) | **104 dB**<br>*at the 1$^{st}$ mode resonance* |
| Minimum detectable pressure limit<br>(with feedback) | **37 dBA**<br>*(noise floor in the audio band)* |

## Two-Sided Force Feedback Method

As described earlier, the main difficulty with the pressure gradient measurement using the optical gradient microphone is the result of the unwanted pressure sensitive 2nd vibration mode of the diaphragm. In this mode shape, the diaphragm undergoes an in-phase motion and responds to pressure like an omnidirectional microphone instead of responding to pressure gradient. To measure the pressure gradient in a wider bandwidth with these optical gradient microphones, the effect of the second mode in-phase motion needs to be minimized. The electrostatic force feedback can also be used to control individual modes using a more general scheme as shown Figure 78. In this setup, electrostatic force feedback signals are applied from both sides instead of just one side of the diaphragm.

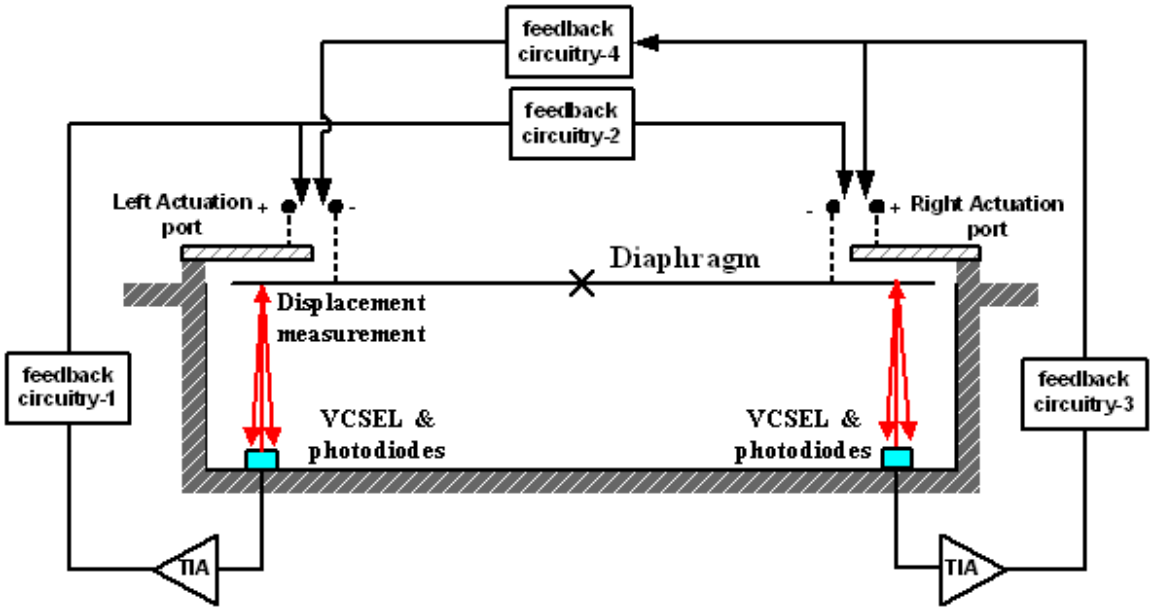


Figure 78: General schematic of the force feedback application to two sides of the diaphragm with optical detection method on both sides.

As described earlier, the displacement of the diaphragm can be sensed by optical detection from either or both sides of the diaphragm. This displacement information is passed through feedback circuits and applied to both electrostatic ports located on each side of the diaphragm. Individual force feedback signals can be controlled by different feedback circuits as shown in the schematic. For example, feedback circuits 1 and 2 is used to modify the force feedback signal applied to the left and right actuation ports respectively when the optical detection reads the displacement output from the left side of the diaphragm. These feedback circuits can apply just a gain or differential and gain signals, depending on the parameter that needs to be tuned by feedback. One configuration of this force feedback approach is the application of same (in phase or out of phase) signals to both ends of the diaphragm to match the phase relationship between the desired and undesired modes.

The main purpose in applying two-sided feedback is to decrease the second mode effect of the diaphragm so that in the whole audio frequency range, the overall response of the diaphragm is dominated by the first mode movement, which is sensitive to the pressure gradient. This modification will result in the decrease of the measured residual intensity and will increase the pressure residual intensity index of these optical gradient microphones. By using the schematic shown in Figure 78 with only one-sided optical displacement detection and using a PD scheme in the feedback circuitry, the response of the gradient microphone is predicted and is plotted in Figure 79.

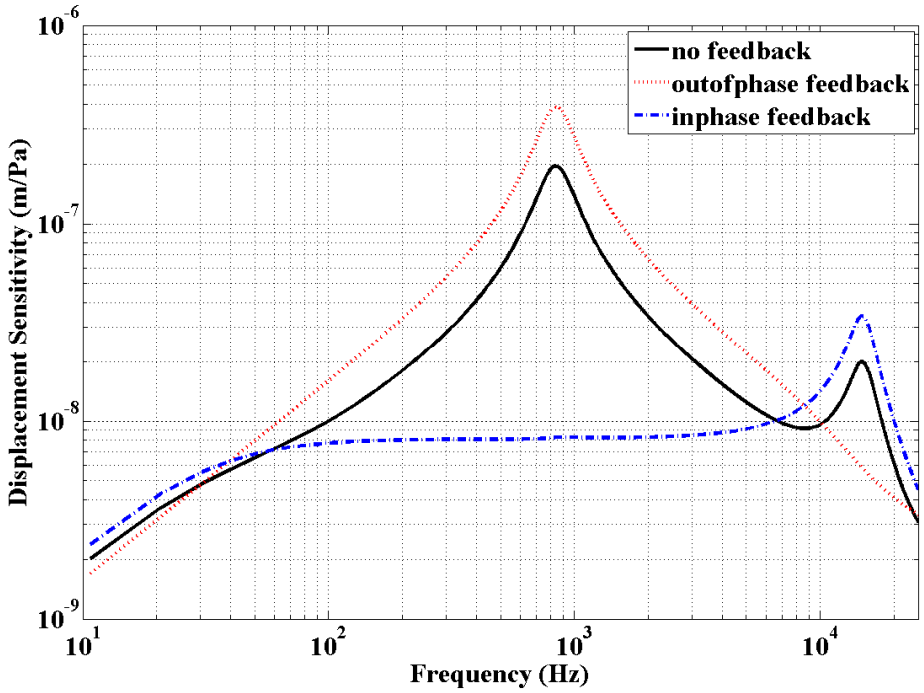


Figure 79: Displacement sensitivity vs. frequency with different configurations of force feedback application

When there is no feedback applied, the displacement sensitivity of the diaphragm is plotted with the solid curve in Figure 79. In this response, the effect of both mode shapes can be seen with their resonance peaks. As described earlier, in order to measure the pressure gradient correctly with these microphones, the effect of the second mode needs to be eliminated. The dotted curve in Figure 79 shows the response of the diaphragm with the applied out of phase feedback signal. In this configuration, the displacement information from the optical detection method is passed through the PD controller with gain 10 and fed back to the electrostatic ports. There is an inverter between the signals applied to different electrostatic ports in order to keep two electrostatic signals out of phase. As seen from the dotted curve, the overall response of the gradient microphone response is dominated by only the first mode which is ideal for

accurate particle velocity measurements. The dotted-dashed curve in this figure is obtained by applying an in phase electrostatic feedback signal to both actuation ports of the diaphragm. In this configuration, there is no inverter used and the gain used for the PD controller is 20. By applying an in phase signal, the first mode effect can be suppressed if it is needed. This model shows that it is possible to suppress the individual mode shapes by applying force feedback from both sides of the diaphragm. By using this information, it can be concluded that these directional microphones can be tuned to measure predominantly the pressure gradient or pressure. For the out-of-phase feedback case, the individual vibration mode movements are shown in Figure 80.

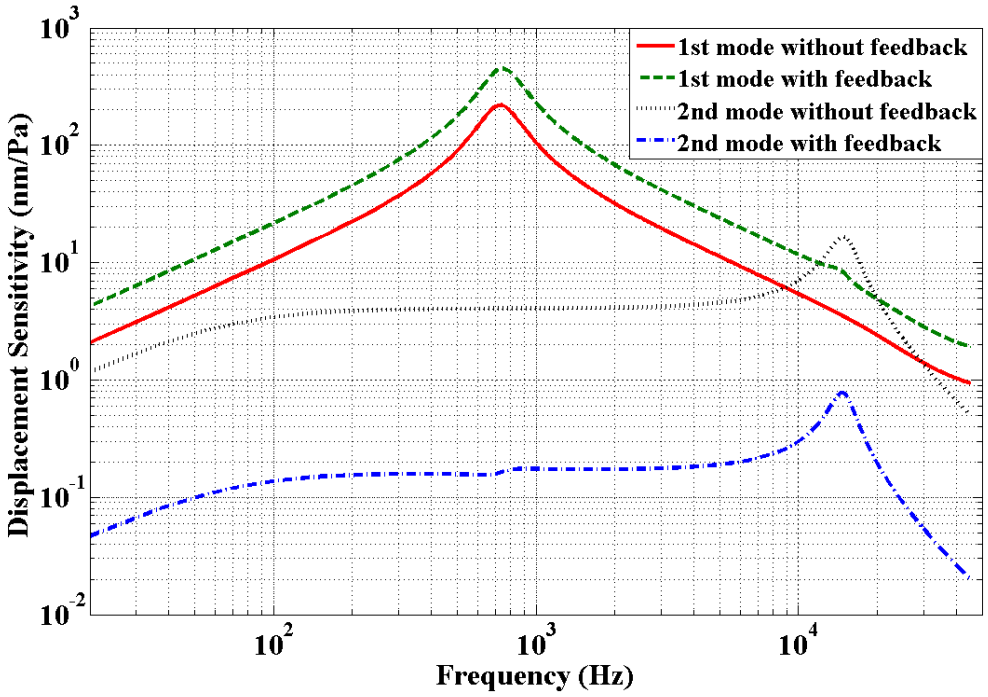


Figure 80: Modification of the displacement amplitudes of individual vibration mode movements with out of phase force feedback application

In Figure 80, the solid and the dotted curves show the response of the 1st mode and 2nd mode of the optical gradient microphone without the force feedback application respectively. As described earlier, the overall response is affected by the 2nd mode motion at frequencies below 200 Hz and above 4 kHz. The dashed and dotted-dashed curves show the change of the individual mode movement changes with the application of out-of-phase feedback. As seen from the figure, while the feedback improves the sensitivity of the 1st vibrational mode, the second mode movement is suppressed for the whole frequency range. This suppression will enable these microphones to measure only the pressure gradient between 50 Hz to 10 kHz frequency range.

As seen from Figure 80, the out of phase force feedback application suppress the 2nd mode movement as desired for the pressure gradient measurements. However, the highly resonance behavior of the 1st mode still causes the gradient microphone to operate nonlinearly. In order to solve this high resonance and nonlinearity problems, two-sided feedback is applied in different configuration to suppress the 2nd mode effect while damping the 1st mode resonance peak. This application shows the addition of electronic damping similar to one-sided feedback case in combination with the two sided out of phase feedback. The predicted results are shown in Figure 81. In this figure the solid curve, the response without the feedback case, is damped as shown in the dashed curve. While damping the 1st mode, the 2nd mode motion is suppressed as can be seen from the dotted and the dotted dashed curves. This suppression results in the improvement of the PRII of the gradient microphone which will be discussed in the next section.

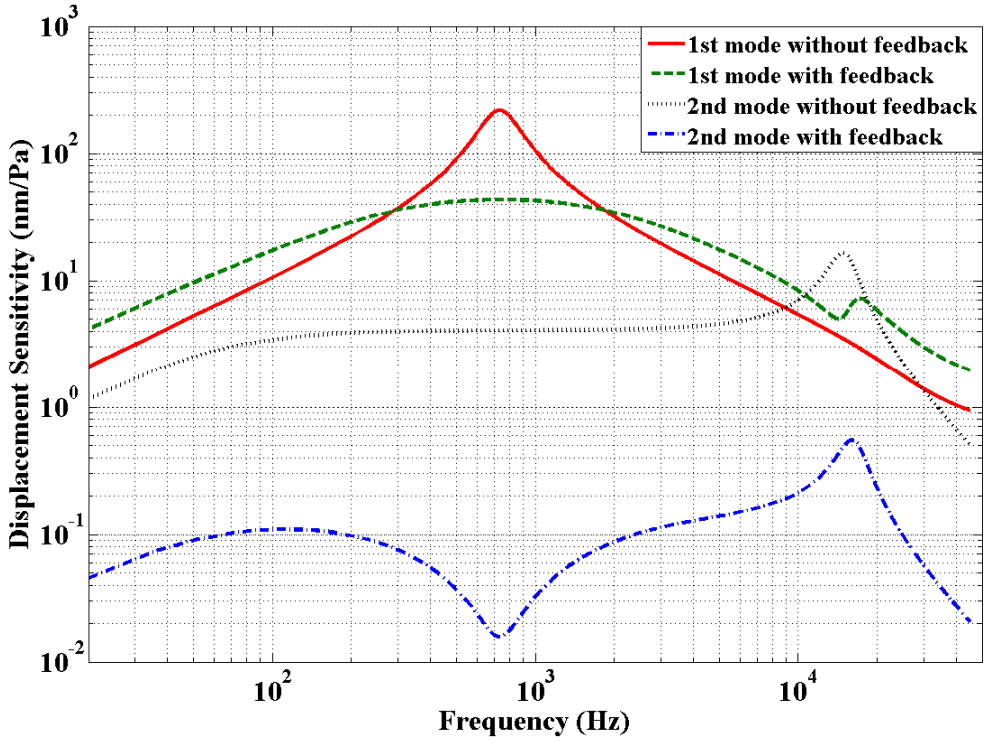


Figure 81: The first and the second vibrational mode displacement with and without the out of phase force feedback with addition of electronic damping

**Improving the Directionality and PRII with Two-Sided Force Feedback**

The most important result of suppressing the second mode with two-sided force feedback is the improvement in the directionality pattern of these differential microphones. In order to show this improvement, the directionality plots of these microphones at different frequencies are shown in Figure 82.

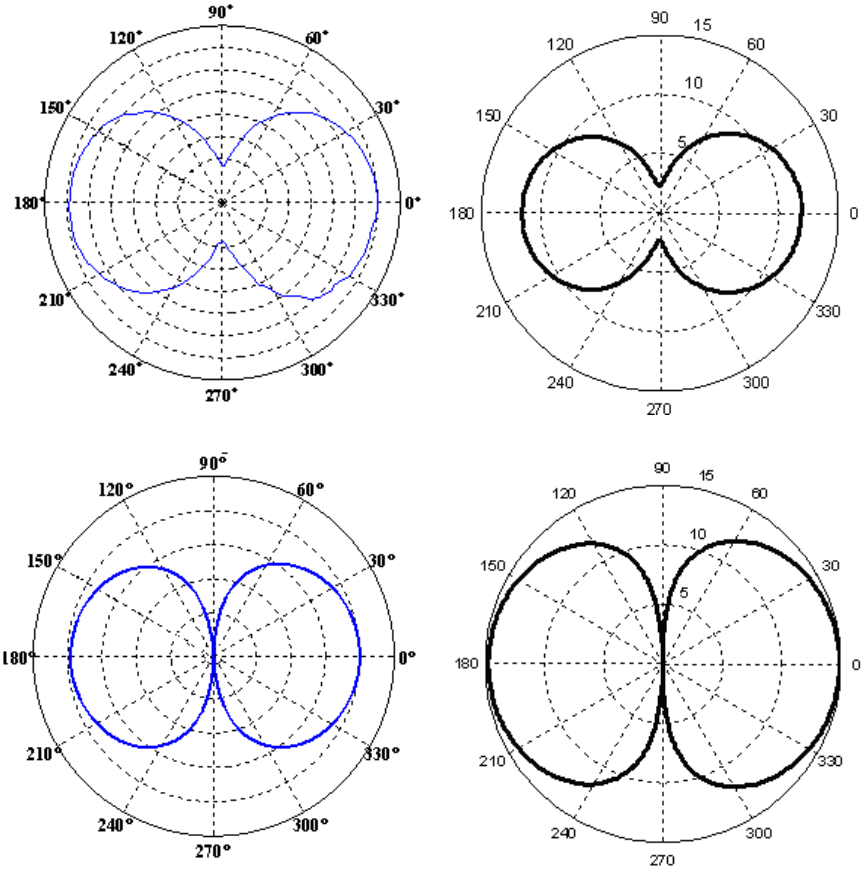


Figure 82: Measured (left) and predicted (right) directionality plots of differential microphone at 100 Hz (top) and at resonance frequency of the 1st mode (bottom)

As seen from the top plots at Figure 82, the directionality response of these differential microphones is not reaching its minimum values at 90° and -90°. The offset at these angles comes from the movement of the second mode which has an omnidirectional behavior. However at frequencies around the resonance frequency of the first mode, the microphone responds to the pressure gradient, and the resulting directionality plot looks like an ideal Figure-8 pattern, as seen from the bottom plots at Figure 82.

The result of the predicted directionality plots with two-sided out-of-phase electrostatic force feedback can be seen from Figure 83. The solid curve shows the response of the directional microphone without any feedback. At 100 Hz, it can be seen

that the directionality plot is not ideal because of the second mode in-phase motion. The dotted curve which is the predicted response curve with the applied out-of-phase feedback shows the improved directional behavior. Since the overall response with the out-of-phase feedback is dominated by the 1st mode motion, the response shows similarity to the ideal Figure-8 pattern.

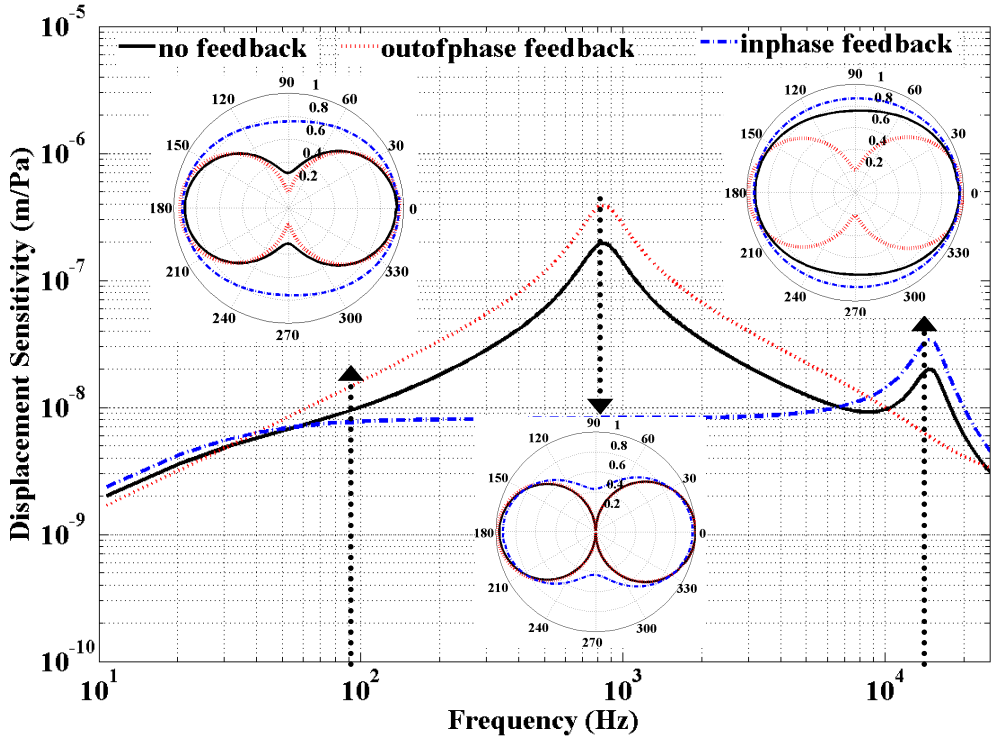


Figure 83: Modification of directionality response at 100 Hz, 1st and 2nd resonance frequencies with out-of-phase and in-phase feedback application

If the directionality plots at the first resonance mode are investigated from Figure 83, it is shown that the out-of-phase feedback improves the symmetry of the directional response. Even at this frequency, the dotted-dashed curve, which is the predicted response of the microphone with the in-phase feedback, shows the omnidirectional

behavior. At the second mode resonance frequency, no feedback curve shows the omnidirectional behavior which is the result of the dominant in-phase motion. In the prediction curves with the two-sided force feedback application, this response can be changed to be directional by suppressing the in-phase mode effect by out-of-phase feedback or it can be changed to be ideally omnidirectional by suppressing the out-of-phase mode by in-phase feedback. This demonstrates that two-sided electrostatic force feedback can be used to adjust the directivity of differential microphones by tailoring the responses to pressure and pressure gradient. By improving the pressure gradient measurement ability of these directional microphones, accurate velocity measurements can be done in a frequency range between 50 Hz-10 kHz.

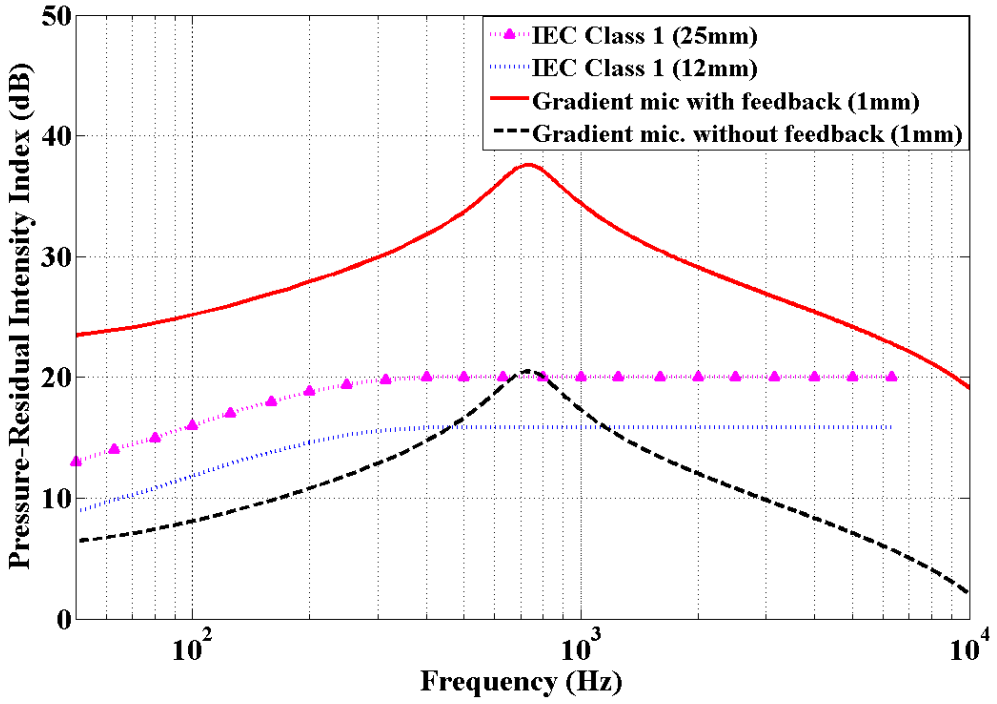


Figure 84: Improvement on the predicted pressure residual intensity index with out-of-phase force feedback application and comparison with IEC 1043 standard requirements *(for the configuration shown in Figure 80)*

The improvement on the pressure residual intensity index by using two-sided force feedback is shown in Figure 84. This figure shows the predicted pressure residual intensity index of these gradient microphones with and without feedback case from Figure 80. With the application of out-of-phase feedback, the pressure residual intensity index can be improved by more than 15 dB. With this improvement, the predicted residual intensity index meets and exceeds IEC 1043 Class 1 standard requirements. The other important point to note is that the standards are defined for commercially available 12mm and 25mm spacing distance. However the gradient microphone, which is much smaller in size than a commercial sound intensity probe, meets the requirements with only 1mm port spacing and without need for multiple spacers.

As described earlier, by the addition of the damping with the two sided feedback application, the 1$^{st}$ resonance mode can be damped as shown in Figure 81. Using this configuration, the predicted residual intensity index of the gradient microphone is shown in Figure 85. It can be seen from this figure that, the high resonance peak can be damped without sacrificing too much from its sensitivity. The predicted PRII is still higher than 20 dB until 8 kHz which is above the IEC 1043 standard requirements. The standard curves are plotted until 6.5 kHz because they are defined only for that frequency range.

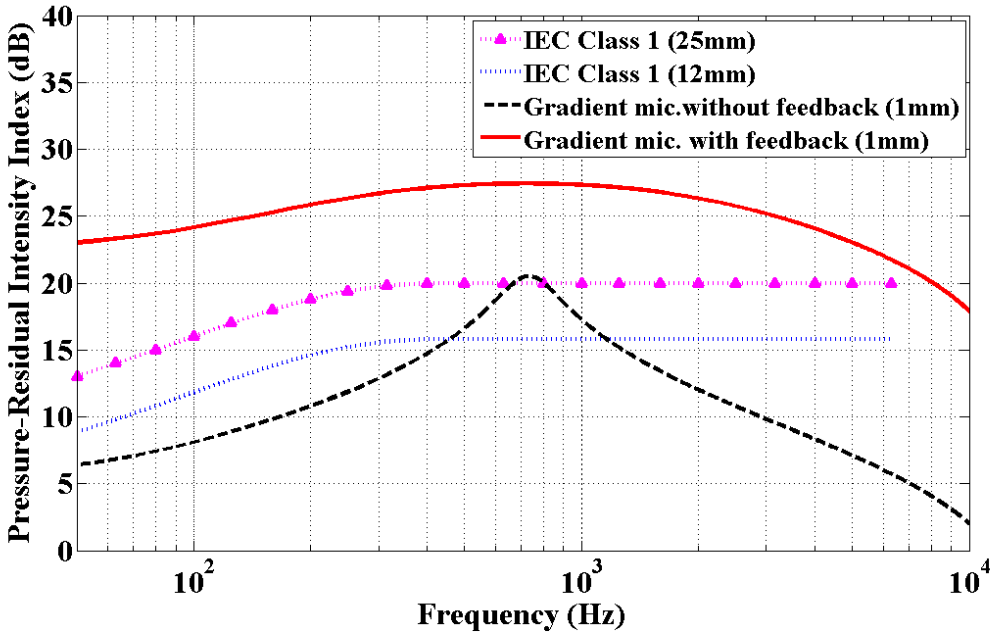


Figure 85: Improvement on the predicted pressure residual intensity index with out-of-phase force feedback application and comparison with IEC 1043 standard requirements *(for the configuration shown in Figure 81)*

In conclusion, it is shown that individual vibration modes can be modified with different configurations of two sided force feedback. This enables one to suppress the second mode motion, which makes the differential microphone sensitive to pressure gradient in a wider frequency range. By suppressing the second mode motion, directionality plots are shown to be improved, resulting in more symmetrical Figure-8 like patterns. These improvements enable more accurate pressure gradient measurements, making these differential microphones candidates for small size particle velocity sensors. Since the force feedback signal applied to both sides of the diaphragm can be controlled individually, correction of asymmetric responses caused by the fabrication or one-sided detection schemes may also be possible. In addition to these, the microphone response can be significantly improved by reading displacement only from one side and using two-

sided electronic feedback, eliminating the need for two optical detection methods on both sides of the microphone diaphragm.

# CHAPTER 6

# CONCLUSION

This thesis presents the implementation, modeling and characterization of micromachined optical biomimetic gradient microphones as well as their application to sound intensity measurement. These microphones combine a diffraction based optical detection method with a novel microphone diaphragm structure inspired by the fly *Ormia ochracea*. The high sensitivity and low noise of optical sensing and inherently low thermal noise and high mechanical sensitivity of the biomimetic diaphragms result in pressure gradient microphones with 36dBA noise levels and 1 mm port spacing. In addition to achieving this remarkable performance, shown to be better than current directional microphones [18], the optical sensing method utilized in this microphone also provides electrostatic actuation capability, which is exploited for force feedback method implementation.

In Chapter 2, the biomimetic microphone diaphragms and its modal properties are discussed in addition to describing the integration of the optical detection method with these diaphragms to implement a gradient microphone. The dimensions of the package, which contains 2 directional and 1 omnidirectional microphone, is 8mm x 8mm x 2mm. Characterization of the directional microphones is performed and the results show that these microphones have high sensitivity with figure-8 like directionality response. To evaluate the performance and efficiency of the optical detection method, a detailed optical model is developed. The efficiency of the optical detection method with the microphone structures is observed to be affected by many important parameters like

laser beam divergence angle, spot size on the diffraction gratings, the propagation distance between the laser and the grating plane and any tilt or misalignment in the overall system. Even the overall efficiency of the optical detection method is found to be 1%; these microphones have better or comparable performances in terms of size, noise and sensitivity than commercial directional microphones. Low optical efficiency can be improved by reducing the laser spot size on the grating plane, which causes direct light reflection and power loss. Future work can be the implementation of optical elements like a micro-lens to focus the incoming VCSEL light into a small spot on the grating plane and steer the reflected orders onto the photodiodes. Another future work to increase the efficiency of the optical detection can be the use of automatic pick & place system in positioning and aligning VCSEL and photodiodes instead of manual placement during the integration.

An important application of these optical gradient microphones is sound intensity probes. Chapter 3 investigates the capability of these microphones to measure particle velocity, which is the main component needed for sound intensity measurements. Comparisons with existing commercial probes show that optical gradient microphones are useful in measuring the sound intensity when the particle velocity in the field is higher than $2x10^{-6}$ m/s. However, the measured pressure residual intensity index is about 10-15dB lower than that obtained with a commercial intensity probe. The main problem in measuring the sound intensity comes from the effect of the in-phase mode which is sensitive to pressure instead of pressure gradient. This problem is addressed by the force feedback method, described in Chapter 5.

In Chapter 4, an equivalent circuit model is developed to predict the response of the optical microphones for different applications. This model combines the results of finite element structural and computational fluid dynamics models and predicts the microphone response with a minimum number of fitting parameters. The structural analysis is used to obtain the diaphragm parameters, and the computational fluid analysis is used for modeling the effect of air inside the backvolume of the microphone. The model is verified by experiments and its validity in the presence of higher order modes is discussed. One of the most important advantages of this model is the prediction of individual mode movements of the diaphragm. This information is used for optimizing these microphones in intensity measurements. It is shown that the effect of the second mode can be suppressed by modifying the diaphragm design. This results in more accurate intensity measurements in a larger frequency band.

Chapter 5 describes an alternative method, electrostatic force feedback, to alter the optical microphone response without changing its mechanical design. The force feedback method is used to add electronic damping to the system. This increases the bandwidth and the dynamic range of the microphone. These are achieved without adding significant noise to the system. In addition to the modification of stiffness and damping, force feedback is used to alter the response of the individual modes of the diaphragm. A two-sided force feedback method is developed for this purpose. In this method, the force feedback signal is applied to both electrostatic ports located on each side of the diaphragm. The model predictions show that it is possible to suppress the effect of the undesired mode movement, resulting in improved directionality response and pressure residual intensity index by optimized two-sided force feedback signal. This ability

enables one to change the response of these optical gradient microphones to pressure or to a pressure gradient in a large bandwidth. Future work in this area can focus on the use of force feedback to correct for fabrication variations and to relax mechanical design parameters so that simpler to fabricate diaphragms can provide the desired response, improving the overall yield of the fabrication process.

## Research Contributions

This research has resulted in several significant contributions. The first important outcome is the high performance optical directional microphones with low noise and small size. In these microphones, highly sensitive directional sensing of the novel biomimetic diaphragms is combined with the highly sensitive optical displacement detection, making these microphones a good candidate for hearing aids. In addition to the hearing aids, pressure gradient output of these optical microphones can be used to measure particle velocity which is the main component for sound intensity probes. By combining these gradient microphones with a pressure sensor, sound intensity measurements can be performed in small spaces without the need for multiple spacers at frequencies between 50 Hz – 10 kHz.

The second important contribution is the innovative use of the electrostatic actuation ports for force feedback application while using the optical detection as the sensing mechanism. Force feedback can be used to change the dynamics of the microphone by shaping its frequency response in a desired manner, increasing the dynamic range and improving the directionality without adding significant noise. The other important use of force feedback is to tune the optical gradient microphones to

respond to pressure or to a pressure gradient selectively. Using this electrostatic feedback method, it is possible to have an intensity probe with a single sensor measuring the pressure and the particle velocity at the same point in a field with the application of force feedback. This solves some of the problems that are caused by using two different sensors at two different locations to measure the sound intensity.

The third contribution is the equivalent circuit model developed for predicting the response of the optical directional microphones. This model includes both the structural and air effects, and can be used to predict the response of the optical microphones with applied electrostatic and force feedback signals.

The results of this research can be used in a broad range of opto-mechanical sensors such as optical accelerometers or seismometers, where the undesirable vibration mode suppression is desired. Although it is demonstrated only by two-sided force feedback method here, this method can be generalized and can provide flexibility in designing the optical sensors with individually controlled modes.

# APPENDIX A

# FLOTRAN MODEL VERIFICATION

To verify the Finite Element Modeling (FEM) results of the FLOTRAN model, initially a simple Helmholtz resonator is used because the theoretical solution of this resonator is well known. A Helmholtz resonator mainly consists of two parts; a rigid walled cavity of volume V filled with fluid (usually air) and a neck with length L that connects the cavity to the open medium. The basic schematic of the Helmholtz resonator can be seen from Figure 86.

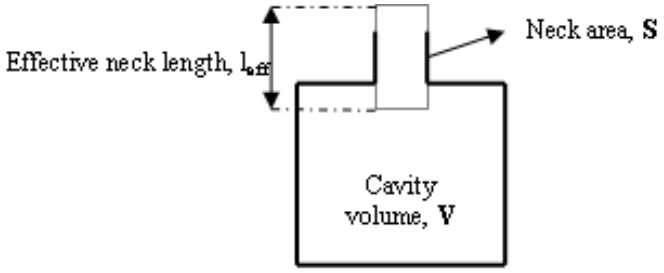


Figure 86: Basic schematic of a Helmholtz resonator.

When the air in the neck is forced to move by a small amount into the cavity, the compression of the air in the cavity causes the cavity pressure to increase. This increase in the pressure causes the air in the neck to move back to the open medium. As a result of this, the air in the neck of the resonator oscillates because of the spring effect of the air inside the container. This kind of resonator is mainly used for picking out the particular frequencies from a sound field. This particular frequency is designed to be the resonant

frequency of the resonator which depends on its volume, neck dimensions and the properties of the fluid filled inside.

### 3D Helmholtz Resonator

The 3D FEM model of the fluid inside the resonator is shown in Figure 87. The fluid is modeled by using the FLUID 142 3D-FLOTRAN element. In FLOTRAN, only the fluid domain is modeled and the analysis is done by taking losses into consideration. The dimensions of the Helmholtz resonator are given in Table 7. After having the model of the resonator, it is time to apply the necessary boundary conditions for the analysis. All the walls of the cavity and the side walls of the neck are modeled as a rigid wall and given zero displacement and velocity input. The opening at the neck is modeled as a pressure release hole and given zero relative pressure as a boundary condition. The air inside the neck is forced to move initially by an impulsive velocity input and then the transient FLOTRAN analysis is done. The time period for the transient analysis is chosen such that all the response of the air dies out.

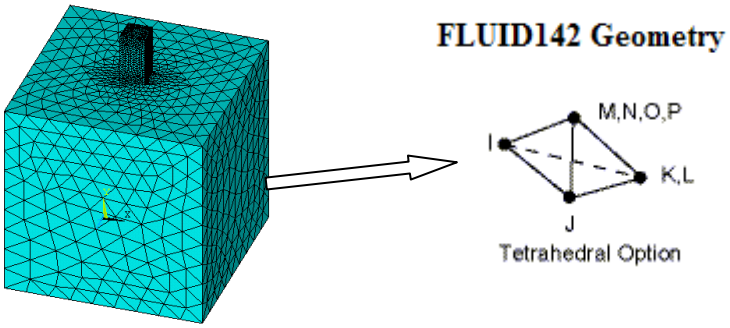


Figure 87: 3D model of the fluid inside the Helmholtz Resonator (left), FLUID142 element (right)

When the FLOTRAN analysis is done, the pressure and velocity results of the model are exported in order to post-process with MATLAB. Figure 88 shows the exported result for velocity input at the neck and pressure response in the cavity as a function of time.

Table 7: Dimensions of the Helmholtz resonator model

| | |
|---|---|
| Cavity volume, V | 4000μm x 4000μm x 4000μm |
| Cross-sectional area of the neck, S | 500μm x 500μm |
| Length of the neck, L | 1000μm |

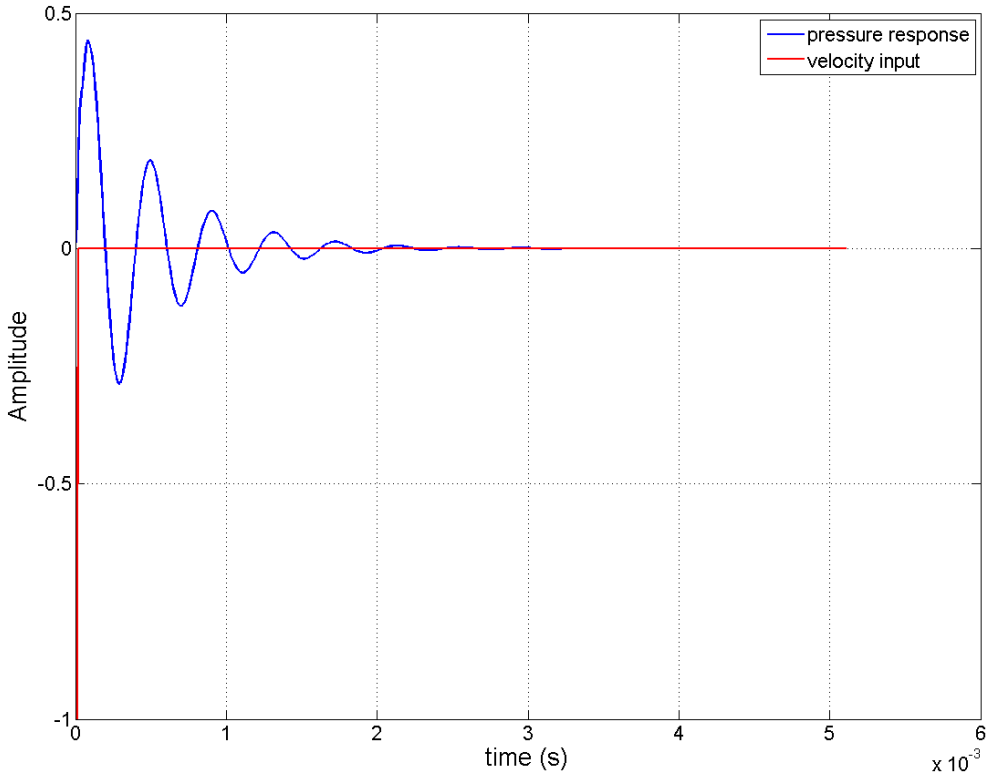


Figure 88: Amplitude of the gauge pressure and velocity input vs. time (3D modeling)

A custom written MATLAB program gets these time domain signals and converts into the frequency domain signals by using Fast Fourier Transform (FFT). Since the velocity and pressure signals as a function of frequency are known, frequency response and impedance can be simply calculated. Figure 89 shows the magnitude and phase of the frequency response of the fluid inside the Helmholtz resonator. As can be seen from Figure 89, there is one resonance frequency of this 3D Helmholtz resonator, which is expected. This resonance frequency is found to be 2530 Hz from the FLOTRAN model. Another important thing to mention in this figure is that the roll-off of the response after the resonance is 12 dB/octave [89].

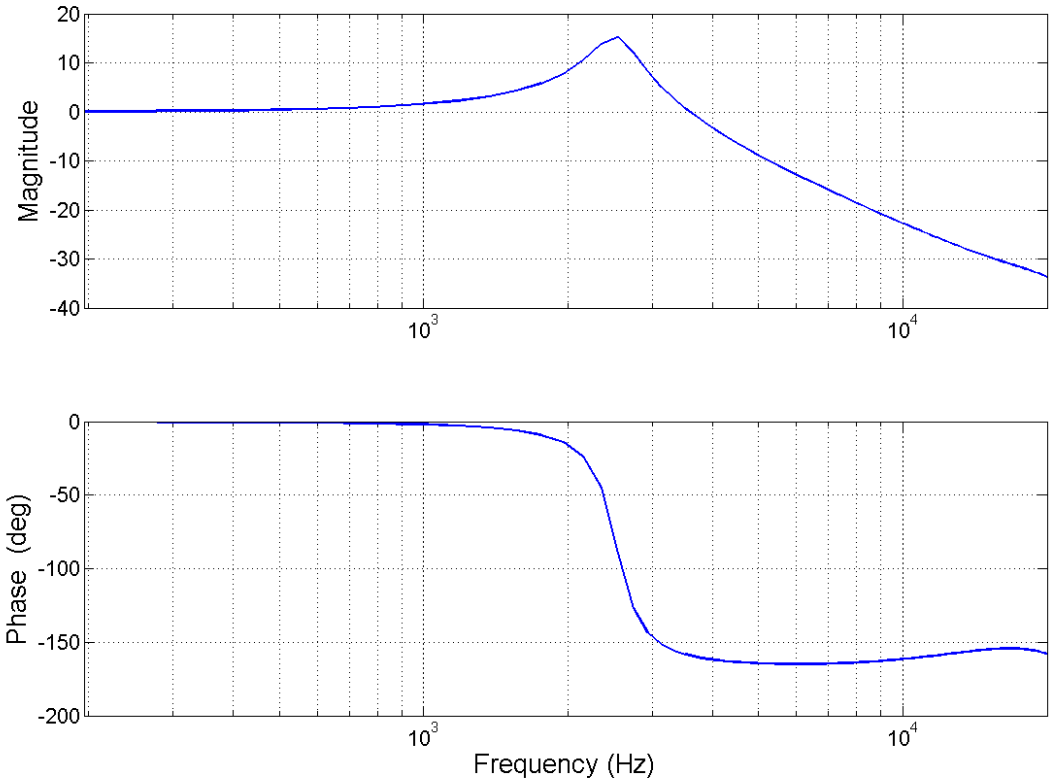


Figure 89: Magnitude and phase of the frequency response of 3D Helmholtz resonator model

**Theoretical Modeling**

To create an equivalent circuit model for the Helmholtz resonator, lumped element representation is used. With this method, the dynamic behavior of the resonator can be found by modeling the air inside the neck as a mass element, the radiation of the open neck to the medium and the loss at the neck as resistance elements and finally the air inside the cavity as a stiffness element. Connection rules between elements are defined based on whether an effort-type variable or a flow-type variable is shared between them. Whenever an effort variable, such as force, voltage or pressure, is shared between two or more elements, those elements are connected in parallel in the equivalent circuit. With the same analogy, whenever common flow, like velocity, current, or volume velocity is shared between elements, those elements are connected in series. By using these rules, the equivalent circuit representation of the Helmholtz resonator is obtained and shown in Figure 90.

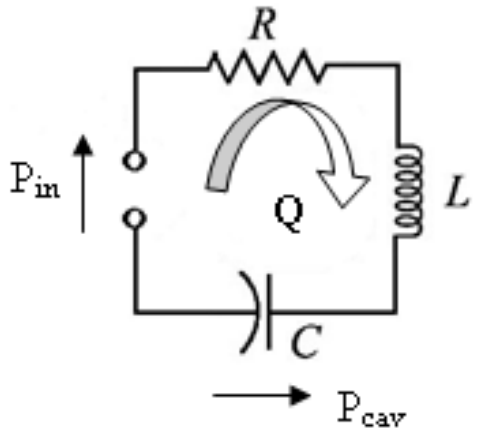


Figure 90: Equivalent circuit representation of the Helmholtz resonator with the lumped elements

The frequency response function, which represents the pressure amplification, ***A*** of the resonator is calculated as;

$$A = \frac{\frac{1}{j\omega C}}{R + j\omega L + \frac{1}{jwC}} = \frac{Z_C}{Z_R + Z_L + Z_C} \tag{37}$$

where, $C$ is the acoustic compliance (analogous to electrical capacitance), $L$ is the acoustic inertance (analogous to electrical inductance), $R$ is the acoustic resistance (analogous to electrical resistance), $Z_x$ is the acoustic impedance of $x$.

From an analysis of the equivalent circuit, the resonance frequency of the Helmholtz resonator is calculated as;

$$f_{res} = \frac{c}{2\pi}\sqrt{\frac{S}{Vl_{eff}}} \tag{38}$$

By using this theoretical equation for the resonance frequency, a comparison can be done between the FLOTRAN model and the theoretical value. Table 8 shows the found and predicted resonance frequency of the Helmholtz resonator. These values show good agreement, which verifies that the FLOTRAN 3D model can be used for fluid analysis to predict the results accurately.

Table 8: Comparison of resonance frequencies; 3D model vs. theoretical

| | |
|---|---|
| $f_{res}$ from FLOTRAN 3D model | ~ 2530 Hz |
| $f_{res}$ from theoretical model | 2543 Hz |

**2D Helmholtz resonator**

Since 3D analysis needs too much computation time, 2D approximation of the Helmholtz resonator is also modeled. In this 2D model, the same dimensions, boundary conditions and input velocity impulse are used with FLUID 141 2D-FLOTRAN element.

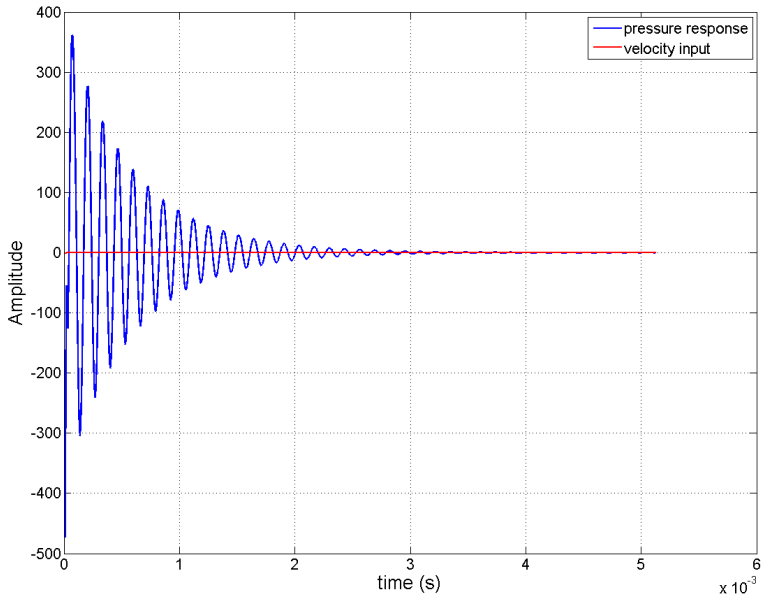


Figure 91: Amplitude of the gauge pressure and velocity input vs. time (2D modeling)

The velocity input and the pressure response of the fluid are shown in Figure 91 as a function of time. After taking the FFT of these signals and post-processing in MATLAB, it is found that the resonance frequency of this resonator is around 7840 Hz, which can be seen from Figure 92.

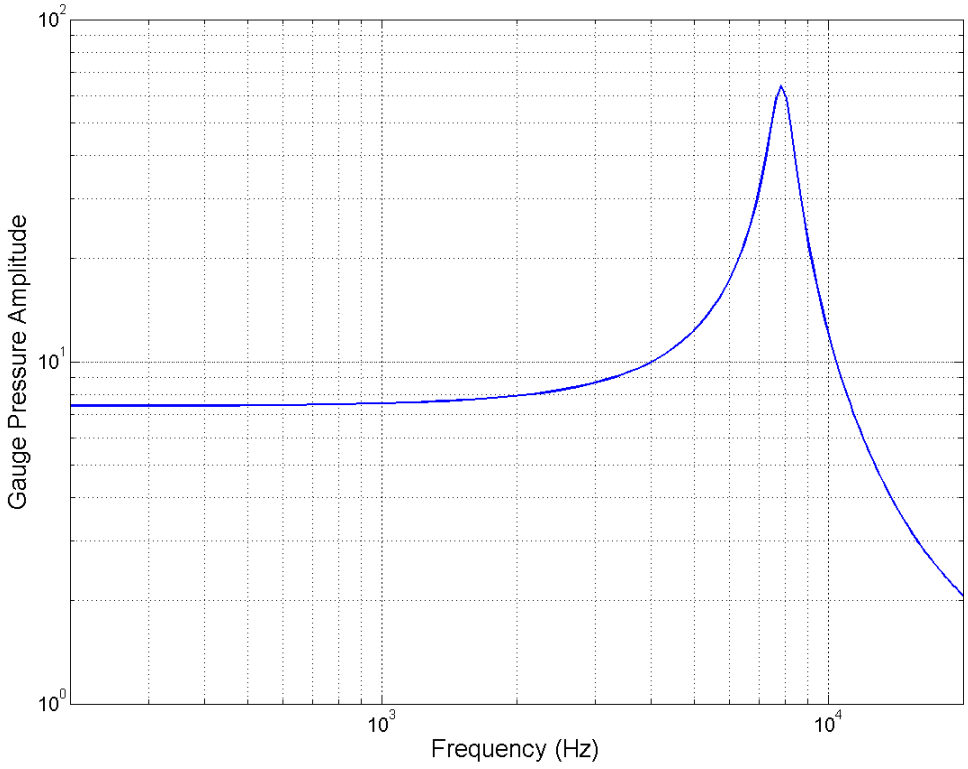


Figure 92: Pressure profile with 2D Helmholtz model in frequency domain

Since the 2D model does not have a depth dimension, the theoretical solution of the resonance frequency for 2D model is modified as;

$$f_{res} = \frac{c}{2\pi}\sqrt{\frac{S}{Vl_{eff}}} \quad \text{where} \quad S = wt \quad \text{and} \quad V = xyt$$

$$f_{res} = \frac{c}{2\pi}\sqrt{\frac{w}{xyl_{eff}}} \tag{39}$$

where, $w$ is the width of the neck, $t$ is the depth of the neck and cavity (since it is 2D, FLOTRAN assumes same depth for the neck and the volume), $x$ and $y$ are the length and width of the cavity respectively. By using the modified equation above, the theoretical resonance frequency of the resonator is found to be 7630 Hz.

Table 9: Comparison of resonance frequencies; 2D model vs. theoretical

| | |
|---|---|
| $f_{res}$ from FLOTRAN 2D model | ~ 7840 Hz |
| $f_{res}$ from theoretical model | 7630 Hz |

These modeling results of the Helmholtz resonator show that 2D model also prediction with acceptable results. With this verification, the 2D FLOTRAN fluid model of the directional microphone can be used to predict the effect of the air on the microphone response.

# APPENDIX B

# OPTICAL MODELING MATLAB CODE

```
close all;
clear all;

% Define physical and mathematical constants
eps_0 = 8.85e-12;          % Permittivity of free space
c_0 = 299792458;           % Speed of light in vacuum (m/s)
e = 2.718281828;           % Natural logarithmic base

% Define VCSEL parameters
lambda = 850e-9;           % VCSEL operating wavelength (m)
P0 = 2e-3;                 % VCSEL nominal output power (W)
theta_div = 8;             % VCSEL FWHM divergence angle (degrees)
w0 = lambda / (pi * (theta_div/1.18) * pi / 180);        % Beam waist size
k = (2 * pi) / lambda;     % wavevector magnitude

% Define structure parameters
z1 = 400e-6;               % z1 is the distance from the VCSEL to the lens front plane
z2 = 450e-6;               % z2 is the distance from the lens back plane to the grating plane
L1 = 450e-6;               % L1 is the distance from the grating plane to the lens back plane
L2 = 450e-6;               % L2 is the distance from the lens front plane to the photodiode plane

% Define grating and windowing parameters
fill = 50;                 % define the grating fill factor (i.e., duty cycle)
g_p = 4e-6;                % define the grating period
g_x = 600e-6;              % g_x is the grating's x-dimension
g_y = 600e-6;              % g_y is the grating's y-dimension
g_x_pos = 0;               % g_x_pos is the x-coordinate of the center of the finite grating in real space
g_y_pos = 0;               % g_y_pos is the y-coordinate of the center of the finite grating in real space
R = 0;                     % R is the amplitude reflection coefficient of the region outside the grating window

% Define tilt angle
tilt_angle = 0 * pi / 180;    % tilt_angle is the tilt angle (radians) of the backplate specified as a rotation of
                              the xy-plane in the +z-direction

% Import transmissive functions from ZEMAX
import = importdata('FTRANS.TXT');
f_trans = import.data;
import = importdata('BTRANS.TXT');
b_trans = import.data;
trans_array_size = 512;

Nx = 3000;          % number of pixels defined in x-dimension
Ny = 3000;          % number of pixels defined in y-dimension
dim = [Nx, Ny];     % vector specifying overall pixel dimensions

% Create spatial domain and range for VCSEL plane
Tx_u1 = 1e-3;
dx_u1 = Tx_u1 / Nx;
```

```
vx_u1 = -Tx_u1 / 2:dx_u1:(Tx_u1/2 - dx_u1);
Ty_u1 = 1e-3;
dy_u1 = Ty_u1 / Ny;
vy_u1 = -Ty_u1 / 2:dy_u1:(Ty_u1/2 - dy_u1);
[x_u1, y_u1] = meshgrid(vx_u1, vy_u1);

% Create spatial frequency domain and range
fx_v_u1 = (-1/Tx_u1 * Nx/2):(1/Tx_u1):(1/Tx_u1 * Nx/2 - 1/Tx_u1);
fy_v_u1 = (-1/Ty_u1 * Ny/2):(1/Ty_u1):(1/Ty_u1 * Ny/2 - 1/Ty_u1);

 % Create new (scaled) spatial domain and range for lens front/back planes
vx_u2 = fx_v_u1 .* lambda .* z1;
vy_u2 = fy_v_u1 .* lambda .* z1;
[x_u2, y_u2] = meshgrid(vx_u2, vy_u2);

% Create new (scaled) spatial frequency domain and range
dx_u2 = vx_u2(2) - vx_u2(1);
Tx_u2 = Nx * dx_u2;     % Value into ZEMAX
fx_v_u2 = (-1/Tx_u2 * Nx/2):(1/Tx_u2):(1/Tx_u2 * Nx/2 - 1/Tx_u2);
dy_u2 = vy_u2(2) - vy_u2(1);
Ty_u2 = Ny * dy_u2;
fy_v_u2 = (-1/Ty_u2 * Ny/2):(1/Ty_u2):(1/Ty_u2 * Ny/2 - 1/Ty_u2);

 % Create new (scaled) spatial domain and range for grating plane
vx_u4 = fx_v_u2 .* lambda .* z2;
vy_u4 = fy_v_u2 .* lambda .* z2;
[x_u4,y_u4] = meshgrid(vx_u4, vy_u4);

% Create new (scaled) spatial frequency domain and range
dx_u4 = vx_u4(2) - vx_u4(1);
Tx_u4 = Nx * dx_u4;
fx_v_u4 = (-1/Tx_u4 * Nx/2):(1/Tx_u4):(1/Tx_u4 * Nx/2 - 1/Tx_u4);
dy_u4 = vy_u4(2) - vy_u4(1);
Ty_u4 = Ny * dy_u4;
fy_v_u4 = (-1/Ty_u4 * Ny/2):(1/Ty_u4):(1/Ty_u4 * Ny/2 - 1/Ty_u4);

 % Create new (scaled) spatial domain and range for lens back/front planes
vx_u5 = fx_v_u4 .* lambda .* L1;
vy_u5 = fy_v_u4 .* lambda .* L1;
[x_u5,y_u5] = meshgrid(vx_u5, vy_u5);

% Create new (scaled) spatial frequency domain and range
dx_u5 = vx_u5(2) - vx_u5(1);
Tx_u5 = Nx * dx_u5;
fx_v_u5 = (-1/Tx_u5 * Nx/2):(1/Tx_u5):(1/Tx_u5 * Nx/2 - 1/Tx_u5);
dy_u5 = vy_u5(2) - vy_u5(1);
Ty_u5 = Ny * dy_u5;
fy_v_u5 = (-1/Ty_u5 * Ny/2):(1/Ty_u5):(1/Ty_u5 * Ny/2 - 1/Ty_u5);

 % Create new (scaled) spatial domain and range for photodiode plane
vx_u7 = fx_v_u5 .* lambda .* L2;
vy_u7 = fy_v_u5 .* lambda .* L2;
[x_u7,y_u7] = meshgrid(vx_u7, vy_u7);
```

```
% Create new (scaled) spatial frequency domain and range
dx_u7 = vx_u7(2) - vx_u7(1);
Tx_u7 = Nx * dx_u7;
fx_v_u7 = (-1/Tx_u7 * Nx/2):(1/Tx_u7):(1/Tx_u7 * Nx/2 - 1/Tx_u7);
dy_u7 = vy_u7(2) - vy_u7(1);
Ty_u7 = Ny * dy_u7;
fy_v_u7 = (-1/Ty_u7 * Ny/2):(1/Ty_u7):(1/Ty_u7 * Ny/2 - 1/Ty_u7);

% Scale transmissive functions from ZEMAX
[x_old,y_old] = meshgrid(linspace(-dx_u2*Nx/2,dx_u2*Nx/2,trans_array_size));
[x_new,y_new] = meshgrid(linspace(-dx_u2*Nx/2,dx_u2*Nx/2,Nx));
f_trans = interp2(x_old,y_old,f_trans,x_new,y_new);
[x_old,y_old] = meshgrid(linspace(-dx_u2*Nx/2,dx_u2*Nx/2,trans_array_size));
[x_new,y_new] = meshgrid(linspace(-dx_u2*Nx/2,dx_u2*Nx/2,Nx));
b_trans = interp2(x_old,y_old,b_trans,x_new,y_new);

% Define field (Gaussian profile) to be propagated at VCSEL plane
% u1 = sqrt((2 * P0) / (pi * w0^2)) * exp(-(x.^2 + y.^2) / w0^2);
% Use normalization constant to make total power distributed across
% field equal to P0
u1_gaussian = exp(-(x_u1.^2 + y_u1.^2) / w0.^2);
nu_0 = 377;             % Characteristic Impedance of Free Space (Ohms)
A = sqrt((P0 / ((sum(sum(abs(u1_gaussian).^2 * dx_u1 * dy_u1)))) * 2 * nu_0));      % Normalization
Constant
u1 = A * u1_gaussian;

% Plot field at VCSEL plane
figure(1);
imagesc(vx_u1 * 1e3, vy_u1 * 1e3, abs(u1));
xlabel('x (mm)');
ylabel ('y (mm)');
title('Electric field at VCSEL plane (Field magnitude)');

% Propagate field to lens front plane
% Propagate field with quadratic-phase exponential
p1 = u1 .* exp((1i * k) / (2 * z1) * (x_u1.^2 + y_u1.^2));
% Fourier-transform propagated field to find Fresnel approximation
ft_p1 = dx_u1 * dy_u1 * fftshift(fft2(p1));
% Calculate field arriving at lens front plane
u2 = ft_p1 .* exp(1i * k * z1) / (1i * lambda * z1) .* exp((1i * k) / (2 * z1) * (x_u2.^2 + y_u2.^2)) .* exp(1i
* k * z1);

% Plot field arriving at lens front plane
figure(2);
imagesc(vx_u2 * 1e3, vy_u2 * 1e3, abs(u2));
xlabel('x (mm)');
ylabel ('y (mm)');
title('Electric field at lens front plane (Field magnitude)');

clear u1_gaussian;
clear u1;
clear p1;
clear ft_p1;
clear x_u1;
clear y_u1;
```

```
% Calculate field arriving at lens back plane via multiplication with
% forward magnitude- and phase-transmissive function from ZEMAX
u3 = u2 .* exp(-1i .* f_trans);

% Plot field arriving at lens back plane
figure(3);
imagesc(vx_u2 * 1e3, vy_u2 * 1e3, abs(u3));
xlabel('x (mm)');
ylabel('y (mm)');
title('Electric field at lens back plane (Field magnitude)');

% Propagate field to grating plane
% Propagate field with quadratic-phase exponential
p3 = u3 .* exp((1i * k) / (2 * z2) * (x_u2.^2 + y_u2.^2));
% Fourier-transform propagated field to find Fresnel approximation
ft_p3 = dx_u2 * dy_u2 * fft2(p3);
% Calculate field arriving at grating plane
u4 = ft_p3 .* exp(1i * k * z2) / (1i * lambda * z2) .* exp((1i * k) / (2 * z2) * (x_u4.^2 + y_u4.^2)) .* exp(1i
* k * z2);

% Plot field arriving at grating plane
figure(4);
imagesc(vx_u4 * 1e3, vy_u4 * 1e3, abs(u4));
xlabel('x (mm)');
ylabel ('y (mm)');
title('Electric field at grating plane (Field magnitude)');

clear u2;
clear u2_prime;
clear lens_space;
clear p2;
clear ft_p2;
clear x_u2;
clear y_u2;
clear p3;
clear ft_p3;
clear u3;

% Windowing function to account for finite grating
window_space = zeros(dim(1));
test_win_x = (abs(x_u4 - g_x_pos) <= g_x/2);
test_win_y = (abs(y_u4 - g_y_pos) <= g_y/2);

for index1 = 1:dim(1)
   for index2 = 1:dim(2)
      if ((test_win_x(index1,index2) == 1) && (test_win_y(index1,index2) == 1))
         window_space(index1,index2) = 1;
      end
   end
end

u4_win = zeros(dim(1)); % initialize windowed field matrix
u4_win_inverse = zeros(dim(1));
```

```
for index1 = 1:dim(1)
   for index2 = 1:dim(2)
      if window_space(index1,index2) == 1
         u4_win(index1,index2) = u4(index1,index2);
      end
      u4_win_inverse(index1,index2) = u4(index1,index2) - u4_win(index1,index2);
   end
end

u4_win_outside = R .* u4_win_inverse;

clear test_win_x;
clear test_win_y;
clear window_space;
clear u4_win_inverse;
clear u4;

% Plot windowed optical field
figure(5);
imagesc(vx_u4 * 1e3, vy_u4 * 1e3, abs(u4_win));
xlabel('x (mm)');
ylabel('y (mm)');
title('Windowed electric field at grating plane (Field magnitude)');

% Plot inverse optical field
figure(6);
imagesc(vx_u4 * 1e3, vy_u4 * 1e3, abs(u4_win_outside));
xlabel('x (mm)');
ylabel('y (mm)');
title('Inverse of windowed electric field at grating plane (Field magnitude)');

g_v = .5 * (1 + square(2 * pi / g_p * (vx_u4 - g_p / 4), fill));
[gx_new, gy_new] = meshgrid(vx_u4, g_v);
gy_new = gy_new';

% Set grating finger reflectivity
for index7 = 1:dim(1)
   if g_v(index7) == 0
      u4_win(:,index7) = sqrt(1) .* u4_win(:,index7);
   end
end

% Plot windowed optical field with applied finger reflectivity
figure(7);
imagesc(vx_u4 * 1e3, vy_u4 * 1e3, abs(u4_win));
xlabel('x (mm)');
ylabel('y (mm)');
title('Windowed electric field at grating plane with applied finger reflectivity (Field magnitude)');

p4_reflected = u4_win_outside .* exp(1i * k / (2 * L1) * (x_u4.^2 + y_u4.^2));
ft_p4_reflected = dx_u4 * dy_u4 * (fft2(p4_reflected));
u5_intermediate_window_outside = ft_p4_reflected .* exp(1i * k .* L1) ./ (1i * lambda .* L1) .* exp(1i * k
./ (2 .* L1) .* (x_u5.^2 + y_u5.^2)) .* exp(1i * k * L1);
```

```
clear gx_new;
clear u4_win_outside;
clear p4_reflected;
clear ft_p4_reflected;

gap_dist = (vy_u4 + vy_u4(Ny)) .* tan(0 * pi / 180);

d0_test = [0 lambda/8 lambda/4];
size_d0 = size(d0_test);
order0_pos = zeros(2,1);
order1_pos = zeros(2,1);

for gap_test = 1:size_d0(2)

    gap_test;

    d = d0_test(gap_test) + gap_dist;
    phi_array = (4 * pi .* d) ./ lambda;
    [dummy, phase_exp] = meshgrid(vx_u4, phi_array);
    g_final = exp(1i .* phase_exp .* gy_new);

    u4_bar = u4_win .* g_final;
    p4 = u4_bar .* exp(1i * k / (2 * L1) * (x_u4.^2 + y_u4.^2));
    ft_p4 = dx_u4 * dy_u4 * (fft2(p4));

    u5_intermediate_grating_window = ft_p4 .* exp(1i * k .* L1) ./ (1i * lambda .* L1) .* exp(1i * k ./ (2 .*
L1) .* (x_u5.^2 + y_u5.^2)) .* exp(1i * k * L1);
    u5 = u5_intermediate_window_outside + u5_intermediate_grating_window;

    clear d;
    clear phi_array;
    clear dummy;
    clear phase_exp;
    clear g_final;
    clear u4_bar;
    clear p4;
    clear ft_p4;
    clear u5_intermediate_grating_window;

    figure(gap_test + 20);
    imagesc(vx_u5 * 1e3, vy_u5 * 1e3, abs(u5));
    title('Optical field arriving at lens back plane from diffraction from grating');
    xlabel('x (mm)');
    ylabel('y (mm)');

    % Calculate field arriving at lens front plane via multiplication with
    % forward magnitude- and phase-transmissive function from ZEMAX
    u6 = u5 .* exp(-1i .* b_trans);

    % Propage field to photodiode plane
    % Propagate field with quadratic-phase exponential
    p6 = u6 .* exp((1i * k) / (2 * L2) * (x_u5.^2 + y_u5.^2));
    % Fourier-transform propagated field to find Fresnel approximation
    ft_p6 = dx_u5 * dy_u5 * fft2(p6);
```

```
    % Calculate field arriving at photodiode plane
    u7 = ft_p6 .* exp(1i * k * L2) / (1i * lambda * L2) .* exp((1i * k) / (2 * L2) * (x_u7.^2 + y_u7.^2)) .*
exp(1i * k * L2);

    abs_optical_field = abs(u7);

    clear u7;
    clear p6;
    clear ft_p6;
    clear u6;
    clear u5;

    figure(gap_test + 40);
    imagesc(vx_u7 * 1e3, vy_u7 * 1e3, abs_optical_field);
    title('Optical field arriving at photodiode plane');
    xlabel('x (mm)');
    ylabel('y (mm)');

    if gap_test == 1
        [order0_pos(1),order0_pos(2)] = find(abs(u7) == max(max(abs(u7))));
        cross_section = abs(u7(order0_pos(1),:));
        figure(100);
        plot(vx_u7*1e3, cross_section);
        order_size = length(find((cross_section > (1/e * max(max(abs(u7))))) == 1)) * dx_u7
    elseif gap_test == 3
        [order1_pos(1),order1_pos(2)] = find(abs(u7) == max(max(abs(u7))));
    end

end

saveas(2,'Field at Lens Front Plane','png');
saveas(20,'Lens','png');
saveas(21,'Field at Lens Plane from Diffraction, 0','png');
saveas(22,'Field at Lens Plane from Diffraction, pi2','png');
saveas(23,'Field at Lens Plane from Diffraction, pi','png');
saveas(3,'Field at Lens Back Plane','png');
saveas(4,'Field at Grating Plane','png');
saveas(41,'Field at Photodiode Plane, 0','png');
saveas(42,'Field at Photodiode Plane, pi2','png');
saveas(43,'Field at Photodiode Plane, pi','png');
close all;

order_ypos = order0_pos(1);
order_ypos_u7 = vy_u7(order_ypos);
order_xpos_0 = order0_pos(2);
order_xpos_0_u7 = vx_u7(order_xpos_0);
order_xpos_1 = order1_pos(2);
order_xpos_1_u7 = vx_u7(order_xpos_1);

dA = dx_u7 * dy_u7;
radius = order_size;
cx = order_xpos_1_u7;
cy = order_ypos_u7;
pd_space = zeros(dim);
```

```
pd_space((x_u7 - cx).^2 + (y_u7 - cy).^2 <= radius.^2) = 400;
cx = -order_xpos_1_u7;
cy = order_ypos_u7;
pd_space((x_u7 - cx).^2 + (y_u7 - cy).^2 <= radius.^2) = 401;
cx = order_xpos_0_u7;
cy = order_ypos_u7;
pd_space((x_u7 - cx).^2 + (y_u7 - cy).^2 <= radius.^2) = 402;

figure(70);
imagesc(vx_u7*1e3,vy_u7*1e3,pd_space);
xlabel('x (mm)');
ylabel('y (mm)');
title('Photodiode positions and areas on photodiode plane');
saveas(70,'Photodiodes','png');

d0_test = linspace(0,lambda,65);
size_d0 = size(d0_test);
d0_normalized = d0_test ./ lambda;

gap_dist = (vy_u4 + vy_u4(Ny)) .* tan(tilt_angle);

for gap_index = 1:size_d0(2)

   gap_index

   d = d0_test(gap_index) + gap_dist;
   phi_array = (4 * pi .* d) ./ lambda;
   [dummy, phase_exp] = meshgrid(vx_u4, phi_array);
   g_final = exp(1i .* phase_exp .* gy_new);

   u4_bar = u4_win .* g_final;
   p4 = u4_bar .* exp(1i * k / (2 * L1) * (x_u4.^2 + y_u4.^2));
   ft_p4 = dx_u4 * dy_u4 * (fft2(p4));

   u5_intermediate_grating_window = ft_p4 .* exp(1i * k .* L1) ./ (1i * lambda .* L1) .* exp(1i * k ./ (2 .*
L1) .* (x_u5.^2 + y_u5.^2)) .* exp(1i * k * L1);
   u5 = u5_intermediate_window_outside + u5_intermediate_grating_window;

   clear d;
   clear phi_array;
   clear dummy;
   clear phase_exp;
   clear g_final;
   clear u3_bar;
   clear p3;
   clear ft_p3;
   clear u4_intermediate_grating_window;

   figure(8);
   imagesc(vx_u5 * 1e3, vy_u5 * 1e3, abs(u5));
   title('Optical field arriving at lens back plane from diffraction from grating');
   xlabel('x (mm)');
   ylabel('y (mm)');
```

```
    % Calculate field arriving at lens front plane via multiplication with
    % forward magnitude- and phase-transmissive function from ZEMAX
    u6 = u5 .* exp(-1i .* b_trans);

    % Propagate field to photodiode plane
    % Propagate field with quadratic-phase exponential
    p6 = u6 .* exp((1i * k) / (2 * L2) * (x_u5.^2 + y_u5.^2));
    % Fourier-transform propagated field to find Fresnel approximation
    ft_p6 = dx_u5 * dy_u5 * fft2(p6);
    % Calculate field arriving at photodiode plane
    u7 = ft_p6 .* exp(1i * k * L2) / (1i * lambda * L2) .* exp((1i * k) / (2 * L2) * (x_u7.^2 + y_u7.^2)) .*
exp(1i * k * L2);

    abs_optical_field = abs(u7);

    clear u4;
    clear p4;
    clear ft_p4;
    clear u5;

    figure(9);
    imagesc(vx_u7 * 1e3, vy_u7 * 1e3, abs_optical_field);
    title('Optical field arriving at photodiode plane');
    xlabel('x (mm)');
    ylabel('y (mm)');

    filename = strcat(num2str(gap_index),' Field');
    saveas(9,filename,'png');

    power_0 = 0;
    power_neg_1 = 0;
    power_pos_1 = 0;

    for index3 = 1:dim(1)
       for index4 = 1:dim(2)
          switch pd_space(index3, index4)
             case 400
                power_neg_1 = power_neg_1 + eps_0 * c_0 / 2 * abs_optical_field(index3,index4).^2 * dA;
             case 401
                power_pos_1 = power_pos_1 + eps_0 * c_0 / 2 * abs_optical_field(index3,index4).^2 * dA;
             case 402
                power_0 = power_0 + eps_0 * c_0  / 2 * abs_optical_field(index3,index4).^2 * dA;
          end
       end
    end

    efficiency_0 = power_0 / P0 * 100;
    efficiency_neg_1 = power_neg_1 / P0 * 100;
    efficiency_pos_1 = power_pos_1 / P0 * 100;
    efficiency_total = (power_neg_1 + power_pos_1 + power_0) / P0 * 100;

    scan_power_neg_1(gap_index) = power_neg_1;
    scan_power_pos_1(gap_index) = power_pos_1;
    scan_power_0(gap_index) = power_0;
```

```
    scan_efficiency_neg_1(gap_index) = efficiency_neg_1;
    scan_efficiency_pos_1(gap_index) = efficiency_pos_1;
    scan_efficiency_0(gap_index) = efficiency_0;
    scan_efficiency_total(gap_index) = efficiency_total;

end

 results = zeros(65,3);
results(:,1) = d0_normalized;
results(:,2) = scan_efficiency_0;
results(:,3) = scan_efficiency_pos_1;

filename = 'Curves.txt';
save(filename, 'results', '-ASCII');

close all;
clear all;
```

# REFERENCES


[1] P. R. Scheeper, A. G. H. Van Der Donk, W. Olthuis, and P. Bergveld, "A review of silicon microphones," *Sensors and actuators. A, Physical,* vol. 44, pp. 1-11, 1994.

[2] M. Gayford, *Microphone engineering handbook*: Focal Press, 1994.

[3] A. G. H. v. d. Donk, P. R. Scheeper, W. Olthuis, and P. Bergveld, , "Modeling of silicon condensor microphones," *Sensors and Actuators A,* vol. 40, pp. 203-16, 1994.

[4] A. Torkkeli, O. Rusanen, J. Saarilahti, H. Seppä, H. Sipola, and J. Hietanen, "Capacitive microphone with low-stress polysilicon membrane and high-stress polysilicon backplate," *Sensors and Actuators A: Physical,* vol. 85, pp. 116-123, 2000.

[5] J. Bergqvist and F. Rudolf, "A silicon condenser microphone using bond and etch-back technology," *Sensors and Actuators A: Physical,* vol. 45, pp. 115-124, 1994.

[6] Q. Zou and R. Lin, "Silicon capacitive microphones with corrugated diaphragms," *The Journal of the Acoustical Society of America,* vol. 105, p. 998, 1999.

[7] M. Bao and H. Yang, "Squeeze film air damping in MEMS," *Sensors and Actuators A: Physical,* vol. 136, pp. 3-27, 2007.

[8] Larson Davis, "http://www.larsondavis.com/AirCondenserMicrophones.htm", 03/01/2010.

[9] S. Bouwstra, T. Storgaard-Larsen, P. Scheeper, J. Gulløv, J. Bay, M. Müllenborn, and P. Rombach, "Silicon microphones-a Danish perspective," *J. Micromechanics and Microengineering,* vol. 8, pp. 64-68, 1998.

[10] P. V. Loeppert and S. B. Lee, "SiSonicTM—The First Commercialized MEMS microphone," in *Solid-State Sensors, Actuators and Microsystems Workshop, Hilton Head Island, South Carolina*, 2006, pp. 27-30.

[11] S. Kochkin, "MarkeTrak III Identifies Key Factors In Determining Consumer Satisfaction," *Hearing Journal,* vol. 45, pp. 39-39, 1992.

[12] F. K. Kuk, "Subjective Preference For Microphone Types in Daily Listening Environments," *Hearing Journal,* vol. 49, pp. 29-38, 1996.

[13] H. B. Nielsen, "A Comparison Between Hearing Aids with Directional Microphone and Hearing Aids with Conventional Microphone," *International Journal of Audiology,* vol. 2, pp. 173-176, 1973.

[14] M. T. Cord, R. K. Surr, B. E. Walden, and L. Olson, "Performance of directional microphone hearing aids in everyday life," *J Am Acad Audio.,* vol. 13, pp. 295-307, 2002.

[15] S. C. Thompson, "Tutorial on microphone technologies for directional hearing aids," *The Hearing Journal,* vol. 56, p. 14, 2003.

[16] R. N. Miles, D. Robert, and R. R. Hoy, "Mechanically coupled ears for directional hearing in the parasitoid fly Ormia ochracea," *Journal of the Acoustical Society of America,* vol. 98, p. 3059, 1995.

[17] R. N. Miles, W. Cui, Q. Su, R. Wu, L. Tan, Y. Liu, S. A. Jones, V. Mohnankrishnaswami, T. Strait, and W. Butler, "Development of novel biologically inspired directional microphones," *The Journal of the Acoustical Society of America,* vol. 120, p. 3158, 2006.

[18] R. N. Miles, Q. Su, W. Cui, M. Shetye, F. L. Degertekin, B. Bicen, C. Garcia, S. Jones, and N. Hall, "A low-noise differential microphone inspired by the ears of the parasitoid fly Ormia ochracea," *Journal of the Acoustical Society of America,* vol. 125, p. 2013, 2009.

[19] D. A. Keating, "The optical microphone-fact or fiction," *Proc IOA,* vol. 11, pp. 277-287, 1989.

[20] K. Kadirvel, R. Taylor, S. Horowitz, L. Hunt, M. Sheplak, E. Florida Univ Gainesville Dept Of, and E. Computer, *Design and characterization of MEMS optical microphone for aeroacoustic measurement*: University of Florida Dept. of Electrical & Computer Engineering, 2004.

[21] H. Sagberg, A. Sudbo, O. Solgaard, K. A. H. Bakke, and I. R. Johansen, "Optical microphone based on a modulated diffractive lens," *IEEE Photonics Technology Letters,* vol. 15, pp. 1431-1433, 2003.

[22] N. Bilaniuk, "Optical Microphone Transduction Techniques," *Applied Acoustics,* vol. 50, pp. 35-63, 1997.

[23] B. M. Jost and J. P. Stec, "Refractive fiber optic microphones with ambient acoustic noise-canceling capabilities," *The Journal of the Acoustical Society of America,* vol. 98, p. 1612, 1995.

[24] T. Weardon, "Integrated optics for interferometric sensors," *Transducer Technology,* vol. 10, June 1990.

[25] G. G. Yaralioglu, "Analysis and design of an interdigital cantilever as a displacement sensor," *Journal of Applied Physics,* vol. 83, p. 7405, 1998.

[26] E. B. Cooper, "High-resolution micromachined interferometric accelerometer," *Applied Physics Letters,* vol. 76, p. 3316, 2000.

[27] S. R. Manalis, S. C. Minne, A. Atalar, and C. F. Quate, "High-speed atomic force microscopy using an integrated actuator and optical lever detection," *Review of Scientific Instruments,* vol. 67, p. 3294, 1996.

[28] N. A. Hall, M. Okandan, R. Littrell, B. Bicen, and F. L. Degertekin, "Micromachined optical microphone structures with low thermal-mechanical noise levels," *The Journal of the Acoustical Society of America,* vol. 122, p. 2031, 2007.

[29] W. Lee, N. A. Hall, Z. Zhou, and F. L. Degertekin, "Fabrication and characterization of a micromachined acoustic sensor with integrated optical readout," *IEEE Journal of Selected Topics in Quantum Electronics,* vol. 10, pp. 643-651, 2004.

[30] F. Fahy, *Sound intensity*: Taylor & Francis Group, 1995.

[31] H. F. Olson, "Apparatus for Converting Sound Vibrations into Electrical Variations," in *US Patent 1,885,001*, 1932.

[32] C. W. Clapp and F. A. Firestone, "The Acoustic Wattmeter, an Instrument for Measuring Sound Energy Flow," *The Journal of the Acoustical Society of America,* vol. 13, p. 124, 1941.

[33] R. H. Bolt and A. A. Petrauskas, "An Acoustic Impedance Meter for Rapid Field Measurements," *The Journal of the Acoustical Society of America,* vol. 15, p. 79, 1943.

[34] T. J. Schultz, "Acoustic Wattmeter," *The Journal of the Acoustical Society of America,* vol. 28, p. 693, 1956.

[35] B. Kjaer, "Primer: Sound Intensity, http://www.bksv.com/doc/br0476.pdf", 03/01/2010.

[36] F. Jacobsen and H. E. de Bree, "A comparison of two different sound intensity measurement principles," *The Journal of the Acoustical Society of America,* vol. 118, p. 1510, 2005.

[37] Larson Davis Sound Intensity Probe, "Model 2260 Sound Intensity Probe, http://www.pazul.com/websites/ldx2/2260.html", 03/01/2010.

[38] G.R.A.S., "Special Intensity Probe, http://www.gras.dk/00012/00056/00147", 03/01/2010.

[39] F. Jacobsen and H. E. de Bree, "Measurement of sound intensity: pu probes versus pp probes," *International Conference on Noise and Vibration Engineering,* November 2005.

[40] H. E. Bree, P. Leussink, T. Korthorst, H. Jansen, T. Lammerink, and M. Elwenspoek, "The Micro-Flown, A Novel Device Measuring Acoustical Flows," 1995.

[41] R. Raangs, "Exploring the use of the microflown," 2005.

[42] H. E. De Bree, "The Microflown: An acoustic particle velocity sensor," *Acoustics Australia,* vol. 31, pp. 91-94, 2003.

[43] H. E. de Bree, R. Raangs, and E. Druyvesteyn, "Sound intensity measurements with the Microflown sensor," *Internoise 2004,* vol. Czech Republic, 2004.

[44] F. L. Degertekin, N. A. Hall, and B. Bicen, "Micromachined microphones with diffraction-based optical interferometric readout," *The Journal of the Acoustical Society of America,* vol. 120, p. 3272, 2006.

[45] N. A. Hall, W. Lee, and F. L. Degertekin, "Broadband self-calibrating micromachined microphones with integrated optical displacement detection," *The Journal of the Acoustical Society of America,* vol. 112, p. 2234, 2002.

[46] N. A. Hall, B. Bicen, M. K. Jeelani, W. Lee, S. Qureshi, F. L. Degertekin, and M. Okandan, "Micromachined microphones with diffraction-based optical displacement detection," *Journal of the Acoustical Society of America,* vol. 118, p. 3000, 2005.

[47] C. T. Garcia, N. A. Hall, F. L. Degertekin, B. Bicen, K. Jeelani, and M. S. Qureshi, "An integrated optical microphone test-bed for acoustic measurements," *Journal of the Acoustical Society of America,* vol. 121, p. 3155, 2007.

[48] N. A. Hall, M. Okandan, R. Littrell, B. Bicen, and F. L. Degertekin, "Simulation of Thin-Film Damping and Thermal Mechanical Noise Spectra for Advanced Micromachined Microphone Structures," *Microelectromechanical Systems, Journal of,* vol. 17, pp. 688-697, 2008.

[49] P. C. D. Hobbs, "Ultrasensitive laser measurements without tears," *Appl. Opt,* vol. 36, pp. 903-920, 1997.

[50] H. Torun, J. Sutanto, K. K. Sarangapani, P. Joseph, F. L. Degertekin, and C. Zhu, "Micromachined membrane-based active probe for biomolecular mechanics measurement," *Nanotechnology,* vol. 18, p. 165303, 2007.

[51] N. Yamauchi, Y. Inaba, and M. Okamura, "An integrated photodetector-amplifier using a-Si pin photodiodesand poly-Si thin-film transistors," *IEEE Photonics Technology Letters,* vol. 5, pp. 319-321, 1993.

[52] B. Bicen, S. Jolly, K. Jeelani, C. Garcia, N. A. Hall, F. L. Degertekin, Q. Su, W. Cui, and R. N. Miles, "Integrated optical displacement detection and electrostatic actuation for directional optical microphones with micromachined biomimetic diaphragms," *IEEE Sensors Journal,* vol. vol. 9, pp. pp. 1933-1941, 2009.

[53] W. Cui, B. Bicen, N. Hall, S. A. Jones, F. L. Degertekin, and R. N. Miles, "Optical Sensing in a Directional Mems Microphone Inspired by the Ears of the Parasitoid Fly, Ormia Ochracea," *Micro Electro Mechanical Systems, 2006. MEMS 2006 Istanbul. 19th IEEE International Conference on,* pp. 614-617, 2006.

[54] Lasermate, " http://www.lasermate.com/VCC85A1G-IS.html", 03/01/2010.

[55] R. N. Miles and F. L. Degertekin, "Optical sensing in a directional MEMS microphone," in *US Patent App. 11/335,137*, 2006.

[56] B. Bicen, C. Garcia, N. A. Hall, M. Okandan, W. Cui, Q. T. Su, R. N. Miles, and L. Degertekin, "Diffraction based optical MEMS microphones and accelerometers with active electrostatic force feedback," *Journal of the Acoustical Society of America,* vol. 123, p. 3230, 2008.

[57] N. A. Hall, M. Okandan, R. Littrell, D. K. Serkland, G. A. Keeler, K. Peterson, B. Bicen, C. T. Garcia, and F. L. Degertekin, "Micromachined Accelerometers With Optical Interferometric Read-Out and Integrated Electrostatic Actuation," *J. of Microelectromechanical Sys.,* vol. 17, p. 37, 2008.

[58] N. A. Hall, W. Lee, and F. L. Degertekin, "Capacitive micromachined ultrasonic transducers with diffraction-based integrated optical displacement detection," *Ultrasonics, Ferroelectrics and Frequency Control, IEEE Transactions on,* vol. 50, pp. 1570-1580, 2003.

[59] J. W. Goodman, *Introduction to Fourier optics*, 3rd edition ed. vol. Chapter 4: Roberts & Co, 2005.

[60] S. W. Rienstra and A. Hirschberg, "An introduction to acoustics," *Eindhoven University of Technology,* 2002.

[61] Anonymous, "Standard test method for impedance and absorption of acoustical materials using a tube, two microphones, and a digital frequency analysis system," *ASTM Standard E 1050-90* 1990.

[62] IEC.1043, "Instruments for the measurement of sound intensity," *International Standard* 1993.

[63] F. J. Fahy, "International Standards for the Determination of Sound Power Levels of Sources Using Sound Intensity Measurement: an Exposition," *Applied Acoustics,* vol. 50, pp. 97-110, 1997.

[64] "Acoustics -- Determination of sound power levels of noise sources -- Precision methods for anechoic and semi-anechoic rooms," *International Organization for Standardization, ISO 3745,* 2003.

[65] Larson Davis, "http://www.larsondavis.com/docs/REF600_500Datasheet.pdf", 03/01/2010.

[66] NYB, "An Introduction to Fan Acoustics," in *Engineering Letter - 12*.

[67] H. F. Olson, *Dynamical analogies*: Van Nostrand New York, 1958.

[68] F. V. Hunt, *Electroacoustics: the analysis of transduction, and its historical background*: Acoustical Society of America, 1982.

[69] T. B. Gabrielson, U. Center, and P. A. Warminster, "Mechanical-thermal noise in micromachined acoustic and vibration sensors," *Electron Devices, IEEE Transactions on,* vol. 40, pp. 903-909, 1993.

[70] J. Bergqvist, "Finite-element modeling and characterization of a silicon condenser microphone with a highly perforated backplate," *Sensors and actuators. A, Physical,* vol. 39, pp. 191-200, 1993.

[71] P. Zhou, J. Gilmore, Z. Badics, and Z. J. Cendes, "Finite element analysis of induction motors based on computing detailed equivalent circuit parameters," *IEEE Transactions on Magnetics,* vol. 34, pp. 3499-3502, 1998.

[72] G. G. Yaralioglu, M. H. Badi, A. S. Ergun, and B. T. Khuri-Yakub, "Improved equivalent circuit and finite element method modeling of capacitive micromachined ultrasonic transducers," in *IEEE Ultrasonics Symposium*, 2003, pp. 469-472.

[73] S. C. Thompson, J. L. LoPresti, E. M. Ring, H. G. Nepomuceno, J. J. Beard, W. J. Ballad, and E. V. Carlson, "Noise in miniature microphones," *Journal of the Acoustical Society of America,* vol. 111, p. 861, 2002.

[74] S. D. Senturia, *Microsystem design*: Kluwer Academic Publishers Norwell, MA, 2001.

[75] P. R. Stepanishen, "The radiation impedance of a rectangular piston," *Journal of Sound Vibration,* vol. 55, pp. 275-288, 1977.

[76] A. Berry, J. L. Guyader, and J. Nicolas, "A general formulation for the sound radiation from rectangular, baffled plates with arbitrary boundary conditions," *The Journal of the Acoustical Society of America,* vol. 88, p. 2792, 1990.

[77] ANSYS, "Computational Fluid Dynamics Guide," in *Release 11.0 Documentation for ANSYS 11.0*, 2009.

[78] L. Tan, "Diaphragm Design And Analysis For The Ormia Differential Microphone," in *Mechanical Engineering*. vol. Master of Science Binghamton: State University of New York, 2002.

[79] C. Kittel, "Elementary Statistical Mechanics," Wiley, 1958.

[80] R. C. Ritter and G. T. Gillies, "Classical limit of mechanical thermal noise reduction by feedback," *Physical Review A,* vol. 31, pp. 995-1000, 1985.

[81] M. Pinard, P. F. Cohadon, T. Briant, and A. Heidmann, "Full mechanical characterization of a cold damped mirror," *Physical Review A,* vol. 63, p. 13808, 2000.

[82] T. R. Rodríguez and R. García, "Theory of Q control in atomic force microscopy," *Applied Physics Letters,* vol. 82, p. 4821, 2003.

[83] J. Tamayo, A. D. L. Humphris, R. J. Owen, and M. J. Miles, "High-Q Dynamic Force Microscopy in Liquid and Its Application to Living Cells," *Biophysical Journal,* vol. 81, pp. 526-537, 2001.

[84] J. Mertz, O. Marti, and J. Mlynek, "Regulation of a microcantilever response by force feedback," *Applied Physics Letters,* vol. 62, p. 2344, 1993.

[85] N. E. Wu, R. N. Miles, and O. A. Aydin, "A digital feedback damping scheme for a micromachined directional microphone," *American Control Conference. Proceedings of the 2004,* 2004.

[86] F. L. Degertekin, N. A. Hall, and W. Lee, "Highly-sensitive displacement-measuring optical device," in *Georgia Technology Research Corporation 10/704, 932*, 2006.

[87] S. Hadjiloucas, L. S. Karatzas, D. A. Keating, and M. J. Usher, "An optical force-feedback microphone measuring audible emissions from plants," in *Conference on Lasers and Electro-Optics* 1994, pp. 266-267.

[88] L. S. Karatzas, D. A. Keating, and M. J. Usher, "A practical optical force-feedback microphone," *Transactions of the Institute of Measurement & Control,* vol. 16, p. 75, 1994.

[89] D. T. Blackstock, *Fundamentals of physical acoustics*: John Wiley & Sons, Inc., 2000.

# VITA

Baris Bicen received his B.S. degree from Middle East Technical University, Ankara, Turkey, in 2004 and his M.S. degree from Georgia Institute of Technology, Atlanta, in 2006, both in mechanical engineering. He received his Ph.D. degree in mechanical engineering at Georgia Institute of Technology in 2010. His research interests include actively controlled optical and opto-acoustic micromachined sensors, and their application to acoustic transducers, mostly microphones and intensity probes. He is a member of the Institute of Noise Control Engineering of the USA (INCE-USA) and Acoustical Society of America (ASA).